UNIVERSITÀ DEGLI STUDI DI PAVIA

PH.D. IN ELECTRONICS, COMPUTER SCIENCE AND ELECTRICAL ENGINEERING

XXXII CYCLE

A. Y. 2016-2019

ON THE DEVELOPMENT OF AN INNOVATIVE MM-WAVE IMAGING SYSTEM FOR BREAST CANCER DETECTION

Doctoral Thesis of Simona Di Meo

Tutor: Prof. Marco Pasian

INDEX

INTRODUCTION

The use of electromagnetics in a medical context has very deep origins. The first researches about the use of electromagnetic techniques in biomedical field dates back to **1926**, when the electrical impedance measurements in the frequency range [20-100] kHz were proposed to monitor the development of the pulmonary oedema in dogs and cats (Lambert and Gremels (1926)).

Successively, in the **1936**, the use of an electromagnetic flowmeter for the measurement of the blood flux was proposed (Kolin (1936)). After about fifty years from the first application, in **1971**, the electromagnetic impedance technique was proposed for the cardiac monitoring both in the operative and post-operative phase (Williams *et al.* (1971)). Some years later, in **1973**, the idea of diagnosing and monitoring the pulmonary oedema with the electromagnetics was proposed in a modified version, by means of radiative techniques at microwave frequencies instead of measuring the electrical impedance of the lung, overcoming the problem of the effect of short circuit due to the presence of a highly conductive medium surrounding the lung (Susskind (1973)).

All these techniques rely on the very strong dependence of tissues dielectric properties on their water content, and for this reason they were originally conceived for the detection of the alteration in tissues dielectric properties, index of a variation in water content, usually related to some pathological condition.

The first glimmers about the possible use of microwave radiometry in medical field dates back to **1974**, when it was demonstrated that biological bodies emit detectable microwave radiation (Bigu del Blanco and Romero-Sierra (1974)). Previously, radiometric techniques were limited to radio-astronomic, communications, and atmospheric sensing. Starting from the job of (Bigu del Blanco and Romero-Sierra (1974)), several studies were conducted in order to derive the best trade-off between the maximum achievable penetration depth and the resolution (Enander *et al.* (1974), Barrett *et al.* (1977), Barrett and Myers (1975)), and also the capability of the microwave radiometry in detecting breast cancers was demonstrated in (Porter and Miller (1978)); however, these experiments on phantoms showed low values for sensitivity and specificity.

From **1975** to **1979**, different medical applications of microwaves were proposed, from the microwave detection of breathing to the measurements of the heart dynamic (Lin (1975), Jacobi *et al.* (1979), Yamaura (1978)). In addition, in **1978**, the electromagnetic imaging as possible diagnostic instrument was applied for the thorax monitoring (Lyte and Dines (1978), Tasto and Schomberg (1978)). In the same year, the Doppler radar technique in X-band for the monitoring of the movement of the arterial wall was also proposed (Lyte and Dines (1978), Henderson and Webster (1978), Stuchly *et al.* (1978), Tasto and Schomberg (1978)).

The main goal of the medical radiology is to see what is present inside a body in a safe and non-invasive way. *Microwaves* generally represent that part of the electromagnetic spectrum with a frequency from 300 MHz to 300 GHz (Sorrentino e Bianchi (2010)), and generally the frequency range from 30 GHz to 300 GHz is additionally marked as *millimetre-wave* regime.

The microwave imaging was proposed basing on the limitations both of X-rays and Ultrasounds for certain applications already recognized at the time, as the monitoring of pulmonary oedema (Lyte and Dines (1978), Tasto and Schomberg (1978)). In this case, indeed, X-rays lose their sensitivity for that kind of tissue; while, on the other hand, Ultrasounds cannot propagate in lungs soft tissues. These are the reasons why, in **1978**, the microwave imaging as a possible solution to these problems has been proposed; therefore, opening several

needs, as the exact knowledge of the dielectric properties of the biological tissues as well as the need to design proper antennas to couple the energy within the imaged organs.

In **1986**, Larsen and Jacobi published a work demonstrating the potentiality of the microwave imaging for the monitoring of perfused canine kidney (Larsen and Jacobi (1986)). In this work, the intensity modulation of a raster scanned display was used in order to convert the measured scattering parameters in an image; however, with very long acquisition time.

Since these first preliminary studies, several data acquisition setups have been proposed for increasingly sophisticated applications, both in linear and circular configurations (Pichot *et al.* (1985), Broquetas *et al.* (1991)), as the bone, heart, breast and brain imaging, as well as the respiration and the heartbeat detection (Semenov and Corfield (2008), Lin and Clarke (1982), Nikolova (2011), Colton and Monk (1995), Meaney *et al.* (2012), Semenov *et al.* (1996), Semenov (2000), Semenov *et at.* (2003), Semenov *et at.* (2006), Brovoll *et al.* (2013)).

In **1995**, Colton and Monk (Colton and Monk (1995)) proposed the feasibility study of electromagnetic imaging for the detection and the monitoring of the leukemia treatment, by means of numerical experiments at 800 MHz based on the nonlinear fixed frequency approach. The presence of leukemia in bone marrow, indeed, causing an increasing in the cellular population in the bone marrow, alters the dielectric properties of the marrow, in particular, increasing its electrical permittivity and decreasing its conductivity; therefore, making possible the detection of these variations.

From **1996** to **2006**, Semenov *et al.* (Semenov *et al.* (1996), Semenov (2000), Semenov *et at.* (2003), Semenov *et at.* (2006)), have demonstrated that the dielectric properties of myocardium in the microwave regime can be used as an indicator of its blood content, infarction and ischemia. Basing on these dielectric differences, they demonstrated the possibility of using microwave tomography to detect the myocardial infarction by distinguishing the dielectric properties of the normal tissues from the infarcted ones.

In **2008**, Semenov *et al* (Semenov *et al.* (2008)) proposed also the microwave tomography for brain imaging with the main aim of the stroke detection. The used frequency range was from 0.5 GHz to 2.5 GHz. Also in this case, the basic idea is that the stroke compromises cerebral blood flow; therefore, it is possible to use microwave imaging, since it is able to image tissues basing on differences in their dielectric properties.

In **2012**, Meaney *et al* (Meaney *et al* (2012)), investigated the bone imaging by acquiring 2-D and 3-D microwave tomographic images, from 500 MHz and 3 GHz, of the hell bones of two patients to evaluate the correlation between the microwave properties and the measurements of X-ray density, showing a good correlation between both permittivity and conductivity and the measurements of density derived by the computed tomography.

In **2013**, Brovoll *et al* (Brovoll *et al* (2013)) proposed a radar approach for UWB imaging of dynamic reflectors (like human heartbeats) within the body. The proposed system was an array with eight body-contact dipole antennas working in the frequency range from 0.1 to 3 GHz, and a good resolution for the observation of different moving parts of the heart was achieved. The time-lapse movie of the beating heart was successively created with a frame rate of 25 Hz.

One of the most investigated applications of microwave frequencies in biomedical context is the breast cancer detection (Nikolova (2011)), and the research in this field is so advanced that different research groups tested their prototypes on alive patients in a clinical phase (Klemm *et al.* (2009), Grzegorczyk *et al.* (2012)). Breast cancer is the most diagnosed cancer among women worldwide, the second most common cancer overall and it is the fifth most common cause of death from cancer in women. The incidence rate of this disease is

increasing, moving from nearly 1.7 million new cases diagnosed in 2012 to over 2 million new cases in 2018 (web site, American Institute for Cancer Research). However, despite this increase in the incidence rate, the overall survival rates for breast cancer are also increasing. This is mainly due to the increasing access to medical care in many nations and the large-scale diffusion of screening campaigns for breast. Detecting the cancer in an early and localized stage increases the survival chance for the woman, and as an example, in many countries, the five-year survival rate for women diagnosed with small breast cancers (Stage I/II) is from 80 to 90% (web site, American Institute for Cancer Research).

Nowadays, the set of imaging techniques for breast cancer detection is very large. The most commonly used approaches are the X-ray mammography, the Ultrasound, the breast Magnetic Resonance Imaging (breast-MRI) and the Positron Emitting Tomography (PET); however, the main limitations of these modalities justify the need of new complementary or supplementary techniques for breast cancer detection. X-ray mammography, thanks to its very high resolution, is currently the gold standard imaging method and it is nowadays adopted for screening purposes; however, it involves the woman exposition to ionizing radiations and it cannot be used in breasts with high content of fibro-glandular tissue. Ultrasound, if on one hand it is safe for the woman, on the other hand is too operator dependent (therefore, the success of the diagnosis depends on the capability of the radiologist) and it cannot be used for the scanning of breasts with too high percentage of adipose tissue. The breast Magnetic Resonance Imaging shows high values of *Sensibility* in dense breasts (technical term for assessing the quality of a diagnostic system, as it will be explained in the following of this thesis); however, since it requires a bulky and very expensive machine, not all clinical structures have this kind of instrumentation. The Positron Emitting Tomography to detect a tumor within the breast makes use of a tracing material that is metabolized differently by malignant cells compared to the normal adjacent tissues, and the brightness of the photons emitted by the tissues is detected by a proper scanner; however, it is a still developing technique for breast imaging. For all these reasons, new imaging techniques for breast are welcome. In particular, photoacoustic and microwave imaging have been mainly investigated.

In photoacoustic imaging, biological tissues are radiated by light impulses coming from one or more than one laser. These impulses are successively converted in heath by the chromophores within the tissues, basing on their degree of absorption, and the following temperature rise causes a local rapid expansion, called thermos-elastic effect, therefore generating low intensity acoustic waves. Then, ultrasonic transducers are used to detect and process them in order to obtain photoacoustic images (Beard (2011)). In this case, the achievable resolutions depend strongly by the ultrasound detector and by the characteristic in frequency of the produced acoustic waves. Some prototype of this kind has been proposed also for breast cancer detection in systems named *Photo-Acoustic Mammography* (PAM) and currently tested in clinical environments (Heijblom *et al.* (2012)).

On the other hand, there is the microwave imaging, that is the subject of this thesis. Microwave medical imaging systems represent a low cost, low risk, and easy to use alternative with respect to the aforementioned current medical imaging systems and the technological progresses done in the microelectronic, material sciences and integrated systems field made available compact and relatively low cost instrumentation; therefore, encouraging more and more this growing interest for microwave and millimetre wave systems.

Microwave medical imaging systems rely on the detection of the dielectric contrast between healthy and malignant tissues, particularly marked in the breast, where it was demonstrated by several experimental campaigns that the volume percentage of adipose tissue can be very high (as detailed in Chapter I). On top of this fundamental motivation, other reasons like the anatomical position and the dimension of the human breast have increased the appeal of the microwave breast imaging. The low values for tissue losses, the relatively small dimensions of the woman breast, as well as its protruding position, indeed, make possible its almost

whole scanning with proper hardware, the possibility of getting information from different angles of view, and eventually the opportunity of compressing a bit its soft tissues to improve the achieved results. In addition, thanks to the high dielectric contrast between the tumor and the surrounding healthy tissues, the backscattering from the malignant lesion is stronger than the one derived from all other internal structures; therefore, making possible its detection.

Microwave imaging could be done by means of passive or active systems. The passive systems detect the microwave radiation that is naturally emitted by human body (or parts of it) as a function of its temperature; they are based on the radiometry principle and do not require the illumination of the scenario with electromagnetic radiation (Barrett *et al.* (1977), Haslam *et al.* (1984), Land (1987), Schaller (1989), Carr (1989)). Usually, they are narrowband systems and make use of typical wavelengths of 10-30 cm. However, since they show several vulnerabilities (e.g., blood concentrations and/or some kinds of healthy tissue could provide a local increase in temperature), they are not currently investigated for the breast imaging anymore.

On the other hand, in the active systems, the microwave radiation is generated and coupled within the tissues. The signals backscattered from the tissue heterogeneities and/or from dielectric lesions are collected by one or more than one antenna and processed. The hardware setups stand out mainly for the patient positioning, the kind of acquired signals, the acquisition surfaces and the use or not of the coupling medium. In addition, another fundamental difference between microwave imaging systems is the kind of signals that is acquired, that could be transmitted, reflected or both. Generally, this aspect brings to the division of the microwave imaging techniques in two macro-categories: tomographic and radar approach.

Usually, in both these approaches, transmission and reflection measurements of the signals is done by means of a Vector Network Analyzer (VNA), to which the antennas are connected through a proper switch matrix; the use of coupling medium was proposed not only in all tomographic systems but also in several radar architectures in order to maximize the energy entering in the tissue and to reduce the unwanted signal of multi-path reflected by the background; in addition, almost always, the signals collected with both approaches require calibration before the use of the data in the image reconstruction algorithms. However, these two approaches, despite these common points, are substantially different.

The goal of the **microwave tomography**, alternatively known as *quantitative imaging* method, is to reconstruct a "map" of dielectric properties (permittivity and conductivity) of the volume of interest. Usually, in these approaches, the imaged object is surrounded by different transmitting and receiving antennas and the data acquisition is done slice-by-slice; each antenna illuminates in turn the scenario, while all others collect the transmitted and/or reflected signal (antennas close to the transmitting one usually collect the reflected signal). Then, the transmitting antenna is switched and the procedure is repeated till all the illumination angles are scanned. The acquisition plane is the one of the array. To allow the complete scanning of the breast, the array is moved in vertical direction (therefore, perpendicularly to the acquisition plane) from the nipple to the chest wall. The data is acquired and processed separately slice-by-slice; therefore, at the end of the scanning, there is a stack of 2-D images representing an almost 3-D image of the object. The 2-D image of the slice is reconstructed by considering only the data acquired by scanning the single slice. In order to maximize the coupling of the signal within the biological tissue, reducing also the reflection from the interface air-body, usually a coupling medium is used, and both the antenna and the imaged object are submerged in a homogeneous coupling medium. Commonly, for microwave tomography, single frequencies in the frequency range from 0.3 to 5 GHz are used. However, even if from a theoretic point of view, these techniques would give the complete information of the imaged object, from a practical point of view, they are based on the solution of inverse scattering problems, usually ill-posed and not univocal, as well as computationally very expensive.

On the other hand, the goal of the **radar imaging**, alternatively known as *qualitative imaging* method, is to see if a dielectric anomaly is present within the illuminated structure, and eventually determine what is its relative position, without deriving its dielectric properties (that, on the contrary, are assumed as *a-priori* information). The backscattering methods use the reflected signals to deduce the position of a possible main scatterer within the illuminated geometry, making use of the same principle of the *Ground Penetrating Radar* (Persico (2014)). This approach has the strong advantage of proposing a direct mathematical solution, without the need of solving an inverse scattering problem. The produced images are achieved by processing simultaneously all the available data. From these radar techniques it is not possible to derive a complete information about the analyzed volume; however, for application like the breast cancer detection, the identification of the presence and the relative position of the target with respect to any other kind of tissue could be enough. In this case, in order to have a good spatial resolution, an Ultra-WideBand (UWB) signal is necessary. In particular, in the radar imaging each antenna transmits a pulse in the time domain (that in the frequency domain is UWB) and the signals that are backscattered by the target are received by one or more than one antenna, sometimes the transmitting antenna could be used also as a receiving one. Radar imaging uses reflected (or backscattered) signals that could be transmitted and collected by a single antenna (mono-static approach) or multiple antennas (multi-static approach). The need of using the multi-static approach or to move the single transmitting and receiving antenna in multiple positions is determined by the high values for attenuations in biological tissues, laying the need of increasing the overall signal-to-noise ratio.

In this Thesis, the interest is for active microwave radar systems.

Several algorithms have been proposed for the focusing of a tumor in radar approaches, and the most common are: the confocal microwave imaging (Fear *et al.* (2002), Li and Hagness (2001), Lim *et al.* (2008)), the Microwave Imaging via Space-Time Beamforming (MIST) (Li *et al.* (2004), Bond *et al.* (2003)), and the Tissue Sensing Adaptive Radar (TSAR) (Fear *et al.* (2013), Sill and Fear (2005)). In all cases, a good spatial resolution is achieved by means of an UWB signal.

The *confocal radar imaging* makes use of the radar synthetic focusing principle, the same that is typically used for example in the remote sensing and in the detection of mine within the ground (Fear *et al.* (2002), Li and Hagness (2001), Lim *et al.* (2008)). The setup could be based on mono-static or multi-static architecture; however, in both cases, the fundamental thing is the collection of as much scattered signals as possible from different angles of view. These measurements are usually done in the time domain. The basic idea is that if a stronger scatter (a dielectric anomaly, usually corresponding to a tumor) is present in the illuminated scenario, than all the waveforms contain this information together with the noise and the clutter. In particular, the backscattered signal is composed by the incident waveform, the scatter from the tumor, the scattered signal from the skin and the other backscattered signals from other internal tissues within the body (representing the clutter). Before using these data for the image reconstruction algorithms, in the confocal radar imaging, the unwanted contribution of the skin is removed from each received waveform, so that only the contribution of the tumor and the clutter is extracted. After the pre-processing of the signals, the waveform backscattered and processed by each antenna in the array is integrated over time in order to include the waveforms due to all the transmitting antennas. Then, the image is created by temporally shifting all these pre-processed waveforms and by summing all these integrated waveforms for each synthetic focal point within the illuminated object. For this last step, it is assumed known both the propagation speed of the wave and the signal attenuation within the tissue (therefore, the correction factor for the radial spreading of the wave that is higher and higher as the wave goes far from the transmitting antenna). The temporary shift and the weight of each backscattered waveform are specific for each voxel and depend by the distance of the voxel from the corresponding sensor. If a voxel belongs to a scatterer all the scattered signals are coherently summed, otherwise, they are

incoherently summed and they reduce each other. The coherent sum, if present, brings to a strong energy of the signal in correspondence of that point.

In the *Microwave Imaging via Space-Time Beamforming* (*MIST*) algorithm (Li *et al.* (2004), Bond *et al.* (2003)), each antenna in the array transmits a low power UWB signal into the breast and collects the backscattered signals. Then, the beamformer on one hand spatially focuses the backscattered signals, reducing the contribution of clutter and noise, and on the other hand compensates for frequency-dependent propagation effects. This focusing is achieved in this way. The received signals are temporally shifted in order to align the signals backscattered from a target hypothesized in a candidate location. Then, in each antenna channel, these time-aligned signals are passed through a bank of Finite Impulse Response (FIR) filters, and are summed in order to produce the output of the beamformer. The weights of the FIR filters are determined so that the components of the signals backscattered from the candidate location have unit gain, compensating for frequency-dependent effect. After this, the output of the beamformer is time gated to the time interval containing the signal backscattered from the candidate location, and at the end the energy is calculated. If a scattering object exists in that location, the energy is very high. By changing the time shifts, the time gating, and the weights of the FIR filters, the beamformer is scanned in different locations, and the image of the backscattered signal strength is given by the display of the energy as a function of the location.

The *Tissue Sensing Adaptive Radar* (*TSAR*) algorithm, (Fear *et al.* (2013), Sill and Fear (2005)), detects all the reflections within the region of interest and uses this information in the imaging procedures. In the TSAR algorithm, the signal collected by the antennas is firstly calibrated, in order to remove the response of the antennas. After this step, the focal point is synthetically scanned through the investigated region, and basing on this an image is created. In particular, the image achieved in this way shows the exact position of the skin, and this information is used to gate the imaging region. After the identification of the skin position, its contribution is estimated at each antenna and it is subtracted from the total signal. Finally, by means of a focusing approach including a weighting factor based on the relative distance of the focal point from the antennas, the image of the tumor is created.

Two fundamental requirements that a good imaging system has to satisfy are: a wide dynamic range for the receivers and a good resolution in the produced images (Nikolova (2011)). Biological tissues represent a very high loss propagative media; therefore, it is fundamental in the design of the system to take in consideration the *dynamic range of the system*, usually corresponding to the one of the receiver. The *dynamic range* of a microwave imaging system is, indeed, defined as the ratio between the stronger undistorted signal and the weaker detectable signal (Nikolova (2011)). Due to the high losses of human breast tissues, *dynamic range*s in the order of -100 dB with respect to the injected signal are required, and the actual availability of dedicated transceiver, as well as high performance VNA with *dynamic range* up to -140 dB, has encouraged the interest for the microwave breast imaging.

Another fundamental point that has to be taken into account in the system design is the achievable *resolution*. The resolution can be defined as “the smaller detail that can be detected in an image, or, alternatively, as the smaller distance between two very small, but detectable, targets that could be distinguished in an image” (Nikolova (2011)). In practice, this means that if two objects are very close each other and their distance is shorter than the system resolution, they appear as a single object (Nikolova (2011)). The resolution is strongly dependent on the wavelength of the microwave radiation by means of the so called “diffraction limit”. Therefore, since it is dependent on the operational frequency and system bandwidth, and considering that these two parameters are also responsible of the maximum penetration depth, a tradeoff between the desired resolution and the achievable penetration depth has to be find out and took into account in the imaging system design.

On top of these two fundamental aspects, the patient position during the test has to be considered, since according on that, the hardware setup is different. The two most investigated positions of the woman during the diagnostic test are prone and supine, even if also the standing position could be possible. In the *prone position*, the woman is laid down with the face downwards and the imaged breast pending in a hemispheric tank covered by antennas and usually filled with a coupling liquid (if included in the system design). This configuration allows the scanning of the breast from different angles of view, usually provides higher values for the Signal to Noise ratio, and naturally reduces the unwanted noise due to the breathing movement of the patient (the chest wall is compressed against the table while the back is moving).

In the *supine position*, on the other hand, the woman is laid down with the face upwards. In this configuration, usually the coupling medium is not used, the breast thickness is naturally flattened thank to the gravity (reducing the path losses), and a planar array placed directly above the imaged breast is used. However, the fixed position of the array does not allow the breast scanning from different angles of view and the whole system suffers for lower values of Signal-to-Noise ratio. In addition, the unwanted movement of the patient for breathing has to be taken into account.

Another possibility could be the *standing* or *sitting position* with the breast compressed between two plates, using a planar array; however, this configuration has not been investigated since one of the will for a microwave imaging system is the patient comfort.

Microwave imaging techniques could be based on measurements in time or in frequency domain. In time domain, usually pulses are used as transmitted signals and are synthetized by doing the inverse Fourier transform of frequency measurements done with the VNA. In frequency domain, the measurements typically consist of broadband frequency sweep of the Scattering parameters. Usually these measurements are performed with the VNA and information on both amplitude and phase is collected.

Considering all the aforementioned aspects, several prototypes at microwave frequencies for breast cancer detection have been proposed worldwide; however, the relatively coarse resolution (Nikolova (2011)) for cancers within a particularly fat breast motivated our interest toward higher frequencies, in the mm-wave regime. If, indeed, in tissues with a greater fibro-glandular component the relatively large wavelength (dictated by the low frequency at play) is compensated by the high values of dielectric permittivity of these tissues, thus allowing a sub-centimetric resolution, the same argument cannot be applied to tissues with a high adipose component. In the latter, indeed, the large wavelength is not compensated by the high permittivity values; therefore, the resolution achievable in environments like this cannot be valid for early diagnosis.

Before 2014 (first experimental campaign performed by our research group at the European Institute of Oncology in Milan on human breast *ex-vivo* tissues), this part of the electromagnetic spectrum has never been investigated as a potential band of interest for non-shallow biomedical imaging applications, limiting the use of mm-waves and beyond (THz-regime) in biomedical context only for that applications for which the penetration depth is not a key parameter (Töpfer and J. Oberhammer (2015)). Till 2014, indeed, examples of application of millimeter-waves in medical field were only proposed for the blood glucose monitoring (Hofmann *et al.* (2013), Jean *et al.* (2008)), since it was demonstrated that the permittivity and the static conductivity of the blood depend on the glucose level; for the assessment of the corneal hydration; for the diagnosis of hidden caries instead of the X-rays; and for the detection and the monitoring of some pathological conditions of the skin. This last case represented the most promising application thanks to both the offered resolution, higher than the one offered by microwave systems, and the penetration depth within the skin, in the order of its thickness (some millimeters). For these reasons, it was proposed the use of mm-waves for the monitoring of wound healing (Hayashi *et al.* (2005), Janssen and Smulders (2012), Smulders (2013)), the study of edema and skin irritation (Nuutinen *et al.* (2004), Alanen (1999)), the evaluation of the effect of skin

treatments (Alekseev (2007), Alekseev (2008)), as well as the diagnosis of skin cancer (Mehta *et al.* (2006), Taeb *et al.* (2013), Caratelli *et al.* (2013), Pickwell *et al.* (2005)).

This interest about the use of mm-waves only for superficial applications is partially justified by the strong attenuations of the signal within the biological tissues, which becomes particularly marked when the wavelength decreases. However, the two experimental campaigns of dielectric characterization of human breast tissues performed in 2014 and 2016 at the European Institute of Oncology in Milan –described in Chapter I- have shown that the dielectric losses of some types of healthy tissues (particularly fat) are not as high as originally thought, so the signal attenuations are not so catastrophic, allowing in theory the detection of targets up to a few centimeters deep. Based on these findings, the potential of millimetre waves for the detection of malignant lesions with sub-centimetric resolutions (for early diagnosis) in particularly fat breasts has been explored in 2016 by means of the feasibility study of the mm-wave imaging system with central working frequency of 30 GHz –as summarized in Chapter III-. In addition to these considerations, the interest in the use of millimetre waves for breast imaging has also been stimulated by the latest technological developments in the field of automotive (car radar), security (body scanner), and communication (short-range links) markets that can now provide a suitable transmitters and receivers at a relatively moderate cost (Fleming (2015), Ahmed *et al.* (2013), Antes and Kallfass (2013)).

The work presented in this thesis was completely done in collaboration with the European Institute of Oncology (Italian acronym, IEO) in Milan and with the Laboratory of Bioengineering of the University of Pavia, since 2014. It was originally funded by the Italian Association for Cancer Research (Italian acronym, AIRC) and subsequently funded by the University of Pavia funding, Blue Sky Research Project, MULTIWAVE.

This Thesis is divided as follows. In Chapter I, the dielectric characterization of biological tissues (both animals and humans, both *ex-vivo* and *in-vivo*) in the frequency range [0.5-50] GHz is presented, together with the comparison between dielectric properties of animal- and human- derived *ex-vivo* samples as well as the identification of the hydration level as possible classifier (among other derived quantities) for the dielectric measurement data up to 50 GHz. In Chapter II, new mixtures based on cheap, easy-to-manage and safe components, mimicking the dielectric properties of all kinds of human breast tissues (both healthy and neoplastic) are presented, and a first model of heterogeneous breast phantom is proposed. In Chapter III, after a brief summary of the numerical and simulated feasibility study of the mm-wave imaging system with central working frequency of 30 GHz, the preliminary tests of the prototype at mm-waves on breast phantoms are shown. Then, some conclusion of this work and future perspectives are explained.

CHAPTER I

DIELECTRIC CHARACTERIZATION OF BIOLOGICAL TISSUES IN THE FREQUENCY RANGE [0.5-50] GHZ

Introduction

The use of microwave and millimetre waves in a biomedical contest is increasing and both therapeutic and diagnostic applications in this frequency range have been proposed since many years.

On top of a proper design of the system for the intended application, the exact and unambiguous knowledge of the dielectric properties of biological tissues is fundamental, as these describe the way in which the electromagnetic fields interact with, and propagate within, a tissue; therefore, the exact knowledge of these properties is the starting point for all possible microwave-based technologies.

The need of an accurate knowledge of the dielectric properties of biological tissues was originally related only to dosimetry studies (Rosen *et al.* (2002)). However, since nowadays the scenario is changed and several ultra-wideband microwave technologies both for diagnostic and for treatment purposes have been proposed and are currently investigated by several research groups worldwide (Converse *et al.* (2004), Yang *et al.* (2005), Klemm *et al.* (2009), Burfeindt *et al.* (2009), Nikolova (2011), Grzegorczyk *et al.* (2012), Fear *et al.* (2013), Bahramiabarghouei *et al.* (2015), Di Meo *et al.* (2017a), Summers *et al.* (2019)), from the beginning of the 20th century, several experimental campaigns for the determination of dielectric properties of biological tissues have been proposed both on animal and human tissues (*in-vivo*, *in-situ*, *ex-vivo*, and *in-vitro*), normal and malignant. The result of this movement is that nowadays it is available a huge amount of experimental data in a broad frequency (from 10 Hz to 50 GHz) and temperature (from around 25°C to around 60°C) range (Gabriel *et al.* (1996b), Lazebnik *et al.* (2006, 2007a, 2007b), Sugitani *et al.* (2014), Matellosio *et al.* (2017), Di Meo *et al.* (2018), Bonello *et al.* (2018)).

Among all possible applications, one of the most investigated was historically the use of microwaves for early-stage breast cancer detection, and this is the reason why a significant fraction of all the most extensive experimental campaigns has been performed on human breast *ex-vivo* samples. The origin of this interest lies in the fact that the human breast is mainly composed by adipose and fibro-glandular tissue, and therefore it can be classified as an organ with lower water content than the malignant tissues (characterized by higher blood perfusion, so higher water content), justifying the significant dielectric difference between these two categories.

Gabriel *et al.* (1996b) proposed an extensive database for the dielectric properties of animal- and human-derived *ex-vivo* samples, covering the frequency range from 10 Hz to 20 GHz, by means of three different experimental setups. All measurements were done at room temperature, and it was demonstrated that the dielectric differences between animals and humans are not systematic and sometimes they are lower than the differences existing between samples within animals and/or humans.

Ten years later, Lazebnik *et al.* (2006), by measuring the dielectric properties of 13 samples derived from 7 bovine and porcine livers both in the broad frequency ([0.5-20] GHz) and in the temperature (from room temperature to ~60°C) range, not only made available experimental data for the dielectric properties of this tissue up to 20 GHz, but also proposed a compact approach for the estimation of the dielectric properties of tissues as function of the frequency and the temperature. In addition, Lazebnik *et al.* (2007a, 2007b) provided also a very extensive database on dielectric properties of more than 400 human breast *ex-vivo* samples derived from more than 200 women in the frequency range [0.5-20] GHz, both normal and malignant, derived both from reduction surgeries (healthy tissues) and from cancer surgeries (healthy and malignant tissues).

Sugitani *et al.* (2014) presented the dielectric properties at room temperature of 102 samples derived from 35 patients, with ages from 33 to 88 years, undergoing breast cancer surgeries, in the frequency range [0.5-20] GHz, demonstrating the correlation between the volume fraction of cancer cells in the tumor tissue with its dielectric constant and conductivity. In particular, they demonstrated that the higher is the percentage of cancer cells within a tumor tissue the higher are its corresponding dielectric properties.

The results of the two experimental campaigns on human breast *ex-vivo* samples in the frequency range [0.5-50] GHz, presented in Matellosio *et al.* (2017) and Di Meo *et al.* (2018), are the object of the first part of this chapter; for this reason, all the details are left to the following of the chapter. In these works, for the first time, the tissue dielectric properties are measured up to 50 GHz. In addition, in Matellosio *et al.* (2017), a comparison with Lazebnik *et al.* (2007a, 2007b) is shown up to 20 GHz, and also in Martellosio *et al.* (2017) it is shown that there exist less than 10% difference in dielectric properties when considering tissues with low adipose content.

In all these experimental campaigns, the dielectric difference between healthy and malignant tissues is shown in all the investigated bandwidth. However, as it was underlined by Gabriel *et al.* (1996a) and by Porter *et al.* (2017), in some cases there is not a good agreement between the dielectric properties in literature, even when they are referred to the same organ.

This incongruity in the achieved results could be ascribable to several factors, from different measurement protocols used by various research groups to some intrinsic properties of the sample itself, and, for this reason, a significant number of works investigating the origin of these differences, as well as some causes for reflection were proposed.

The absence of a reliable and unambiguous measurement protocol (particularly important for the *ex-vivo* measurements), the impact of a not-perfect calibration procedure on the dielectric measurements, the tissue heterogeneity within the sensing volume of the probe, the time between the excision of the sample and the dielectric measurements, could be some of the main causes of this disagreement in the achieved results.

The measurement protocols adopted by Gabriel *et al.* (1996b), Lazebnik *et al.* (2006, 2007a, 2007b), Sugitani *et al.* (2014), Matellosio *et al.* (2017) and Di Meo *et al.* (2018), differs each other, and are summarized below.

In Gabriel *et al.* (1996b), dielectric measurements at body temperature on freshly excised ovine and porcine tissues, on human autopsy derived tissues, and human skin and tongue *in vivo* were presented. This experimental campaign was done by means of three experimental techniques (one automatic swept-frequency network and two impedance analysers), covering the whole frequency range from 10 Hz to 20 GHz. For what concerns animal tissues, the time between the death of the animal and the dielectric measurements was not exceeding 2 hours; while, for what concerns the human derived tissues the time was from 24 to 48 hours after

the death of the person. Samples in the order of 5 cm were used, because of the equipment required for the measurements at low frequency.

In Lazebnik *et al.* (2006), dielectric measurements on 7 freshly bovine and porcine livers were done. The time between the excision and the dielectric measurement was not exceeding 2 hours. From each liver, almost two samples with dimensions of approximately 5x10x3 cm^3 were derived. In order to avoid excessive desiccation, each sample was covered by aluminum foil and by an acrylic plate with proper holes allowing the insertion of the probe. After the sample was covered, it was placed in a laboratory oven at controlled temperature, and the dielectric measurements were done every 5 minutes during both the heating and the cooling phase. Samples were partially heated at body temperature (37°C) and partially at 60°C.

In Lazebnik *et al.* (2007a), the dielectric properties of healthy tissues derived from reduction surgery on 93 women were presented. The measurement protocol tuned in that framework is summarized here. All the dielectric measurements were done in the Pathology Department of two American Hospitals. After the reduction surgery, the exported tissues were transported from the operating theatre to the Pathology Department by means of proper sealed, heated and insulated containers for the humidity preservation. The time between the excision and the dielectric measurements was from 5 minutes to 5 hours. Each sample was extracted from the whole tissue immediately before the dielectric measurement. The diameter of each sample varied from around 2 cm to 10 cm. All measurements were conducted at room temperature. Information about the time between the excision and the dielectric measurement, the patient age and the temperature of the specimen at the time of the measurement were collected for each sample.

The measurement protocol proposed in Lazebnik *et al.* (2007b), for the healthy and malignant tissue measurements derived from cancer surgeries, is briefly described here. The samples healthy and malignant were derived from lumpectomies, mastectomies and biopsies at two different American Hospitals. In both the Hospitals, dielectric measurements were done in the Pathology Departments. Normal tissues near the margins of the excised specimens (away from the lesion) were measured. The time between the tissue excision and the dielectric measurement was in average around 1 hour, but in any case ranging from 11 minutes to 4 hours. The margins of each excised tissue were firstly marked with ink by the pathologist. After this, the pathologist cut a sample containing both healthy and malignant tissues and its dielectric properties were measured. Then, each measurement area was marked with another ink and the marked sample was processed by the pathologist. In this experimental campaign, the time between the excision and the dielectric measurement, the temperature of the sample at the time of the dielectric measurement, as well as the patient age were collected. Several samples at room temperature were measured.

In Sugitani *et al.* (2014), the study of the volume fraction of the cancer cells in the malignant tissue as responsible of the different dielectric properties was shown. The measurement protocol is briefly described here. The dielectric measurements were performed in the Department of Anatomical Pathology. The dimension of the excised breast tissue, derived from total or partial mastectomy surgery, varied from 5 to 30 cm in diameter. The tumors were measured in several locations. The time between the arrival of the tissue in the Anatomical Pathology Department and the dielectric measurements was around 15 minutes. The histology analysis of each tissue sample was done by visual inspection of its cross-section, from which the volume fraction of cancer cells in the tumor tissue was derived.

As for the details of the measured tissues, the measurement protocol adopted in Matellosio *et al.* (2017) and Di Meo *et al.* (2018) is left to the first section of this chapter.

Overall, the measurement protocols proposed by different research groups differ each other, in particular for what concerns the dimension of the sample and the time between the excision and the dielectric measurement,

and these differences could be possible responsible of the incongruity in the achieved results. The impact on the dielectric measurements of the tissue heterogeneity within the sensing volume of the probe, indeed, was recently investigated by Porter *et al* (2017). In particular, the contribution of the tissue composition to dielectric measurements within the sensing volume of the probe was studied, together with the quantification of the contribution to dielectric properties of tissues at differend depths within the measured samples. On the other hand, the impact on the measured data of the time between the excision of the sample and its dielectric measurement was analyzed by Shahzad *et al.* (2017). In this work, Shahzad *et al.* (2017), by measuring the dielectric properties of rat liver *ex-vivo* samples in the frequency range [0.5-20] GHz up to 3.5 hours from the excision, demonstrated the impact of the tissue dehydration on the measured dielectric properties. In particular, two sets of data were collected and discussed, that were directly above and slightly under the surface of the sample, demonstrating the strong impact (greater than 25% in both ε' and ε'') on the sample dielectric properties of the superficial water evaporation over time. In addition, Farrugia *et al* (in Farrugia *et al* (2016)) investigated the immediate changes in dielectric properties after excision, by comparing the dielectric properties of *in-vivo* and *ex-vivo* tissues derived by a colony of mice (more details on this paper will be given in the next section).
Moreover, Gabriel and Peyman (2006) paid attention to the impact of a not-perfect calibration procedure on the dielectric measurements. In their work, indeed, the uncertainty associated to dielectric measurements was investigated and quantified by doing repeated measurements on standard solutions (e.g., 0.1M NaCl) at 20°C.

From all these considerations, it is evident that the debate about dielectric properties of human tissues is still open. First of all, because for the aforementioned reasons, there is not a good agreement between the experimental data presented by different research groups, and second because, before 2014, experimental data for human tissues (in particular, breast) were available only up to 20 GHz.

For these reasons, in this chapter, a contribution to the debate about dielectric properties of biological tissues is given by means of three different analysis. In the first section, the two extensive experimental campaigns on human breast *ex-vivo* tissues up to 50 GHz, performed at the European Institute of Oncology in Milan in 2014 and 2016, are presented; in the second part of the chapter, a very extensive experimental campaign in the frequency range [0.5-50] GHz on animal- and human- derived tissues performed at the University of Malta, in the framework of the COST Action *MyWave*, are presented; in the last part of the chapter, the preparatpry *in-vivo* experimental campaign on malignant tissues of a relatively small colony of mice performed in collaboration with the European Institute of Oncology in Milan at the IFOM institute of Milan in the frequency range [0.5-50] GHz is presented.

The aim of the first section of the chapter is to present the results of the two experimental campaigns on human breast *ex-vivo* tissues performed at the European Institute of Oncology in Milan on healthy and neoplastic tissues, in the framework of a project funded by the Italian Association for Cancer Research, in the frequency range [0.5-50] GHz. Before 2014, dielectric properties of *ex-vivo* tissues were measured only up to 20 GHz, while for higher frequencies mathematical models were used to derive them. Therefore, in this chapter, this gap is bridged, and measurements as well as statistics up to 50 GHz are presented.

The second section of the chapter inserts in the framework of the open debate about the variability in dielectric properties measured by different research groups, even when referred to the same organ. In particular, since one of the possible causes of this variability is the absence of a reliable and unambiguous measurement protocol, a measurement protocol for *ex-vivo* tissues to be used as standard is proposed, in collaboration with the Department of Physics of the University of Malta and the medical staff both of the Department of Anatomy of the University of Malta and of the *Mater Dei* Hospital in Malta. In addition, on top of the definition of a proper measurement protocol to be used as a standard for the *ex-vivo* experimental campaigns, the investigation

of the sample hydration level as possible classifier for the dielectric measurement data is proposed as possible approach to better understand the origin of the dielectric difference between experimental data presented in literature. In this part of the chapter, also the comparison between dielectric properties of animal- and human-derived tissues (both homogenous and heterogeneous) up to 50 GHz is presented, since the works present in literature quantifying the possible dielectric difference between them are currently not extensive and, in any case, were performed at lower frequencies.

Finally, in the third section of the chapter, the *in-vivo* experimental campaign up to 50 GHz on malignant tissues of a small colony of mice is presented. This step is preparatory for the whole experimental campaign that will be performed at a later stage in collaboration with the European Institute of Oncology in Milan. The aim of this section is a step forward for the validation of the database on human breast *ex-vivo* tissues in an *in-vivo* environment; therefore, when both body temperature and blood flux are inevitably present.

Section I - Experimental campaign on human breast *ex-vivo* tissues

In this section, the results of two extensive experimental campaigns, performed at the European Institute of Oncology in Milan, in the broad frequency range from 500 MHz to 50 GHz are presented (Martellosio *et al* (2015, 2017) and Di Meo *et al* (2017b, 2018a)). These experimental campaigns involved 342 human breast *ex-vivo* samples (247 healthy and 95 neoplastic ones) derived from around 100 women of ages from 14 to 85 years; the two experimental campaigns were performed in 2014 and in 2016, involving both heathy and malignant tissues derived from lumpectomy, quadrantectomy or mastectomy surgical operations.

Measurement setup

For both experimental campaigns, the measurement setup was the same. In particular, the open-ended coaxial probe has been used as dielectric spectroscopy technique; therefore, dielectric properties of the Material Under Test (MUT) were measured by means of a reflectometry-based approach. The whole measurement setup was constituted by:

- the open-ended coaxial probe (Keysight 85070E Dielectric Probe Kit), able to perform suitable measurements in a wide frequency ([0.5-50] GHz) and temperature (from -40° up to 220°) range;
- a Keysight E8361C Vector Network Analyzer (VNA), to retrieve, display and store the dielectric properties of the MUT;
- a high-performance flexible coaxial cable (provided with the Keysight 85070E Dielectric Probe Kit), used to connect the coaxial probe to the VNA;
- a mechanical mover to move the MUT toward the probe avoiding any possible movement of the probe itself after the calibration procedure, and a digital balance to control the pressure applied on the MUT.

The involved coaxial probe is characterized by a small footprint; the diameters of inner and outer conductors are very small, 0.268mm and 1.6mm, respectively. They generate a quasi-static capacitor-like field, and to be almost sure of collecting about the 100% of the fringing field both in lateral and in range direction, samples with diameters of 4-5 mm with thickness of 2 mm (corresponding to the penetration depth in all kind of tissues for all the investigated frequencies) were used. The sensing volume of the probe was verified during a preparatory experimental campaign on animal meat performed at the beginning of 2014 at the Microwave Laboratory of the University of Pavia in the framework of the Bachelor thesis of the author of the present work. In that work, indeed, after a preliminary phase on standard liquids (e.g., methanol, ethanol, n-propanol),

lean and fatty meat with decreasing thicknesses (starting value: 1 cm) were measured in the frequency range [0.5-50] GHz and the thickness allowing to measure the support of the sample was discovered to be around 2 mm (Report prepared for IEO).

To remove spurious errors from the collected data, the coaxial probe was calibrated before each measurement session by means of three standards: open ended, short termination, and deionized water at a controlled temperature (room temperature, ~20 °C).
After the calibration, no movements of the probe were possible, in order to provide phase stability, fundamental especially at high frequencies. The air-presence removal between the coaxial probe head and the MUT was avoided by applying a small and controlled pressure on the MUT (with the mechanical mover and the digital balance), while the probe was fixed to a mechanical positioner.
Figure 1.1 represent the measurement setup, a sketch of the probe field is shown in Figure 1.2, and a photo of the measured *ex-vivo* samples is shown in Figure 1.3.
The probe head is always in contact with the sample surface, even if Figure 1.3 is misleading. It depends from the fact that the outer body of the probe, visible in Figure 1.3, is much larger (around 1 cm in diameter) than the sensing area (given by outer conductor of the coaxial probe, around 2 mm, not visible in Figure 1.3). Therefore, the part not in contact with the sample in Figure 1.3 is just the outer body.

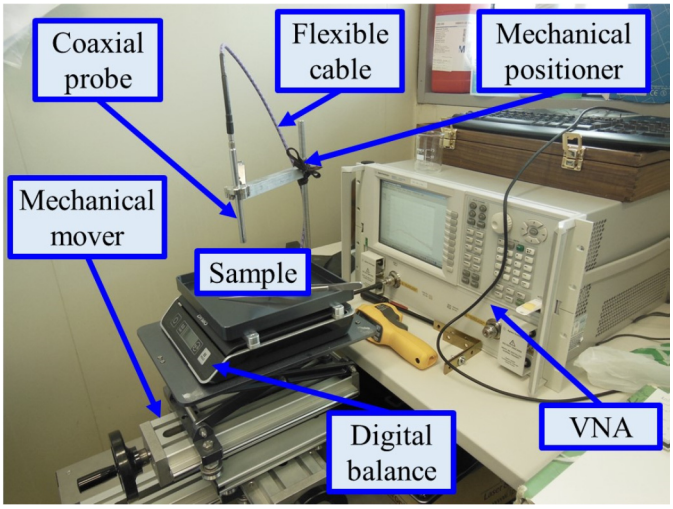

Figure 1.1. Experimental setup used for both experimental campaign on human breast *ex-vivo* tissues (Di Meo *et al.* (2018)).

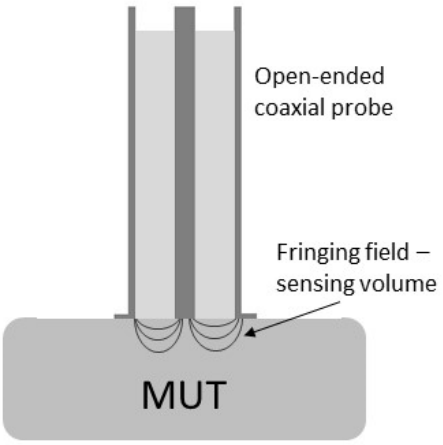

Figure 1.2. Sensing volume of the probe (Di Meo *et al.* (2018)).

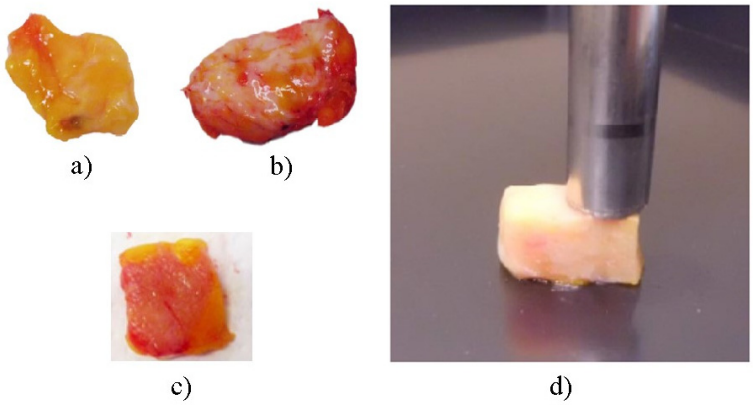

Figure 1.3. Photo of a measured *ex-vivo* a) Low density, b) High density, c) Neoplastic samples, and d) of the head of the probe in contact with a sample during dielectric measurement (credits of Martellosio *et al.* (2016)).

Measurement protocol

In both experimental campaigns (Martellosio *et al* (2015, 2017) and Di Meo *et al* (2017b, 2018a)) performed in 2014 and 2016, the dielectric properties of breast tissues were measured in the Pathology Department of the European Institute of Oncology in Milan after the surgical operations of lumpectomy, quadrantectomy or mastectomy, including both healthy and neoplastic tissues. The measurement protocol was established in a strict collaboration between the engineering and the medical staff, and among other aspects, it was aimed to the preservation of the sample humidity.

The transportation of the exported breast from the operating theatre to the Pathology Department was done in proper specimen bags, preserving the tissue humidity. Once in the Pathology Department, the sample was prepared by a pathologist to be measured by the engineer. The thickness of each sample, including normal and malignant tissue, was around 6 mm and the volume was from 700 mm^3 to 1500 mm^3. All the measurements were performed at room temperature (around 21°C), and the time between the excision and the measurement (from 6 minutes to 3 hours and half) was collected together with the temperature information. Depending on the dimension of each sample, the number of different dielectric measurements was variable. Each measurement side was marked with a proper ink to be distinguished by the other sides and to be easily identified in the subsequent examination done by the pathologist, defining the nature of the measurement side as well as the adipose content of the sample in that point. The pathological description of the nature of the sample was included in the database together with the electromagnetic response.

The measurement protocol used in these experimental campaigns is summarized in Figure 1.4.

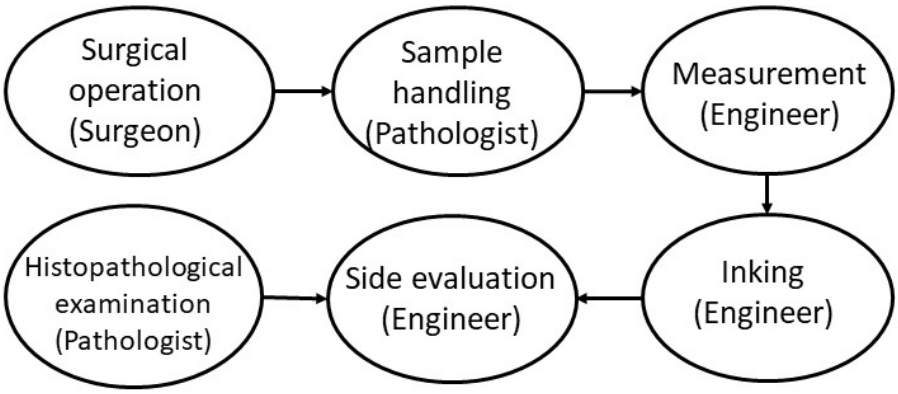

Figure 1.4. Measurement protocol for both the experimental campaigns (Di Meo *et al.* (2018)).

Measurement results including both experimental campaigns

The database derived from these two experimental campaigns involved 342 human breast *ex-vivo* samples (247 healthy and 95 neoplastic) derived by 98 women with different ages, from 14 to 85 years.
Several statistics were done on this complete database, as the derivation of the Cole-Cole parameters, an estimate of the *Sensitivity* and *Specificity* (two medical parameters commonly used to evaluate the quality of a diagnostic test of making reliable diagnosis, as explained in the following), and the correlation between the samples and the women age, as well as the correlation between the number of samples and their corresponding dielectric properties.

In Figure 1.5 a) and b) the comparison between dielectric properties of healthy and malignant tissues is shown in the frequency range [0.5-50] GHz for real and imaginary part, respectively. The shaded region is representative of one standard deviation.
In addition, due to the large variability in dielectric properties of normal tissues (visible in Figure 1.5), a classification between healthy samples based on their water content has been performed and, since there is not a standard way to classify biological tissues basing on their adipose or water content, the choice was as follows. Healthy tissues have been classified in *High* (adipose content lower than 20%), *Medium* (adipose content between 20 and 80%), and *Low* (adipose content greater than 80%) *density* tissues. Their dielectric properties have been compared to the ones of cancerous tissues, and the results are shown in Figure 1.6 a) and b) for real and imaginary part, respectively.

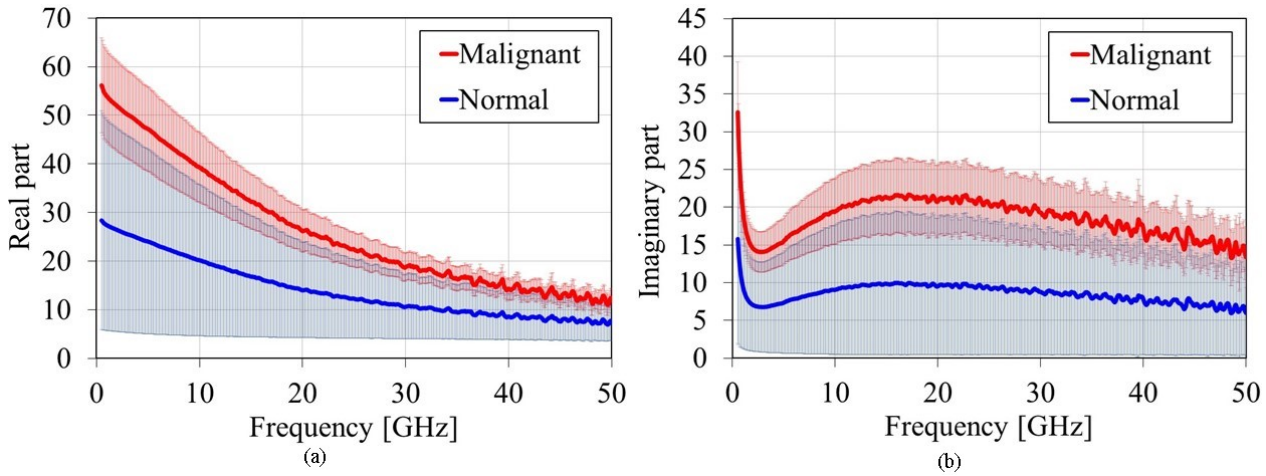

Figure 1.5. Characterization of the (a) real and (b) imaginary part of the relative dielectric permittivity for normal (blue line) and malignant (red line) tissues. The shaded region denotes the variable range at ± 1σ (Di Meo *et al.* (2018)).

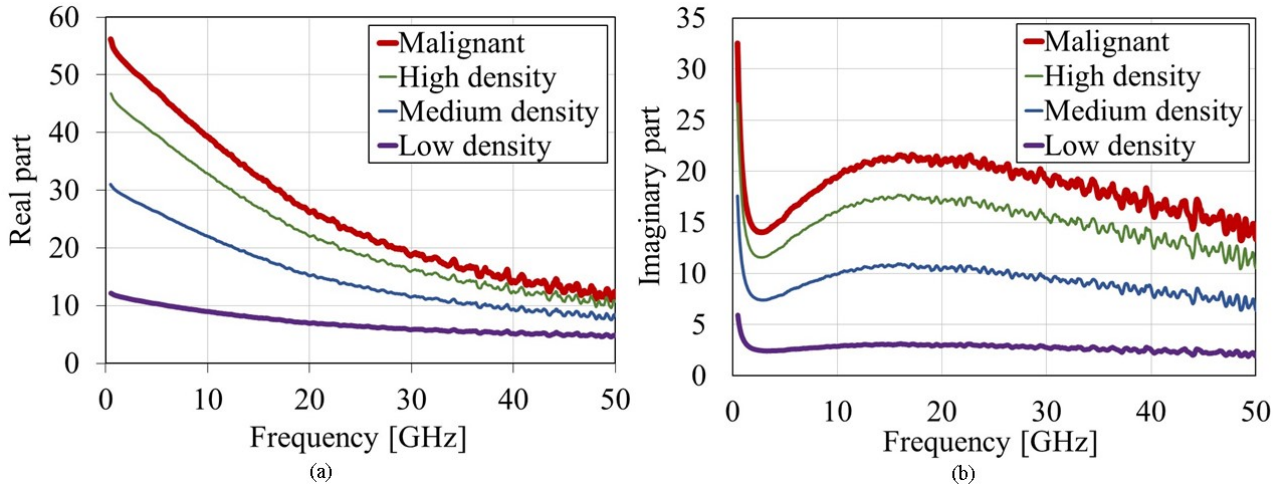

Figure 1.6. Differences between the average relative dielectric permittivity for healthy and cancerous tissues for (a) real and (b) imaginary part (modified picture starting from Di Meo *et al.* (2018)).

The dielectric properties of the tissues are significantly different in all the investigated bandwidth between healthy and malignant tissues, and the dielectric difference is strongly influenced by the adipose content of healthy tissues. In particular, the higher is the adipose content of the tissues the lower are the corresponding dielectric properties and, therefore, the higher is the dielectric contrast between them and malignant tissues.

Cole-Cole model

The dielectric properties of a biological tissue can be described by the Cole-Cole mathematical model, eq. below (Cole-Cole (1941)). This model allows to describe in compact form the behaviour of a material on a wide range of frequencies through the only knowledge of the five frequency-dependent parameters of which it is constituted. The equation is:

$$\varepsilon^* = \varepsilon_\infty + \frac{\varepsilon_s - \varepsilon_\infty}{1+(j\omega\tau)^{(1-\alpha)}} + \frac{\sigma_s}{j\omega\varepsilon_0}$$

where ε^* is the complex dielectric constant, ε_s and ε_∞ are the *static* and *infinite* dielectric constants, respectively, τ is the time constant, ω is the angular frequency, α is a constant that could assume value from 0 to 1 and describes different spectral shapes, σ_s is the static conductivity and ε_0 is the dielectric constant of the vacuum.

These parameters were computed using the least-square fitting to the average values of the measured dielectric properties.
Results are summarized in Table 1.1 for the average values of healthy and tumorous tissues, taking into account the difference in density between healthy tissues.

TABLE 1.1. COLE-COLE PARAMETERS DERIVED FOR NORMAL AND MALIGNANT TISSUES

	Normal			Malignant
	Low density	***Medium density***	***High density***	
$\Delta\varepsilon$	9,08	24,83	39,2	48,4
ε_∞	3,6	4,6	5,089	4,9
τ(ps)	17	11	9,58	9
α	0,19	0,14	0,1	0.09
σ_s	0,16	0,45	0,7	0.8

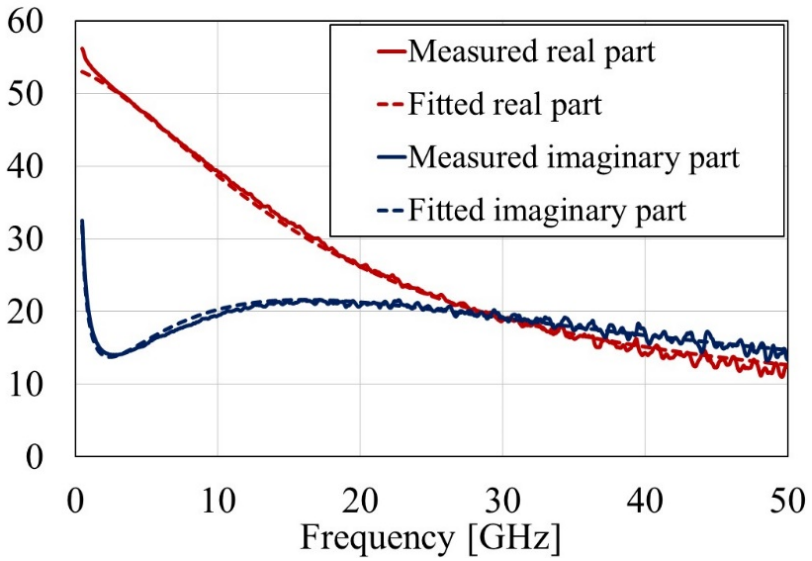

Figure 1.7. Comparison in real (red lines) and imaginary (blue lines) part between the measured (continuous line) and fitted (dotted line) data for the average malignant tissues (Di Meo *et al.* (2018)).

In addition, as an example, in Figure 1.7 the comparison in real and imaginary part between the measured and the fitted data for the average malignant tissues, as it is representative of all situations, and a perfect agreement is appreciable.

Sensitivity and *Specificity*

Generally, each diagnostic technique is evaluated basing on its quality of identifying as sick one person which is really sick, and on the contrary as healthy one person which is healthy. These two percentage values take the name of *Sensitivity* and S*pecificity*. In particular, *Sensitivity* is related to the True Positive (TP) rate, so sick people which are correctly classified as sick, while *Specificity* is related to True Negative (TN) rate, so healthy people which are correctly identified as healthy.
These two parameters are defined (Ghaaliq Lalkhen *et al* (2008)) as:

$$Sensitivity = \frac{Tp}{Tp+Fn}$$

$$Specificity = \frac{Tn}{Tn+Fp}$$

where, Tp stands for “True positive”, so one normal sample which is correctly classified as healthy, Fn stands for “False negative”, so the outcome of the test classifies as healthy one tumorous sample, Tn indicates “True negative”, so healthy samples correctly classified as healthy, and Fp is “False positive”, therefore healthy samples incorrectly classified as sick.
In the ideal case, a perfect diagnostic tool should have both *Sensitivity* and *Specificity* equal to 100%. However, in the real case, this is not possible to achieve; therefore, the goal is to design a system with these values as high as possible.

In this work, these two parameters were used to evaluate the capability of the coaxial probe of doing reliable measurements of the sample dielectric properties. These two parameters were computed by using one standard deviation as cut-off value; then, the pathology findings were used as benchmark to define the nature of the sample. In particular, the dielectric property values of each sample were compared to the strip of one standard deviation and the sample was considered a *True positive* if it was marked by the pathologist as a tumor tissue and its dielectric properties fall within the strip of one standard deviation for malignant tissues; it was classified as *True negative* if it was marked by the pathologist as a normal tissue and its dielectric properties fall within the strip of one standard deviation for healthy tissues; *False negative* if it was marked by the pathologist as a tumor tissue and its dielectric properties fall within the strip of one standard deviation for healthy tissues; *False positive* if it was marked by the pathologist as a healthy tissue and its dielectric properties fall within the strip of one standard deviation for malignant tissues.

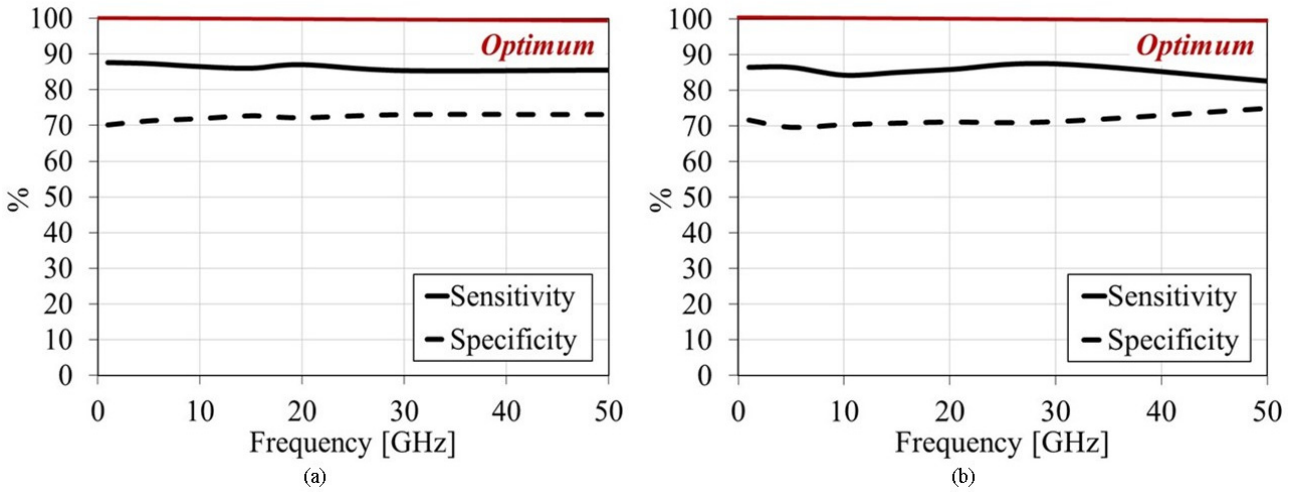

Figure 1.8. Sensitivity and Specificity calculated for (a) real and (b) imaginary part of the relative dielectric permittivity, where the continuous line represents the *Sensitivity* and the dotted line the *Specificity* (Di Meo *et al.* (2018)).

The results of this study performed considering all healthy tissues (also the ones with very *High density* tissues) are plotted in Figure 1.8, and values in the order of 85% for *Sensitivity* and 70% for *Specificity* are appreciable, showing the good capability of the coaxial probe of properly measuring the dielectric properties of healthy and malignant human tissues.

Number of samples and women versus women age strips

The whole database derived by the fusion of the two experimental campaigns on human breast *ex-vivo* tissues comprises samples derived from women of a very large span of age, from 14 to 85 years. Since breast cancer risk is depending on the woman age (web site, AIRC), to evaluate the distribution of the samples with respect to the woman age, in Fig. 1.9 the number of healthy and neoplastic samples with respect to the patient age

strips is plotted. In addition, because each woman produced more than one sample, in Fig. 1.10 the rate of women with and without breast cancer with respect to the patient age strips is shown.

From these figures (Di Meo *et al.* (2018b)), the similarity in considered patterns is evident; therefore, within certain limits it is possible to consider indifferently samples and women. It is also worth observing that the age distribution exhibits a peak for middle-aged women (45-56 years old), reflecting the probability distribution for a woman to undergo breast-related medical diagnosis and/or surgery in that age strip.

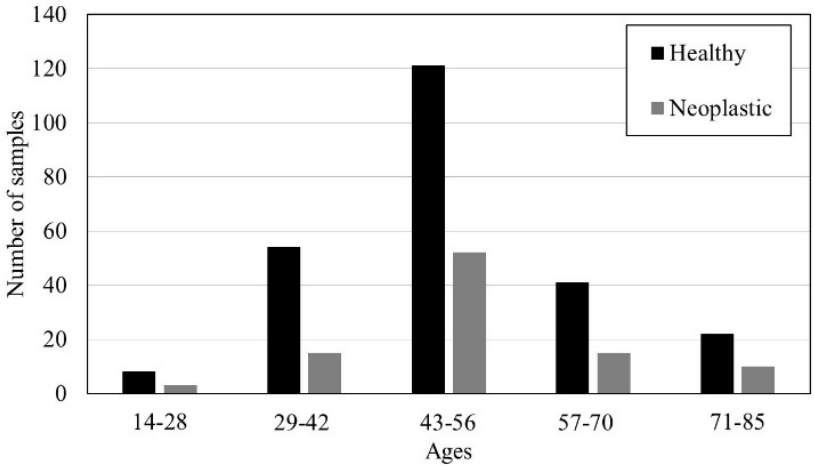

Figure 1.9. Rate of healthy and sick samples with respect to the patient age strips (Di Meo *et al.* (2018b)).

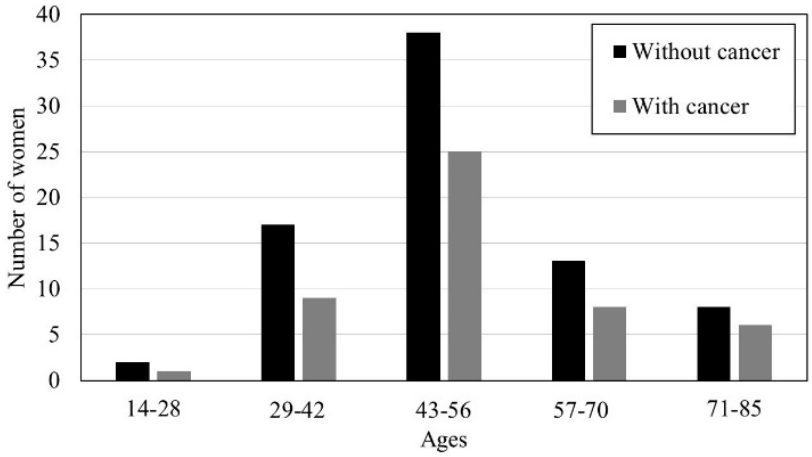

Figure 1.10. Rate of healthy and sick women with respect to the patient age strips (Di Meo *et al.* (2018b)).

Number of samples versus dielectric permittivity ranges

In previous paragraphs, it has been demonstrated the significant difference in dielectric properties of healthy and cancerous tissues considering all the measurements derived from the two experimental campaigns. Now, the whole range of dielectric permittivity, both for real and imaginary part, it is divided in nine strips and the number of samples falling in each of these ranges is counted, evaluated at 30 GHz. With this approach, the natural distribution of the samples within the strips of dielectric properties can be derived without dividing the samples on the base of their density.
Results for healthy tissues are shown in Figure 1.11a and 1.11b for real and imaginary part, respectively. In Figure 1.12a and 1.12b, results coming from cancerous tissues are shown for real and imaginary part, respectively.

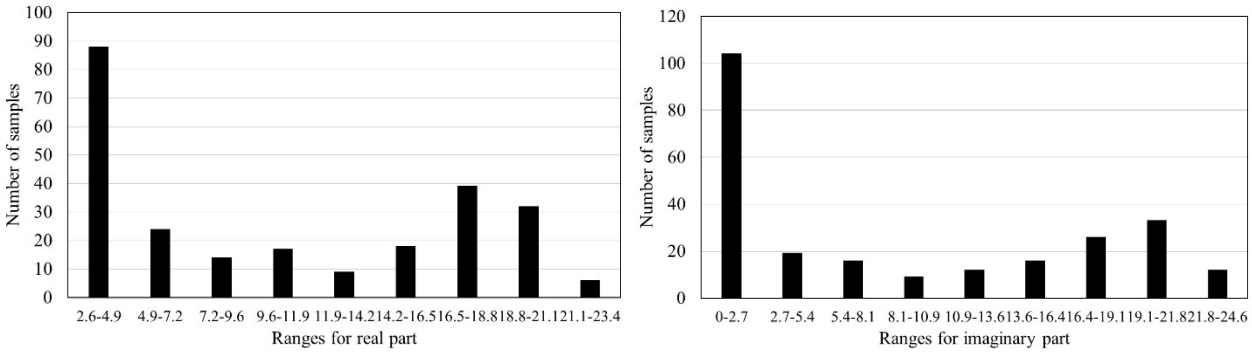

a) b)

Figure 1.11. Rate of healthy samples in each strip for (a) real and (b) imaginary part of the dielectric permittivity (Di Meo *et al.* (2018b)).

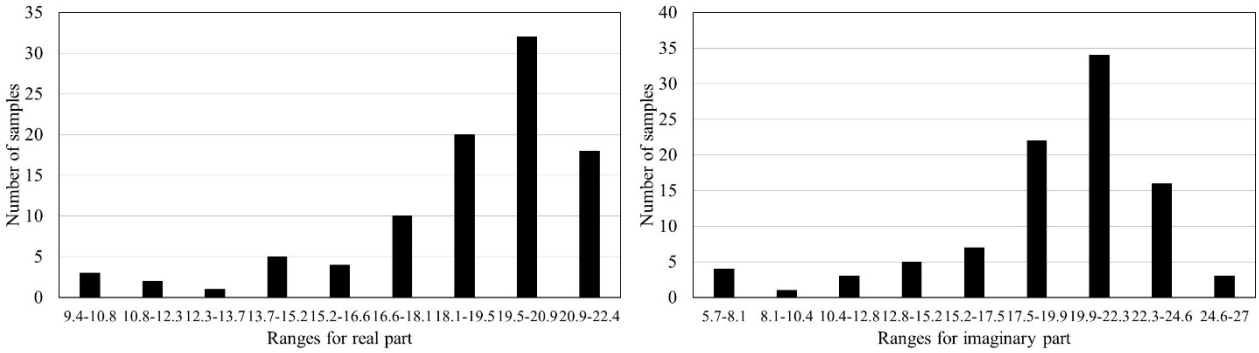

a) b)

Figure 1.12. Rate of malignant samples in each strip for (a) real and (b) imaginary part of the dielectric permittivity (Di Meo *et al.* (2018b)).

From Figure 1.11a-b it is evident that the highest number of measured healthy samples at 30 GHz have dielectric properties falling in the range from around 2.6 to 4.9 for the real part (35.6% of the healthy samples included in the whole database), and from 0 to 2.7 for the imaginary part (42.1% of the healthy samples included in the whole database). These outcomes are promising, because low values for the imaginary part of the dielectric permittivity are responsible of an acceptable signal attenuation, making possible the detection of non-subctutaneous lesions for a mm-wave imaging system, with central working frequency of 30 GHz. In addition, a significant dielectric difference between healthy and neoplastic tissues can be appreciated by comparing Figure 1.11 a-b) and Figure 1.12 a-b). Furthermore, the use of mm-wave as potential substitute of the actual X-ray mammography for women around 50 years is confirmed by the consideration that the distribution of dielectric properties is related to the age of the woman in terms of tissue adipose content. In this regard, it is important to note that, since the proposed imaging technique is intended to be a screening system even before diagnostics, the target population is not the whole female population (where the percentage of very fat breasts could not be high), but the one considered at risk (depending, among other things, by the woman age), where it is reasonable that you can expect an encouraging percentage of fat breasts.

Conclusions of this section

In this section, the results of the two experimental campaigns performed at the European Institute of Oncology in Milan, in 2014 and 2016, involving 342 human breast *ex-vivo* samples (247 healthy and 95 neoplastic ones) derived from around 100 women of ages from 14 to 85 years, are presented. Results show that there is a higher variability in dielectric properties of healthy tissues compared to malignant ones, and this is due to the different adipose percentage constituting them (tissue heterogeneity). The dielectric difference is particularly significant between healthy *Low density* tissues (adipose content ≥80%) and malignant ones, and this case is of particular interest for the aim of this thesis, breast imaging at mm-waves. In addition, the number of healthy samples

with low values for the dielectric permittivity corresponds to around 40% of the whole database and this number could be possibly related to the high concentration of women in the age strip around 50 years, where the use of breast cancer screening, diagnosis, and treatment techniques would be particularly beneficial. This study about the correlation between the distribution of the samples and the woman ages, possibly confirms the statistics about the increase in incidence rate of breast cancer for women of ages around 50 years old.
An additional promising consideration that can be derived from the study presented in this section is that also the significant dielectric difference at 30 GHz between the largest percentage of healthy and neoplastic samples is confirmed, and all the outcomes of this study are appealing for the detection of non-subcutaneous lesions with a mm-wave imaging system.

Section II - Experimental campaign on animal and human *ex-vivo* tissues

In this section, the results of the extensive experimental campaign on animal and human derived *ex-vivo* tissues performed at the University of Malta are presented. In particular, this measurement session inserts itself in the open debate about the strong variability of the dielectric properties of tissues presented in literature.
As said in the introduction of this chapter, there is not a good agreement in dielectric properties proposed by different research groups, even when they are referred to the same organ. One of the possible reasons for this variability is the absence of a reliable and unambiguous measurement protocol to be used as standard. Therefore, an *ad-hoc* measurement protocol for the measurement of animal and human derived *ex-vivo* samples was established in collaboration between the Department of Industrial and Information Engineering of the University of Pavia, the Department of Physics of the University of Malta, and the medical staff both of the Department of Anatomy of the University of Malta and the *Mater Dei* Hospital in Msida (Malta). In addition, since to better understand the origin of the dielectric differences among the results present in literature it could be useful the identification of some classifiers for the dielectric measurement data and since dielectric measurements of biological tissues are mainly performed in the γ dispersion region (mainly due to the polarization of polar molecules), the sample hydration level as possible classifier for the dielectric measurement data was deeply investigated and quantified, both for homogeneous and heterogeneous tissues.

The need of investigating the variation in hydration level between tissues as possible confounding factor in the measured dielectric data was recently underlined by Porter *et al.* (2018).

Shahzad *et al.* (2017) has demonstrated the impact of the tissue dehydration on the measured dielectric properties. In particular, two sets of data (directly above and slightly under the surface of the sample) were collected and discussed, and the results of this analysis shown a better stability over time of the dielectric properties measured under the surface, as this area is less exposed to air (therefore, to the dehydration effect), compared to the superficial dielectric measurements. However, this study did not enter in the detail of the hydration level of the samples, demonstrating only the strong impact (greater than 25% in both ε' and ε'') on the sample dielectric properties of the superficial water evaporation over time.

On the other hand, a first correlation between the sample dehydration level and its dielectric properties was shown by Pollacco *et al.* (2018). In particular, the impact of drying on the measured dielectric properties was demonstrated and quantified by measuring the dielectric properties of samples derived from 6 rats with different stages of dehydration, in the frequency range [0.5-50] GHz. Two kinds of tissues were considered in that analysis, fat and muscle, as representative of tissues with low and high water content, respectively, and it was demonstrated the decreasing in dielectric properties as the dehydration stage increases. In addition, both *in-vivo* and *ex-vivo* dielectric properties of the samples were measured at room temperature, and it was demonstrated that within certain sample dehydration levels the dielectric characteristics of *ex-vivo* samples could be representative of the *in-vivo* samples dielectric properties (as it was also demonstrated by Farrugia *et*

al. (2016)). In the work of Pollacco *et al.* (2018), a complete study of the variability of the dielectric properties of biological tissues with the sample dehydration level was done and for each percentage variation of sample hydration level the decreasing in dielectric properties was quantified up to the sample was completely dried.

Starting from these considerations, some novelties with respect to the state of the art, in particular Pollacco *et al.* (2018), are presented in this section. In particular, the hydration level of each single sample was used as a classifier of the variability between dielectric properties of the same organ in different animals (*inter*-animal variability), of different organs in the same animal (*inter*-organ variability), and of the same organ in animals and humans. In addition, the sample water content was correlated to the variation coefficient –ratio of the standard deviation with respect to the average- between the three independent measurements on each sample, quantifying the *intra*-organ variability both for homogeneous and heterogeneous organs.

For what concerns homogeneous tissues, liver and kidney cortex were chosen as representative organs of this category. In particular, 191 *ex-vivo* samples from liver and kidney cortex both of animal and of human (from beef, sheep, pigs and one human cadaver) were dielectrically characterized in the frequency range [0.5-50] GHz at room temperature (~20°C). While, lungs were chosen as representative of the category of heterogeneous tissues, and 93 samples from pigs, sheep and human being were measured. The human being is a 93 years old man, died for a cardiorespiratory arrest, provided by the Department of Anatomy of the Faculty of Medicine and Surgery of the University of Malta and by the *Mater Dei* Hospital staff. For each sample, three independent measurements were done, and the average, the standard deviation and the variation coefficient between them were computed. The water content of the samples was determined by means of the *loss-on-drying* approach. By doing this, the hydration level as a possible classifier of the *inter*- and *intra*-organ variability, of the *inter*- and *intra*-animal variability, as well as the variability between animals and humans was investigated from microwave to the millimeter-wave regime ([0.5-50] GHz).

Experimental setup

The open-ended coaxial probe was used as dielectric spectroscopy technique. In particular, dielectric properties of the tissues have been measured in the frequency range [0.5-50] GHz, by means of the open-ended slim coaxial probe.

The complete experimental setup was constituted both by the instrumentation for the dielectric measurements (Figure 1.13 a)) and by the equipment for sample drying (Figure 1.13 b) – c)).

In particular, the experimental setup for the measurement of the dielectric properties of the tissues involved:

- a two-port Vector Network Analyser (Rhode and Schwartz ZVA50), operating in the frequency range from 10 MHz to 50 GHz;
- a slim open-ended coaxial probe (Agilent Slim Form 85070) which enabled dielectric measurements in a broad frequency (from 500 MHz – 50 GHz) and temperature (from 0°C to 125°C) range, with its own software;
- a lab jack used to move the sample (named Material Under Test, MUT) toward the probe;
- a laptop to control the VNA by means of GPIB and to store data. The software Agilent 85070E was used to translate the reflection coefficient measured by the VNA in the complex dielectric permittivity.

The small diameter of the probe (2.2mm) allows measurements on very small samples (Agilent 85070E). The small dimension of the sensing region of the probe is fundamental for doing reliable measurements of the dielectric properties of biological tissues, as the heterogeneous tissue composition within the sensing volume of the probe, as well as the different contribution to the measured dielectric properties of tissues at different depths below the measurement area, it has been demonstrated having a strong impact in the measured dielectric properties (Porter *et al.* (2017)).

The water content of each sample was determined by means of the *loss-on-drying* approach (detailed in the next paragraph); therefore, the experimental setup for the determination of the sample water content included:

- an AE Adam Nimbus digital balance;
- a professional oven (Genlab Drying Cabinet).

The temperature of each sample was measured by a DTM 3000 - PT100 digital thermometer with an S-type probe attached and recorded.

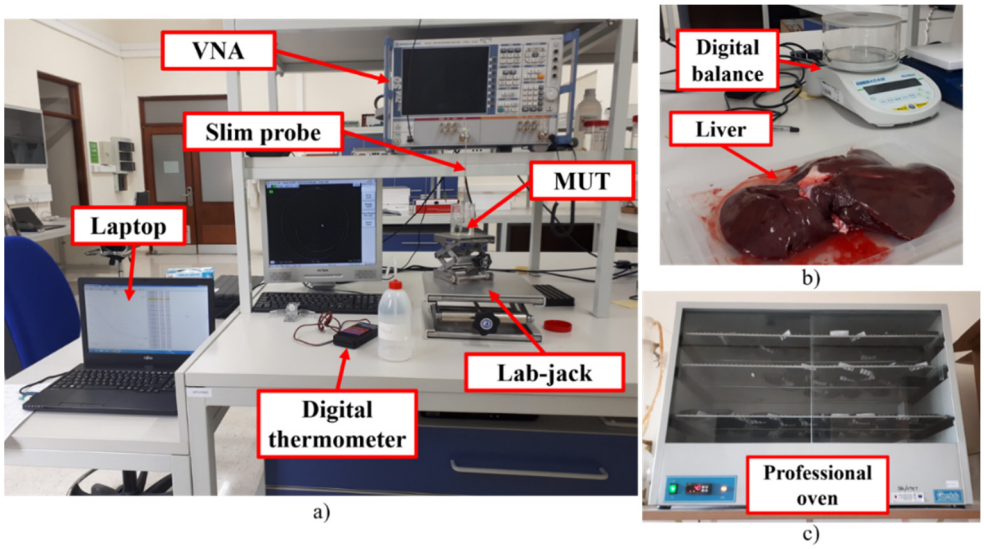

Figure 1.13. Experimental setup for the sample a) dielectric properties and b)-c) hydration level.

Measurement protocol

The proposed measurement protocol was intended to preserve the sample humidity and represents an attempt to standardize the measurement procedure for *ex-vivo* samples, since adopting the same approach could be fundamental to compare the results achieved by different research groups. This protocol was established in strict coordination between the Department of Industrial and Information Engineering of the University of Pavia, the Department of Physics of the University of Malta, and the medical staff both of the Department of Anatomy of the University of Malta and the *Mater Dei* Hospital in Msida (Malta), in order to allow for minimal sample preparation and thus minimal dehydration of the sample.

Before starting the measurement session, the whole system was calibrated by means of three standards: deionized water at room temperature (~20°C), air and short block. This procedure is as simple as delicate, since the system calibration is an integral part of the process for the dielectric measurements and an incorrect system calibration has a detrimental impact on the measured dielectric properties (Gabriel and Peyman *et al.* (2006)). In particular, a great attention must be paid for the measurements in water and with the short block, as problems like the presence of air bubbles on the tip of the probe and a not-perfect contact with the short block must be avoided.

After the calibration of the system, before starting the measurement of the dielectric properties of the tissues, the quality of the calibration was verified against published data (Gabriel and Peyman *et al.* (2006)) for a typical reference liquid (0.1M NaCl saline solution at room temperature, ~20°C), and if necessary the calibration was repeated (the calibration was considered acceptable for percentage variations lower than 1% for ε' and lower than 2% for ε'').

Animal meat was derived from fleshly killed animals, provided by the Public Abattoir of Malta. The transportation of the organs from the Public Abattoir of Malta to the Electromagnetic Laboratory of the

University of Malta was done by placing specimens in a sealed plastic bag, in order to preserve the humidity of the organs.

Once at the laboratory, the organs were dissected into smaller biological samples, having a minimum dimension of around 4x4x3 cm^3. The time between the death of the animal and the measurement of the dielectric properties did not exceed 4 hours. The time between excision of samples and their dielectric measurements varied from 30 seconds to 2 minutes.

The dielectric properties of each sample were measured at three independent locations on the sample, at room temperature (~20° C), and before the measurement the slim probe was inserted in a slit (done in each point of measurement), by paying particular attention to guarantee the contact between the face of the probe and the sample, in order to avoid any possible impact of the superficial water evaporation on the measured dielectric properties (Shahzad *et al.* (2017)). In Figure 1.14, a photo of a liver sample during dielectric measurements is shown.

After the dielectric measurements, the sample was weighted by means of a digital balance and its weight was stored. Then, the sample was put in a professional oven at a fixed temperature of 40° C for several days, depending on its dimension.

At the end of each set of measurements on one single organ, to avoid any possible corruption of the measured dielectric properties due to the drift of the calibration, the reference liquid (0.1M NaCl saline solution at room temperature, ~20°C) was re-measured to verify the stability of the setup, discarding if necessary all measurements collected in between two different calibration checks. In particular, these measurements were made taking care that the difference between the initial and final temperature of the solution was less than 1°C and a maximum tolerability of 2% was allowed (by way of example, at 5 GHz, equal to 0.27% for ε' and 1.93% for ε''; at 30 GHz, equal to 1.95% for ε' and 0.06% for ε'').

The weight of the sample was measured every day till its stabilization. The percentage of hydration (therefore, the percentage water content) for each sample was derived by comparing the weight of the completely dried sample to its original weight when fresh (*loss-on-drying* procedure).

The protocol adopted for human being samples was the same in all parts, except for the time between the death of the person and the dielectric measurements of the corresponding samples. Depending on the specific medical procedures *post mortem* (after the death), the time between the death and the dielectric measurements could not be lower than 12 hours, and in any case it was not exceeding 15 hours.
The proposed measurement protocol is summarized in the block diagram in Figure 1.15.

Figure 1.14. Photo of a liver sample during dielectric measurement with the probe inserted in the barely visible slit.

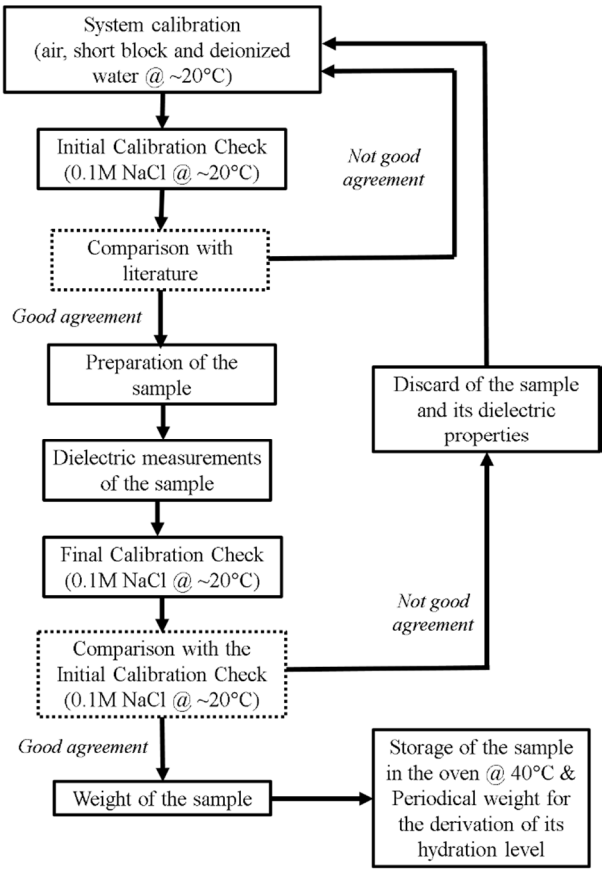

Figure 1.15. Block diagram of the proposed measurement protocol.

Analyzed homogeneous tissues

191 different *ex-vivo* samples both from liver and kidney cortex, both from animals and human, were measured. Of these, 82 samples were derived from kidney of 4 pigs, 3 sheep, 3 beef, and one human cadaver. The remaining 109 samples were derived from liver of 5 pigs, 3 sheep, 2 beef, and one human cadaver. The whole database is summarized in Table 1.2, where also the Water Content (WC) range, as well as the average Water Content, for each organ in each animal and in the human cadaver is displayed. In addition, the distribution of the samples with the percentage water content is shown in Figure 1.16 a) and b) for liver and kidney cortex samples, respectively.

In Figure 1.17, all the comparisons done about homogeneous organs are summarized.

TABLE 1.2. SUMMARY OF THE ANALYZED HOMOGENEOUS TISSUES.

Specie	Organ	#Samples	#Organs	#Animals	Range of WC (%)	Average WC (%)
Pigs	Liver	44	5	5	[67-72]	70
	Kidney	26	8	4	[72-82]	76
Sheep	Liver	28	3	3	[64-72]	68
	Kidney	14	6	3	[75-79]	78
Beef	Liver	28	2	2	[67-70]	69
	Kidney	36	6	3	[66-80]	75
Human	Liver	9	1	1	[72-77]	75
	Kidney	6	2	1	[74-80]	77

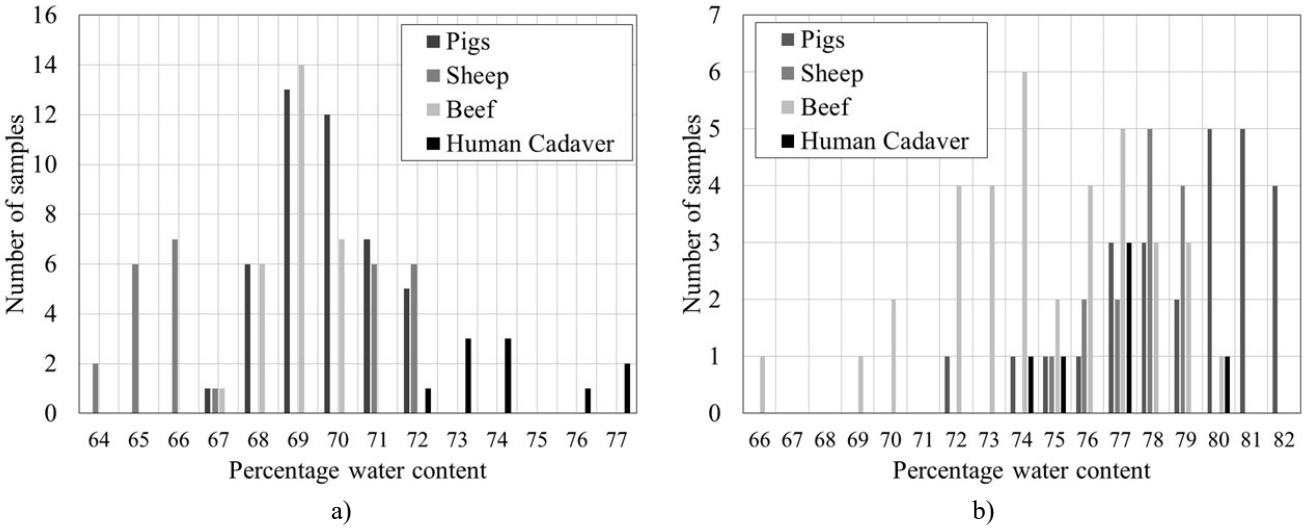

Figure 1.16. Distribution of the samples with the percentage water content for a) liver and b) kidney cortex samples.

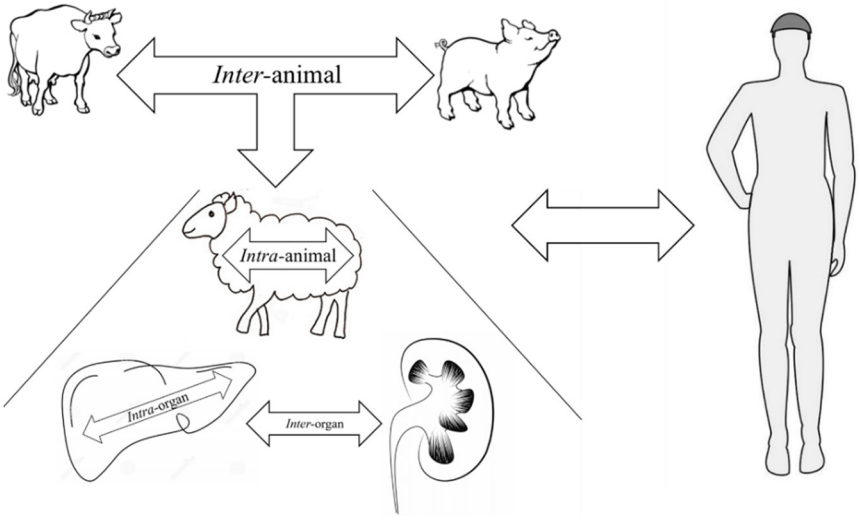

Figure 1.17. Schematic of the presented comparisons.

Results for homogeneous tissues

The dielectric properties of the samples were measured in 501 linearly spaced frequency points within the broad frequency range from 500 MHz to 50 GHz, and are described in terms of real and imaginary part of the dielectric permittivity.

The results of the experimental campaign are presented in terms of the *inter*- and *intra*-organ, the *inter*- and *intra*-animal variability, and the variability between animals and humans (Figure 1.17).

Inter-organ variability

From Table II emerges that liver and kidney cortex of all animals are characterized by a different water content. In this paragraph, the dielectric properties of liver and kidney cortex both for each animal and for the human cadaver are shown, in order to evaluate the *intra*-animal and *inter*-organ variability. In Figures 1.18 a)-b), 1.19 a)-b), 1.20 a)-b) and 1.21 a)-b) the comparison between dielectric properties, in the frequency range [0.5-50] GHz, of liver and kidney cortex for real (a) and imaginary (b) part of pigs, sheep, beef, and human being, respectively, is shown.

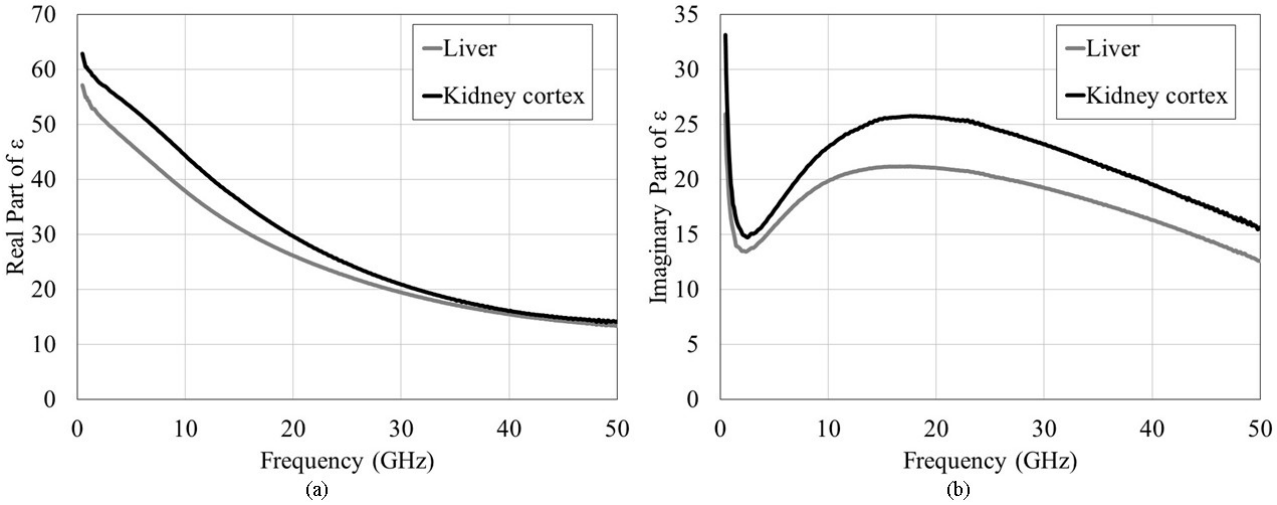

Figure 1.18. Comparison between dielectric properties of porcine liver and kidney cortex for a) real and b) imaginary part.

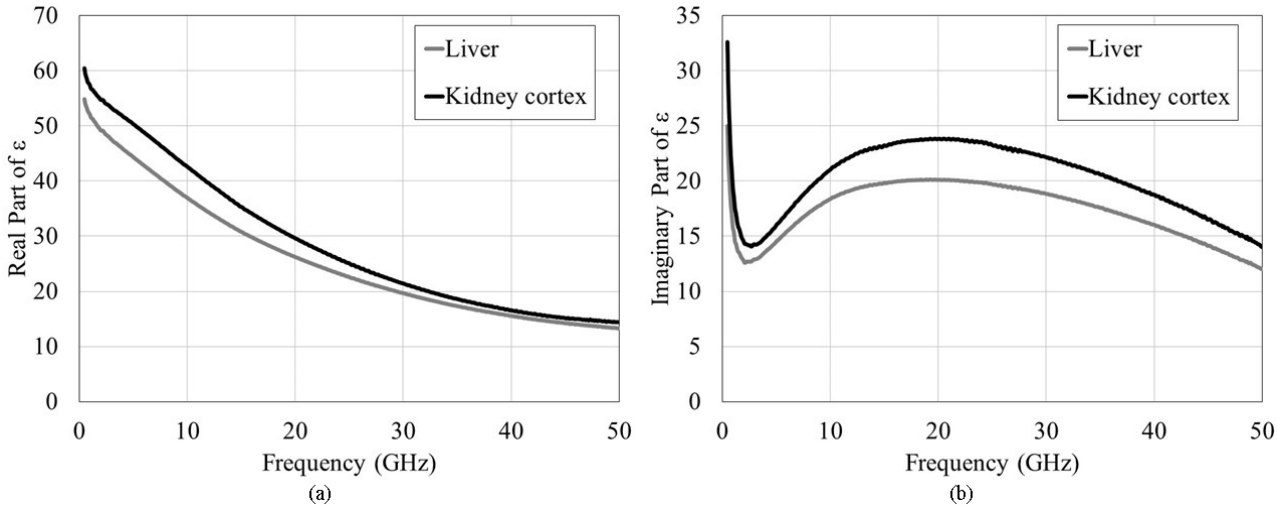

Figure 1.19. Comparison between dielectric properties of sheep liver and kidney cortex for a) real and b) imaginary part.

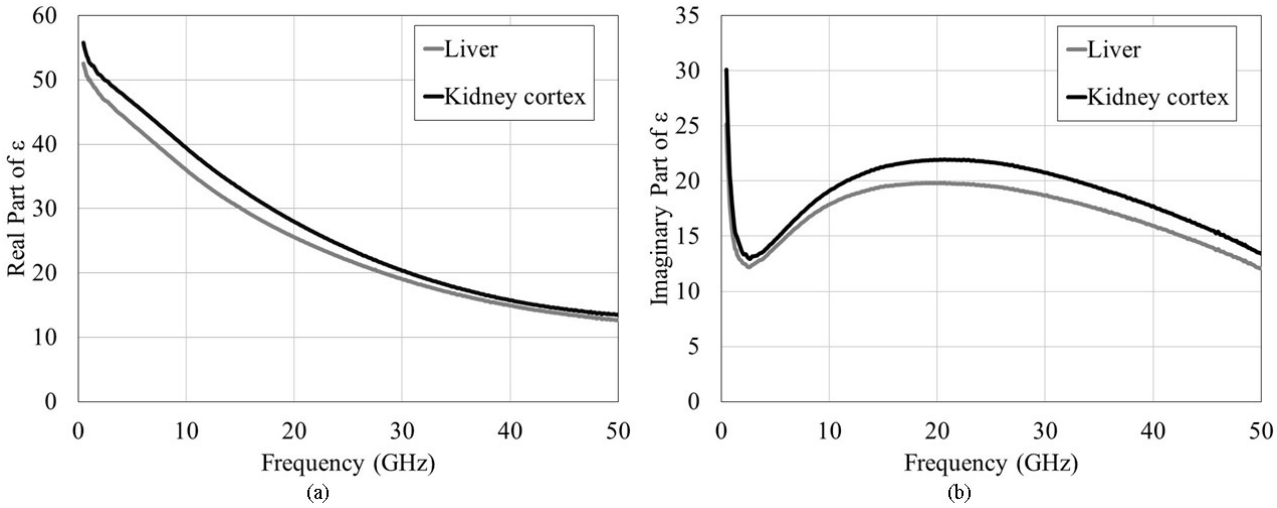

Figure 1.20. Comparison between dielectric properties of beef liver and kidney cortex for a) real and b) imaginary part.

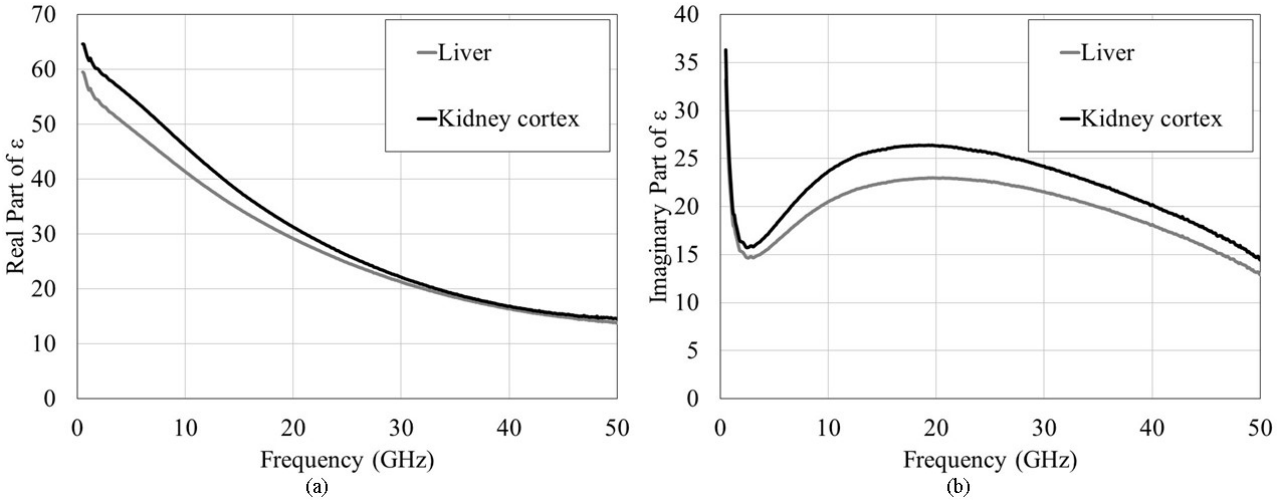

Figure 1.21. Comparison between dielectric properties of human liver and kidney cortex for a) real and b) imaginary part.

The dielectric properties for kidney cortex are higher than for liver in all animals, in line with the higher average water content of kidney with respect to liver (from 6 to 10 %). This result is partially demonstrated also for the human being, where dielectric properties of kidney cortex are still higher than the ones of the liver, as the corresponding average water content; however, the number of samples in this case is very limited and, in addition, all of them were derived from only one person, furthermore very old. For these reasons, it is reasonable to think that the limited number of samples involved in this analysis, as well as the age of the human being, are the main responsibles for the very small difference in average water content between the two organs (2%), highlighting the need of validating this result on a larger number of samples.

Therefore, from these graphs it could be possible to derive the conclusion that the organ hydration level can be used as a classifier for the *inter*-organ variability both within the same animal and, probably, human cadaver.

Inter-animal variability

In this paragraph, the results of the comparison between dielectric properties of liver and kidney cortex for the three animals are presented. In particular, the *inter*-animal variability was investigated in order to evaluate if a significant dielectric difference exists between the same organ in different animals.

The reference to human organs is not mentioned, as the variability between the dielectric properties of the animals and humans is left to the end of this section.

Figure 1.22 (a) and (b) show the comparison between the dielectric properties of pig-, sheep- and beef-derived liver for real and imaginary part, respectively. In the same way, Figure 1.23 (a) and (b) show the comparison between the dielectric properties of pig-, sheep- and beef- derived kidney cortex for real and imaginary part, respectively.

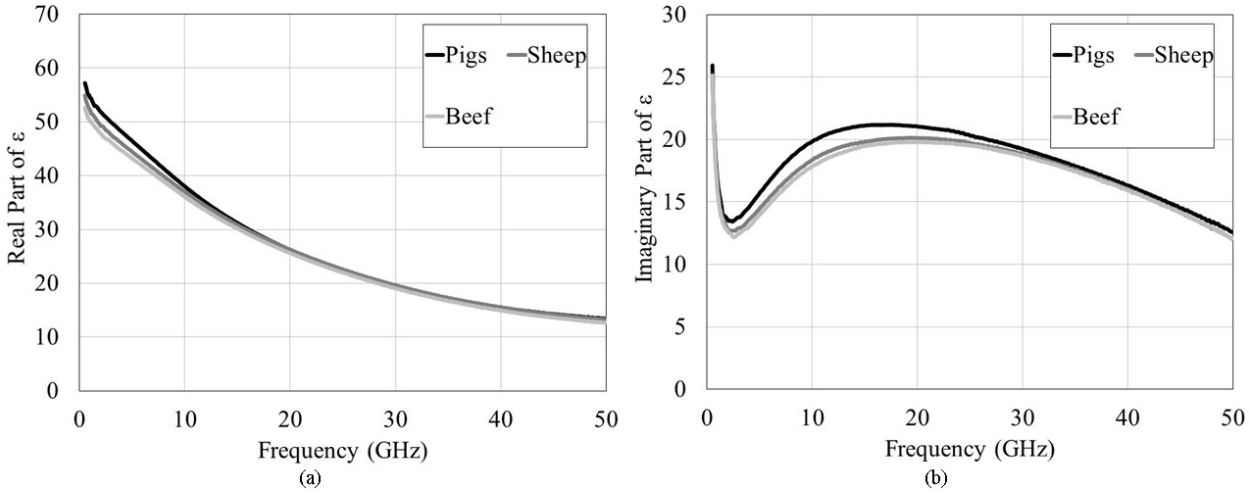

Figure 1.22. Comparison between the dielectric properties of liver derived from pigs, sheep and beef for a) real and b) imaginary part.

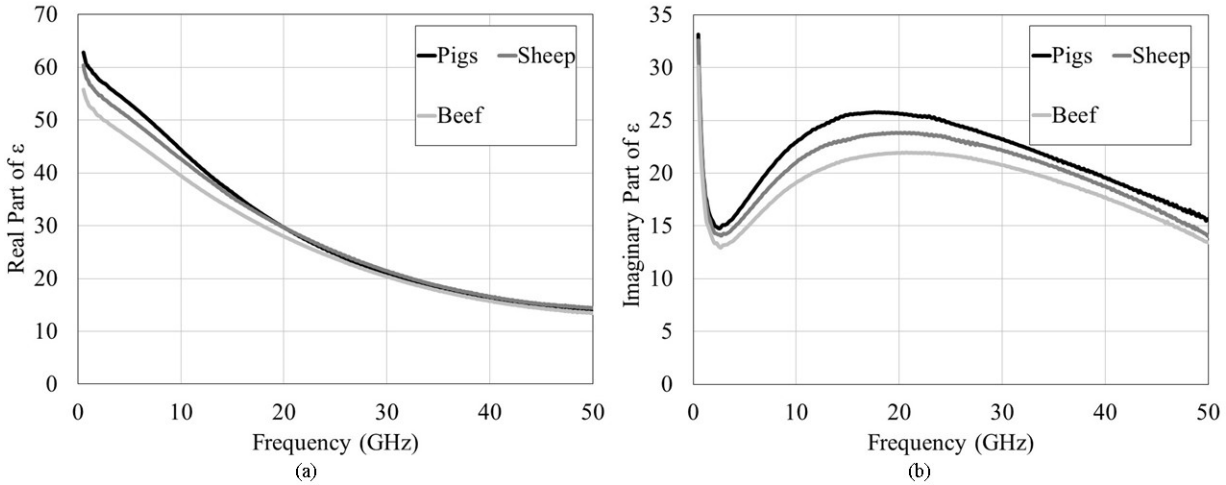

Figure 1.23. Comparison between the dielectric properties of kidney cortex derived from pigs, sheep and beef for a) real and b) imaginary part.

These graphs show that the dielectric difference between liver of different animals is not significant in all the investigated bandwidth. This could be justified by the not significant difference in water content among the liver of different animals (in average: 70% for pigs, 68% for sheep, and 69% for beef), not exceeding 2%. Therefore, since in this case the difference in water content of liver in the three animals is not significant, the hydration level cannot be used as a classifier for the *inter*-animal variability about this organ (at least considering this number of samples). The same conclusions could be derived for kidney cortex, where the difference in water content among different animals is not exceeding 3% (in average: 76% for pigs, 78% for sheep, and 75% for beef).

These results are in qualitative agreement with the main results obtained by Pollacco *et al.* (2018), that has demonstrated that variations in water content of less than about 10% cannot be systematically correlated to a significant difference in dielectric properties.

Intra-organ variability

In this paragraph, a different analysis is presented. In particular, the percentage variation coefficient (ratio of the standard deviation and the average) between the three measurements done on each sample is correlated

to its percentage water content. Therefore, now, the impact of the sample water content on the variability of the dielectric measurement data is analyzed.

The main idea is to investigate if the sample hydration level could still be used as a classifier for the dielectric measurement data, also within the same organ (where it was demonstrated that it is not possible to find a direct correlation between different sample water percentages and their dielectric properties). To do this, two frequencies were chosen, one in the microwave and one in the millimeter wave regime, 5 GHz and 30 GHz, as these are representative of the behavior of the quantity of interest in all the investigated bandwidth.

In Figure 1.24 a)-b), the correlation between the percentage variation coefficient and the liver samples hydration level for the three animals and for the human cadaver is shown at 5 GHz; while, in Figure 1.25 a)-b), the same statistics referred to the same organ are shown at 30 GHz, for real and imaginary part, respectively.

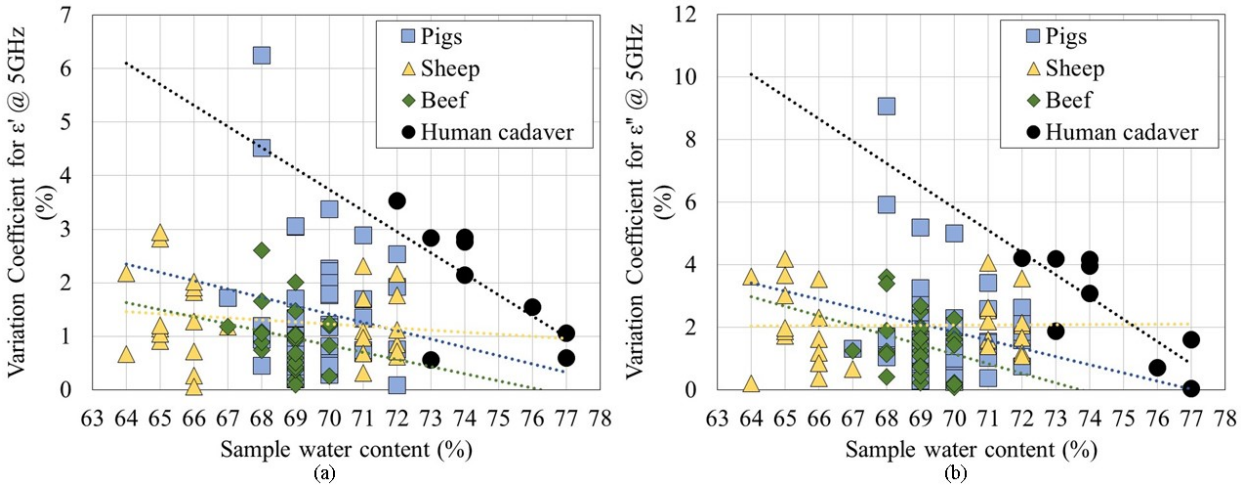

Figure 1.24. Correlation between the percentage variation coefficient and the liver samples hydration level for the three animals and for the human cadaver at 5 GHz for a) real and b) imaginary part.

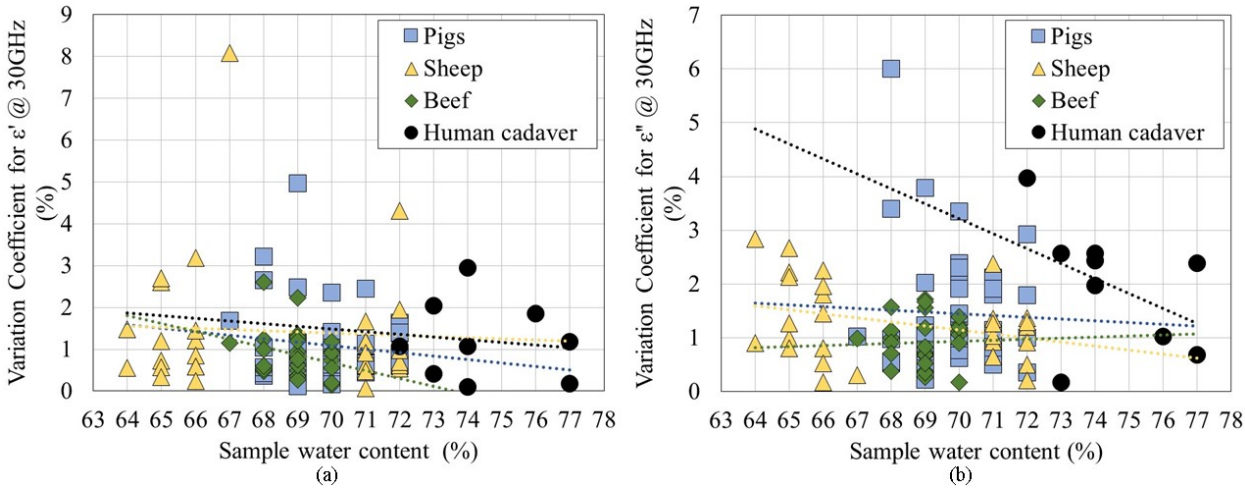

Figure 1.25. Correlation between the percentage variation coefficient and the liver samples hydration level for the three animals and for the human cadaver at 30 GHz for a) real and b) imaginary part.

In the same way, in Figure 1.26 a)-b), the correlation between the percentage variation coefficient and the kidney cortex sample hydration level for the three animals is shown at 5 GHz; while, in Figure 1.27 a)-b), the same statistics referred to the same organ are shown at 30 GHz, for real and imaginary part, respectively.

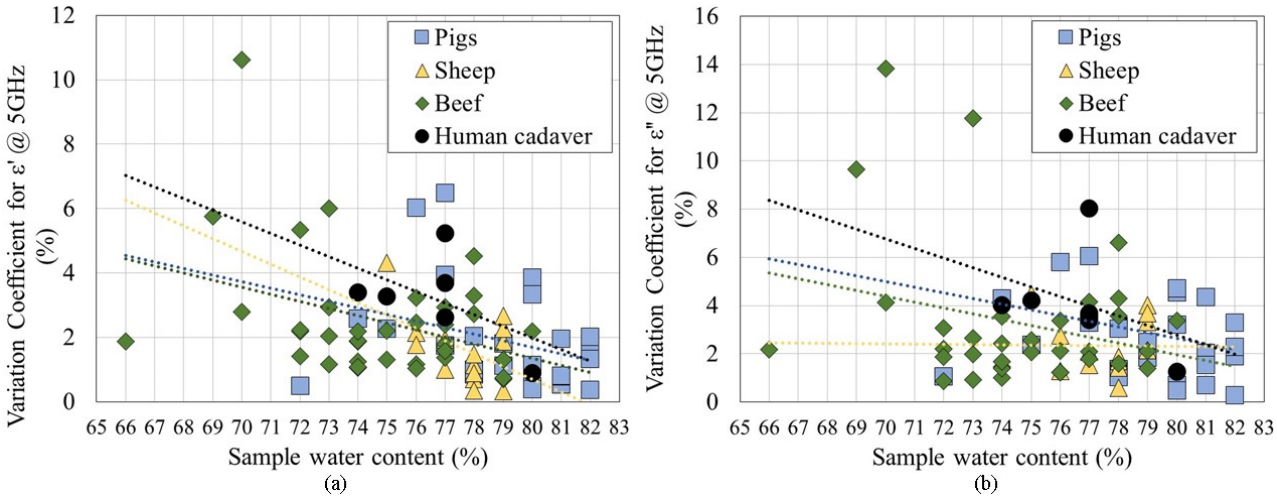

Figure 1.26. Correlation between the percentage variation coefficient and the kidney samples hydration level for the three animals and for the human cadaver at 5 GHz for a) real and b) imaginary part.

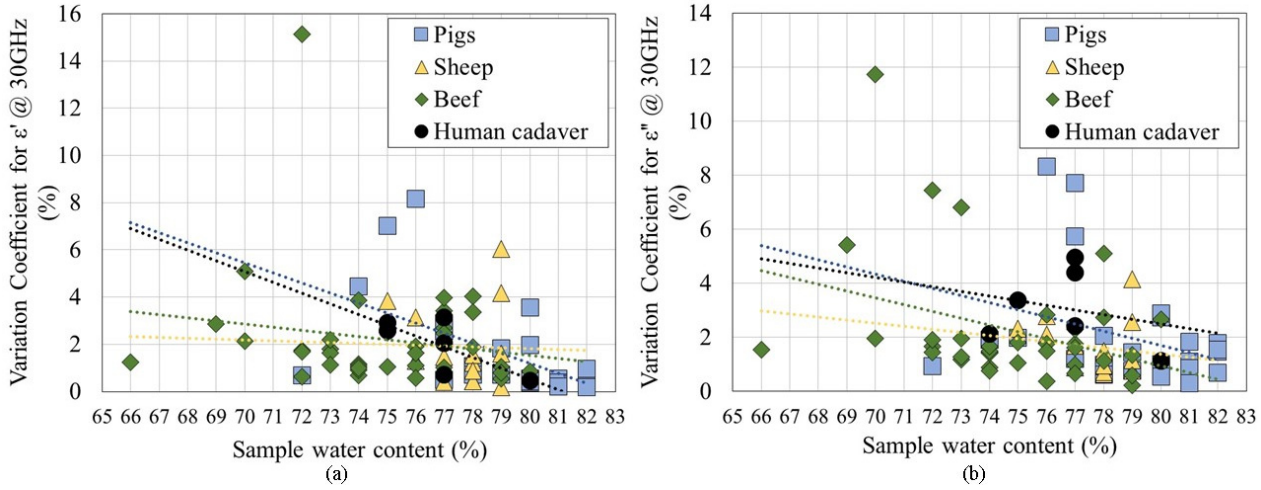

Figure 1.27. Correlation between the percentage variation coefficient and the kidney samples hydration level for the three animals and for the human cadaver at 30 GHz for a) real and b) imaginary part.

In these graphs (Figures 1.24 a)-b), 1.25 a)-b), 1.26 a)-b), 1.27 a)-b)), the dotted lines are representative of the trend for each case. What is clear from these graphs is that for all organs in all animals, as well as for the human being, it is the macro-trend of the correlation between the variation coefficient (both for real and imaginary part of the dielectric permittivity) and the water content of the sample. In particular, these graphs show that the percentage variation coefficient between the three measurements made on the same sample decreases as its water content increases. However, due to the concentration of the samples in a limited range of water content (inevitable, since the statistics are made considering limited sample quantities, compatibly with the relatively short times of the entire experimental campaign), it should not be surprising if there are some outliers, i.e. countertrend lines (a result that we believe to be anti-physical) in which the percentage variation coefficient increases slightly as the water content increases; we expect that these ambiguities can disappear by repeating these statistics on a larger database of samples.

Hence, ultimately, it can be concluded that the higher the water content and the lower the expected variability between dielectric measurements made at different points in the same sample. Therefore, we can derive the conclusion that the hydration level of the sample can still be used as a classifier for dielectric measurement data between samples of the same organ, where the difference in water content between individual samples is too small to be directly related to the different dielectric properties measured, and this information could be used in the future to have an idea about the water content of the measured samples even before its histological analysis or the evaluation of the water content by different approaches.

Variability between animals and humans

In this section, the dielectric properties of liver and kidney cortex between animals and human are compared in all the bandwidth, from 500 MHz to 50 GHz.

In Figure 1.28 a) and b) the average dielectric properties of liver from pigs, sheep, beef and the human cadaver are shown, for real and imaginary part, respectively. In similar way, in Figure 1.29 a) and b), the average dielectric properties of kidney cortex from pigs, sheep, beef and the human cadaver are shown, for real and imaginary part, respectively. In addition, to highlight the difference at low frequencies (where the most common applications are conceived), between measurements on animals and on humans, in Figures 1.30 a)-b) and 1.31 a)-b) the comparison within the reduced frequency axis [0.5-10.5] GHz is shown for real (a) and imaginary (b) part of liver and kidney cortex, respectively.

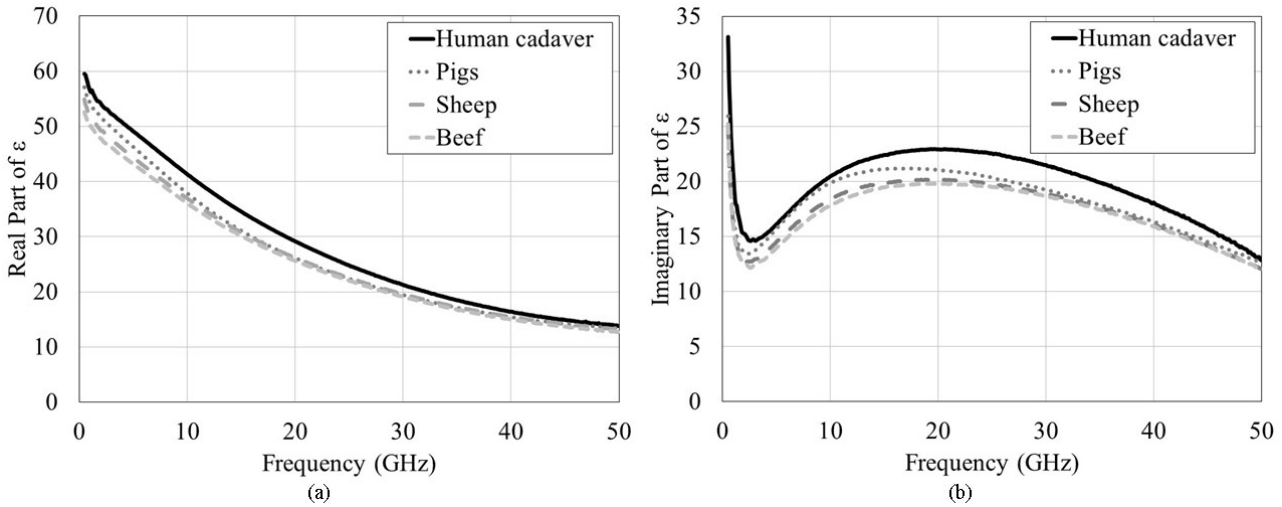

Figure 1.28. Comparison between the dielectric properties of liver derived from pigs, sheep, beef and human being for a) real and b) imaginary part.

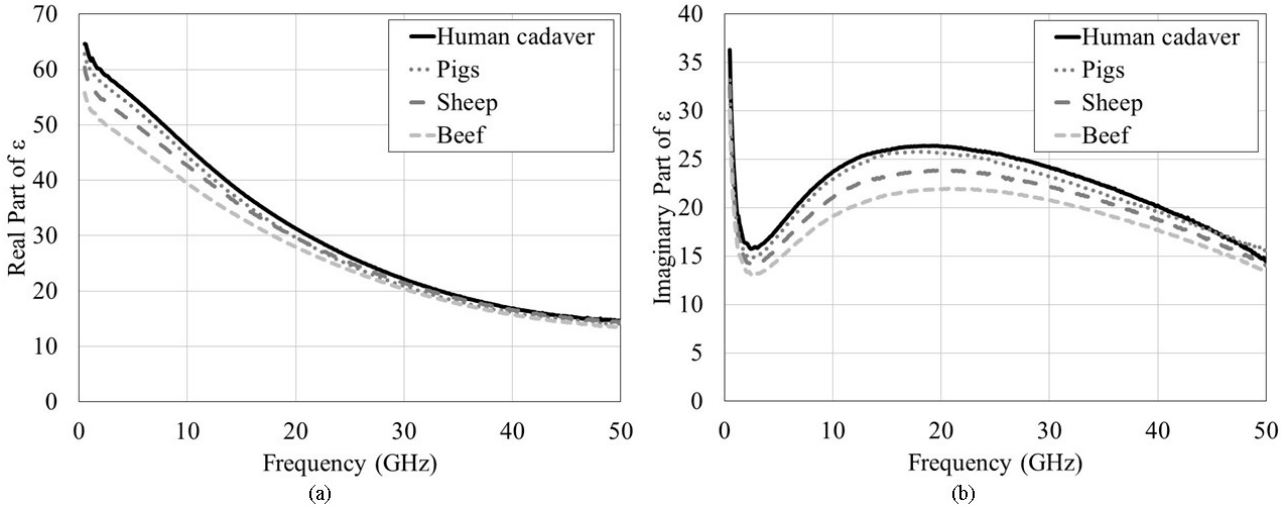

Figure 1.29. Comparison between the dielectric properties of kidney cortex derived from pigs, sheep, beef and human being for a) real and b) imaginary part.

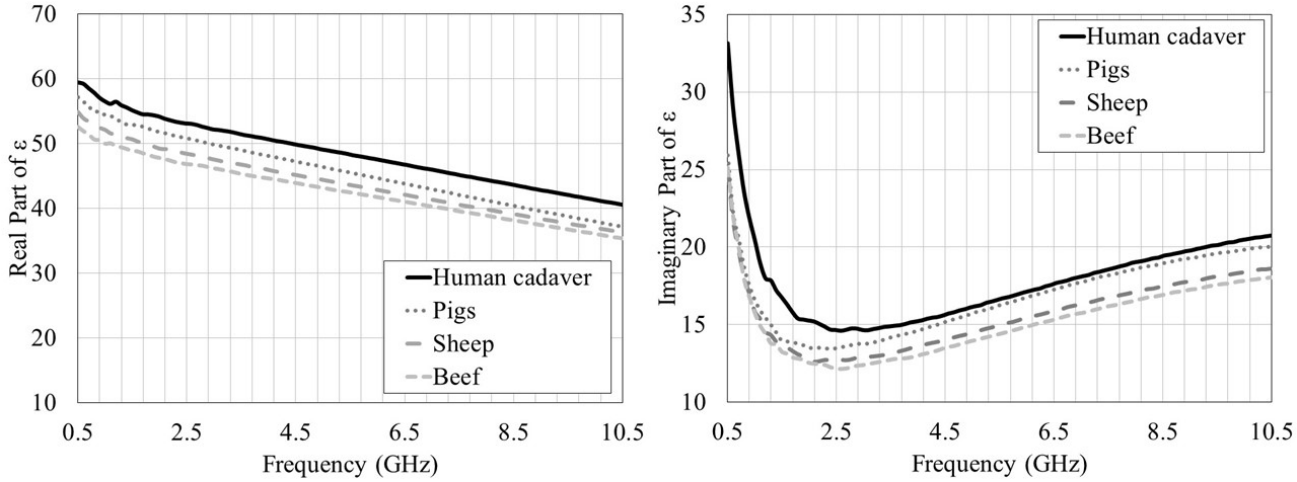

Figure 1.30. Comparison between the dielectric properties of liver derived from pigs, sheep, beef and human being for a) real and b) imaginary part in the frequency range [0.5-10.5] GHz.

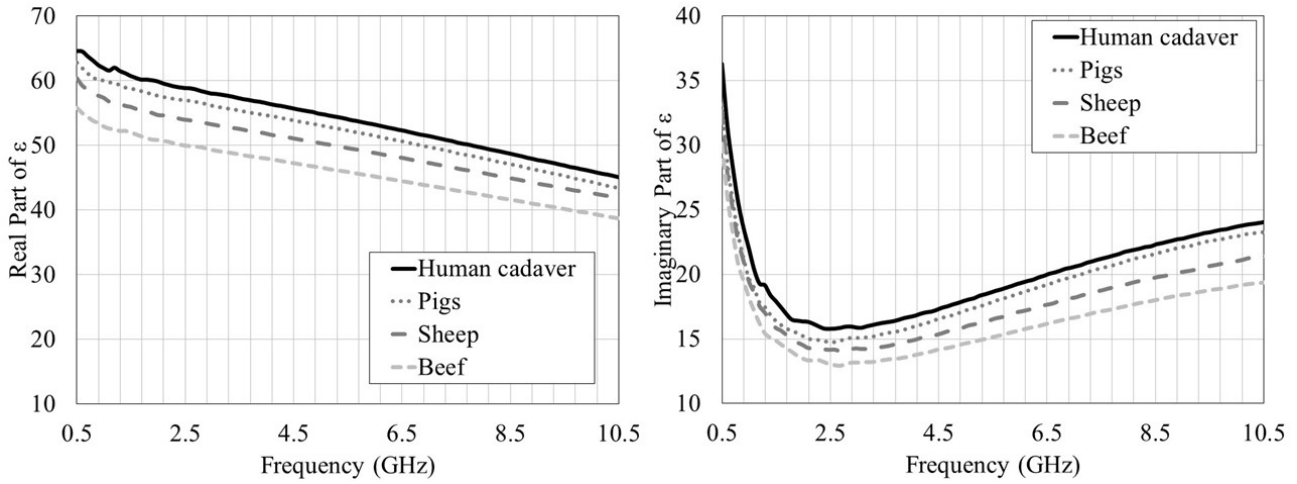

Figure 1.31. Comparison between the dielectric properties of kidney cortex derived from pigs, sheep, beef and human being for a) real and b) imaginary part in the frequency range [0.5-10.5] GHz.

The results show that the difference in dielectric properties is not significant, between all animals and the human cadaver, and in any case are lower than the difference among the three animals itself both for liver and for kidney cortex (in Table 1.3 and Table 1.4 the values of the standard deviations both for liver and for kidney cortex at 5 and 30 GHz are shown). These outcomes are completely preliminary, as it was possible to include in the experimental campaign only one human cadaver; however, they are in line with the literature. The discussion about the difference in dielectric properties between them is, indeed, investigated since many years, and both Stuchly *et al.* (1982) and Gabriel *et al.* (1996b) shown that a not significant statistical difference is present.

TABLE 1.3. STANDARD DEVIATION FOR LIVER SAMPLES AT 5 AND 30 GHZ.

Specie	Re(ε)* at 5 GHz	Im(ε)* at 5 GHz	Re(ε)* at 30 GHz	Im(ε)* at 30 GHz
Pigs	46.28 ± 1.66	15.8 ± 0.57	19.5 ± 0.7	19.26 ± 0.74
Sheep	44.32 ± 0.95	14.58 ± 0.72	19.66 ± 0.72	18.86 ± 0.5
Beef	43.11 ± 1.4	14.02 ± 0.6	19.08 ± 0.53	18.64 ± 0.52
Human	49.00 ± 1.79	16.2 ± 0.61	21.29 ± 0.48	21.52 ± 0.91

*Mean ± standard deviation

TABLE 1.4. STANDARD DEVIATION FOR KIDNEY CORTEX SAMPLES AT 5 AND 30 GHZ.

Specie	Re(ε)* at 5 GHz	Im(ε)* at 5 GHz	Re(ε)* at 30 GHz	Im(ε)* at 30 GHz
Pigs	53.04 ± 2.19	17.27 ± 0.9	20.87 ± 1.3	23.19 ± 1.18
Sheep	50.25 ± 1.22	16.05 ± 0.61	21.47 ± 0.68	22.17 ± 0.51
Beef	46.48 ± 3.05	14.7 ± 1.2	20.33 ± 1.05	20.75 ± 1.43
Human	54.80 ± 2.18	18.03 ± 0.95	22.16 ± 0.6	24.22 ± 0.91

*Mean ± standard deviation

Analyzed heterogeneous tissues

Lungs from pigs, sheep, and human cadaver were chosen as representative for the category of heterogeneous tissues, and 93 samples were considered in the analysis. In Table 1.5, the corresponding database is summarized, together with the Water Content range and the average Water Content.
In addition, the distribution of the samples with the percentage water content is shown in Figure 1.32.

TABLE 1.5. SUMMARY OF THE ANALYZED HETEROGENEOUS TISSUES.

Specie	Organ	#Samples	#Organs	#Animals	Range of WC (%)	Average WC (%)
Pigs	Lung	48	8	4	[73-95]	83
Sheep	Lung	30	6	3	[66-80]	78
Human	Lung	15	2	1	[79-86]	84

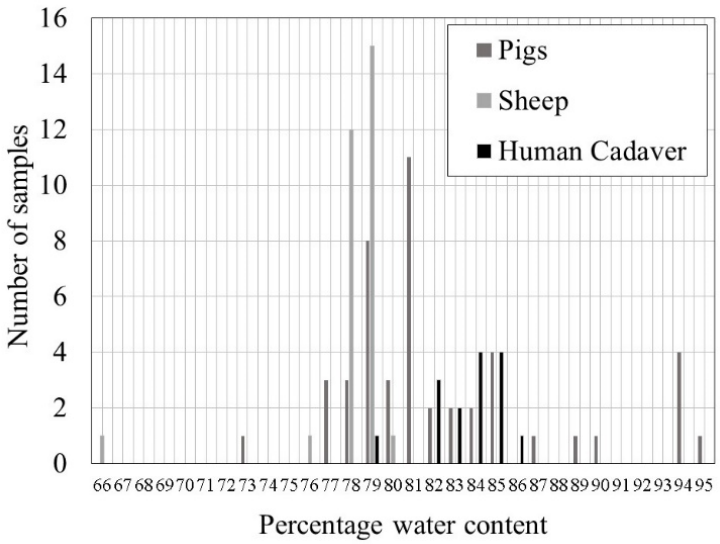

Figure 1.32. Distribution of the samples with the percentage water content for lung samples.

Results for heterogeneous tissues

The average dielectric properties for the lungs of the two animals were compared to the ones of samples derived from human being both for real and imaginary part, in Figure 1.33 a) and b), respectively. In these plots, also the standard deviation is shown, because of its very high value.

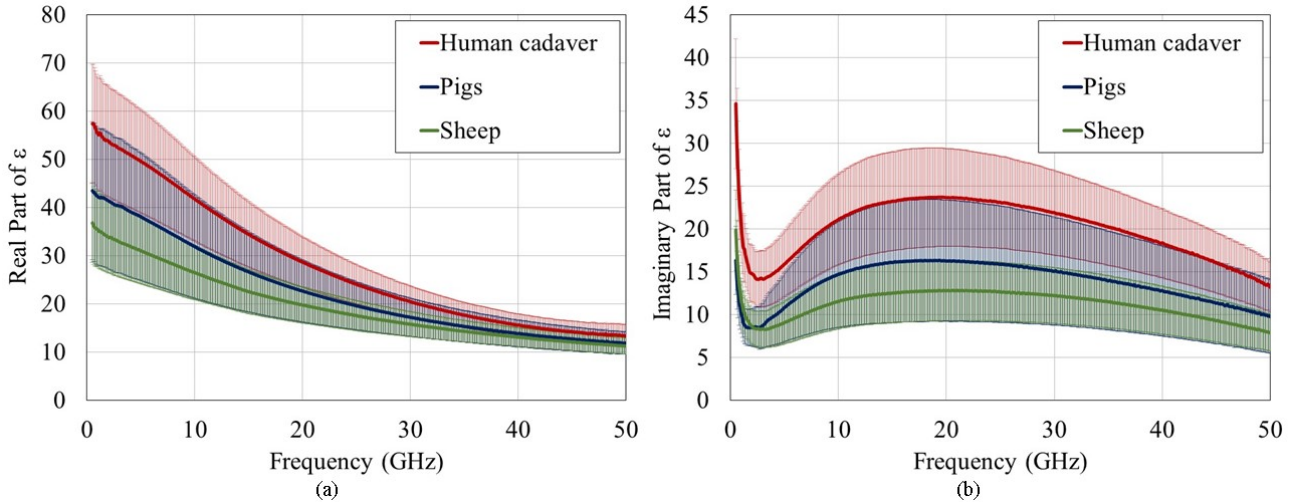

Figure 1.33. Comparison between dielectric properties of samples derived from lungs of human cadaver, pigs and sheep for (a) real and (b) imaginary part. The shaded regions are representative of ± σ.

These graphs show that the standard deviation between measurements both for human cadaver and for animals is large, and this cannot be related only to the large range of water content (Table 1.5), because also the variability among the three measurements on the same sample is large. The trend of the percentage variation coefficient of each sample as function of its water content is shown, as an example, at 10 GHz, in Figure 1.34 a) and b) for real and imaginary part, respectively.

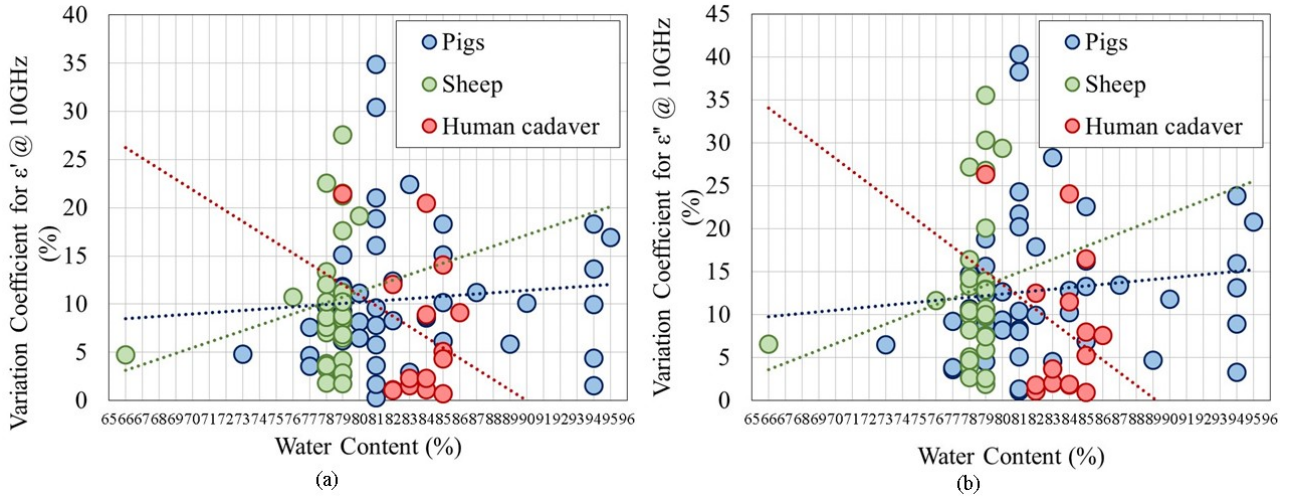

Figure 1.34. Correlation between the percentage variation coefficient and the lung samples hydration level for pigs, sheep and for the human cadaver at 10 GHz for a) real and b) imaginary part.

Due to this variability in measurements, the conclusion that can be derived for this class of tissues is that the hydration level cannot be used as a classifier for dielectric measurement data for this class of tissues both for *inter*- and *intra*-organ variability, and some other classifier (e.g., sample density) has to be found.

Conclusion of this section

In this section, an *ad-hoc* measurement protocol for the dielectric characterization of animal and human derived tissues is proposed, as the absence of a standard protocol could be one of the main causes of the disagreement between the dielectric properties of biological tissues proposed by different research groups referred to the same organ. On top of this, the sample hydration level as possible classifier for the dielectric

measurement data is investigated both for homogeneous and for heterogeneous tissues. In particular, the dielectric properties of 191 samples from two homogeneous organs (liver and kidney cortex) are measured in the frequency range [0.5-50] GHz. Of which, 100 animal liver samples are derived from 5 pigs, 3 sheep and 2 beef, and 9 human liver samples from one human cadaver. On the other hand, 76 animal kidney samples are derived from 4 pigs, 3 sheep and 3 beef, and 6 human kidney samples from one human cadaver. For each sample, three independent measurements are done, producing a whole database of 573 dielectric measurements. For what concerns heterogeneous organs, lungs are chosen as representative of the category and 93 samples both animal and human are measured. Of these, 48 are derived from pigs, 30 from sheep and 15 from one human cadaver.

The exact water content of each sample is determined by means of the *loss-on-drying* method and, among others, the sample hydration level as possible classifier for the *intra-* and *inter-* organs variability and the *intra-* and *inter-* animals variability, as well as the variability between animals and humans, is deeply investigated and quantified. In particular, the correlation between the percentage variation coefficient (ratio between the standard deviation and the average) among the three independent measurements on each sample and its water content is studied, showing the potentiality of the sample water content as a classifier for the *intra-* and *inter-* organ variability for homogeneous tissues, both animal and human derived. In addition, the difference between animal and human derived organs is preliminary investigated, and a not significant dielectric difference is highlighted, in line with the results already published in literature. On the other hand, the same conclusion cannot be derived for the class of heterogeneous organs, because of the very high values for the standard deviations between measurements; therefore, showing the need of finding a different classifier for the dielectric measurement data of this kind of tissues.

In this section, therefore, a new measurement protocol is shown, aimed at preserving the sample hydration level, as well as the possibility of using the sample water content as a classifier for dielectric measurement data for both homogeneous and heterogeneous organs is investigated. The exact water content of the samples is rigorously determined using the *loss-on-drying* approach. For each individual sample, three independent measurements are made and the percentage coefficient of variation between these three measurements was correlated to its exact water content. The results of this analysis for homogeneous organs showed a clear decreasing macro-trend between the variability between dielectric measurements, both for the real and the imaginary part, and the increase in water content of the samples. Thus, opening up the possibility of using this information in future experimental campaigns to derive *a-priori* information about the hydration level of the sample before its rigorous determination (for example, by means of *loss-on-drying* approach, histological analysis and other approaches). In addition, the interesting results reported in this section, as well as this new approach to correlate and gauge the variability between different measurements within a sample to its exact water content, could be hopefully used in the future as a reliable starting point for further analysis involving samples with higher fat percentage, as this category could be more subject to the variability in dielectric measurements.

From all this study related to the correlation of the variability between the different dielectric measurements made on a sample and its water content, it is worth noting that it is essential to adopt a measurement protocol aimed at preserving the hydration level of the sample itself and that is why an attempt to standardize the *ex-vivo* measurement protocol has also been proposed.

On the other hand, it has been demonstrated that for heterogeneous organs the level of hydration is not enough as a classifier for dielectric measurement data, due to the high standard deviation values between the three measurements made on the individual sample. Therefore, to extend this approach to heterogeneous tissues, other classifications (e.g. sample density) should be sought for use in conjunction with the water content of the samples.

Section III - Experimental campaign on mice *in-vivo* tissues

In this last section, the preliminary results of the experimental campaign on *in-vivo* tissues derived from four mice up to 50 GHz are presented. This measurement session is preparatory for the complete experimental campaign, that will be done in the future, at the IFOM (FIRC Institute of Molecular Oncology) institute in Milan. After the extensive experimental campaign on human breast *ex-vivo* tissues and the study of the correlation between dielectric properties of animal and human derived organs, a fundamental additional step is the dielectric characterization of *in-vivo* tissues. Validating the measured dielectric properties on *ex-vivo* tissues in an *in-vivo* environment, where both the body temperature and the blood perfusion are present, is a milestone for the design of both diagnostic and therapeutic microwave systems (usually used on alive patients).
The body of literature about the comparison between dielectric properties of *ex-vivo* and *in-vivo* tissues is not very extensive and there is not a good agreement in the results published by different research groups; for this reason, this work inserts in the framework of the open research about this point.
As an example, two opposite results were achieved by Hater *et al.* (2009) and by Farrugia *et al.* (2016).
In particular, Halter *et al.* in "The correlation of in vivo and ex vivo tissue dielectric properties to validate electromagnetic breast imaging: initial clinical experience", by doing both *in-vivo* measurements during partial or fully mastectomy surgery in the operating theatre on six women and *ex-vivo* measurements in the same locations after the resection of the sample in the Pathology Laboratory in the frequency range 100 Hz-8.5 GHz demonstrated a decreasing in dielectric properties of *ex-vivo* tissues with respect to the dielectric properties of *in-vivo* tissues. On the other hand, in 2016, Farrugia *et al.* in "Accurate in vivo dielectric properties of liver from 500 MHz to 40 GHz and their correlation to ex vivo measurements" by doing measurements up to 40 GHz both *in-vivo* and *ex-vivo* on a colony of mice, demonstrated that under certain conditions of tissue humidity the *in-vivo* and *ex-vivo* dielectric properties do not change significantly.
This preliminary experimental campaign was recently done (July 2019) at the IFOM institute in Milan, in collaboration with the European Institute of Oncology in Milan.

Analysed tissues

In this preliminary work, only the malignant tissues of four mice (three naked and one with fur) were measured, with and/or without the skin. For two naked mice, indeed, the skin removal was not possible for logistic reasons; therefore, all the corresponding results are not directly usable, due to the strong impact of the skin on the dielectric measurement data (even if the thickness of the skin, in this case, does not exceed 0.5 mm and its water content is significantly lower than the one of human skin). In two of the four mice the mouse breast cancer cells were graft, in one mouse the human rectal colon cancer cells were injected and in one mouse the human acute myeloid leukemia cells were implanted. The mice are named *Mouse1*/*2*/*3*/*4* in chronological order.

Measurement setup

The measurement setup, shown in Figure 1.35, was the same used in both the experimental campaigns on human breast *ex-vivo* tissues (Figure 1.1), described in section I.

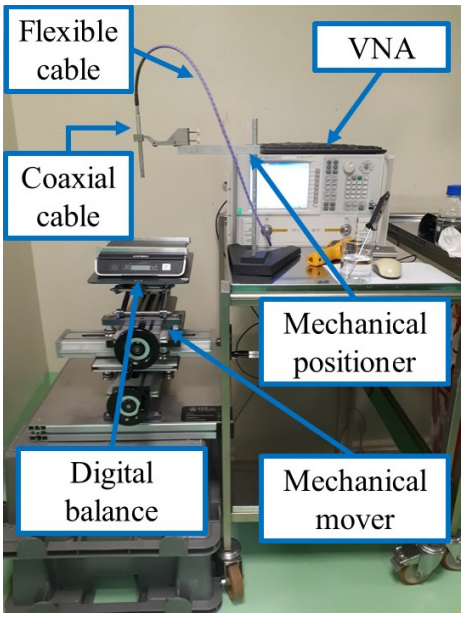

Figure 1.35. Experimental setup.

Measurement protocol

The *in-vivo* measurements were done on alive and anesthetized mice. After the injection of the drug, the mouse was left 10 minutes into the cage to allow the complete absorption of the drug.
The mouse was, then, fixed to a polystyrene plate and placed on the digital balance (above the mechanical mover). Due to the reduced dimensions of the neoplastic mass, three consecutive measurements in the same location on the superficial malignant tissue were done. Both the temperature of the mouse and the room temperature were collected.
Subsequently, the mouse was killed and again fixed in the same location as before. The measurements were repeated *in-loco* (with and/or without the skin) at 2, 4, 6, 8, 10 and 20 minutes from the death of the animal to evaluate the possible impact on dielectric properties of the interruption of the blood flux. For the last mouse, *in-loco* measurements after 20 minutes from the death of the animal were not done for logistic reasons. Each time the mouse temperature was collected, while the room temperature was unchanged (~28° C).
For one of the four mice, after 20 minutes from the death of the animal and after the last *in-loco* measurement, the tumor mass was excised and the *ex-vivo* measurement was done, with and without the skin.
In Figure 1.36, a photo of a mouse with skin during dielectric measurements is shown; while, in Figure 1.37, a photo of a mouse without the skin is represented.

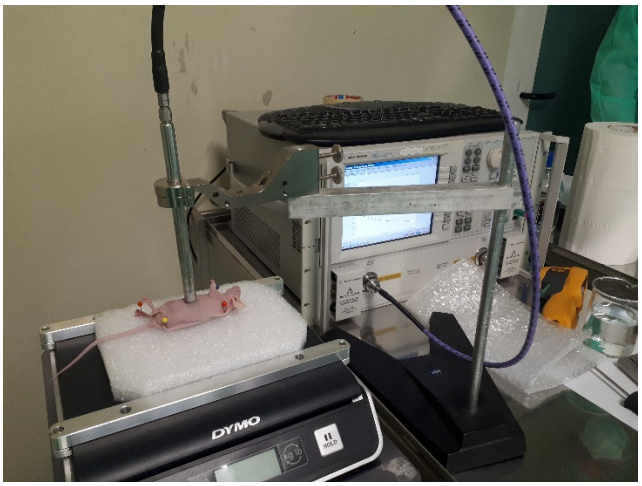

Figure 1.36. Photo of a mouse with skin during dielectric measurement.

Figure 1.37. Photo of a mouse without skin during dielectric measurement.

Results

In Figure 1.38 a)-b) and Figure 1.39 a)-b), the measurements on the two mice for which only measurements with the skin were possible are shown (*Mouse1* and *Mouse4*, respectively), and no difference in dielectric properties *in-vivo* and *in-loco* can be appreciated up to 20 minutes after the death of the animals both for real and imaginary part.

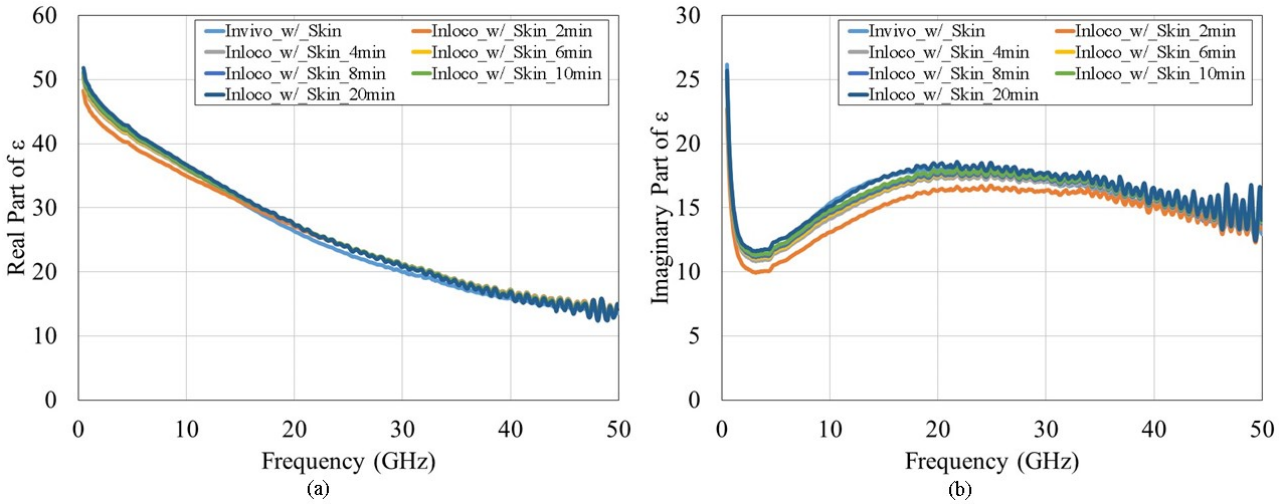

Figure 1.38. Comparison between *in-vivo* and *in-loco* dielectric measurements for *Mouse1* for a) real and b) imaginary part.

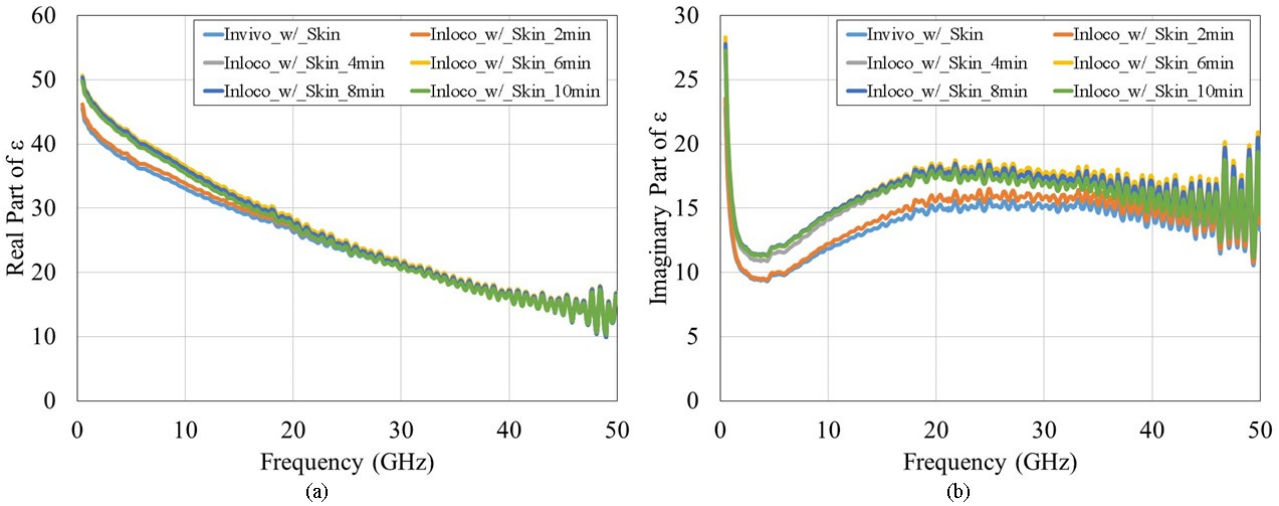

Figure 1.39. Comparison between *in-vivo* and *in-loco* dielectric measurements for *Mouse4* for a) real and b) imaginary part.

In Figure 1.40 a) and b), the measurements done on a naked mouse (*Mouse2*) for which it was possible both to remove the skin and to excise the malignant mass (*ex-vivo*) are shown for real and imaginary part, respectively. These graphs demonstrate the strong impact on the measured dielectric properties of the skin, since the values for the complex permittivity is higher when the neoplastic mass is directly in contact with the probe (as expected).

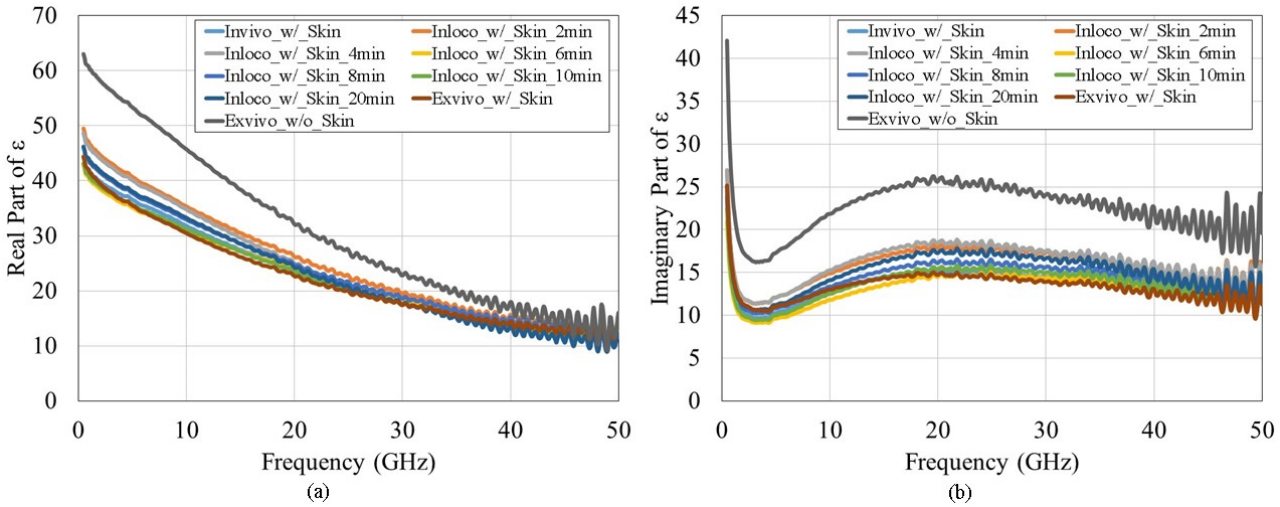

Figure 1.40. Comparison between *in-vivo* and *in-loco* dielectric measurements for *Mouse2* for a) real and b) imaginary part.

The last case is shown in Figure 1.41 a) and b), in which all measurements, both *in-vivo* and *in-loco*, were done without the skin (*Mouse3*).

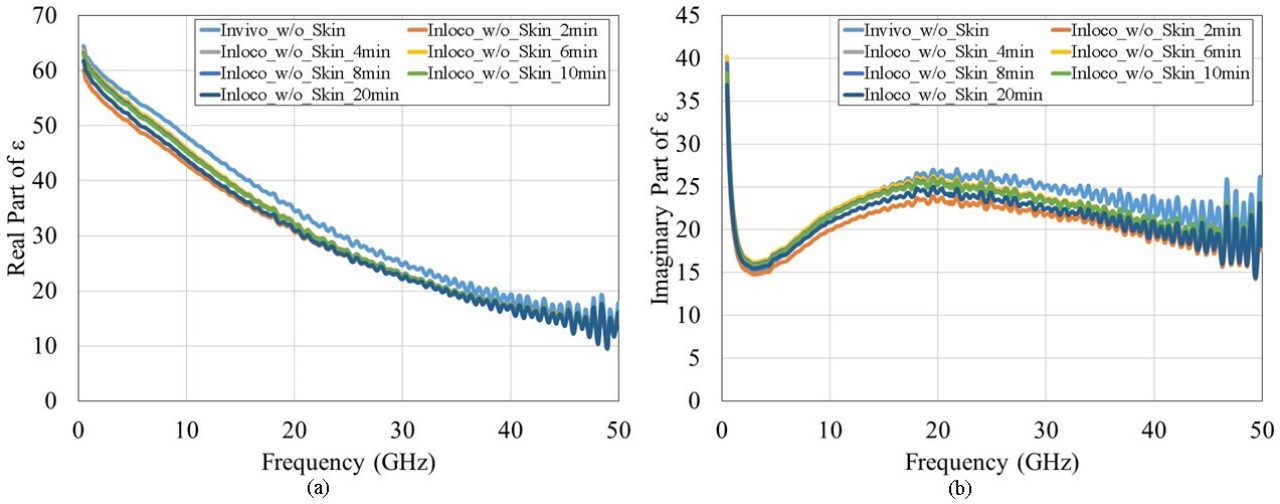

Figure 1.41. Comparison between *in-vivo* and *in-loco* dielectric measurements for *Mouse3* for a) real and b) imaginary part.

From all these graphs, it seems evident that the dielectric properties of *in-vivo* and *in-loco* tissues up to 20 minutes from the death of the mouse do not differ significantly, even if these conclusions need further validations, being derived on measurements done only on four mice.

Conclusions of this section

In this section, a preliminary study of the variability in dielectric properties of *in-vivo* and *ex-vivo* tissues is presented. This measurement session was preparatory for the complete experimental campaign to be performed at a later stage at the IFOM institute in Milan in collaboration with the European Institute of Oncology in Milan. Four mice are included in this preliminary experimental campaign and their dielectric properties are measured in the frequency range [0.5-50] GHz by means of the open-ended coaxial probe (same experimental setup described in section I). The outcomes of the complete analysis will be helpful to validate the experimental data collected on *ex-vivo* tissues. Measurements *in-vivo*, *in-loco* up to 20 minutes from the death of the animal and in one case *ex-vivo* are done, with and/or without the skin. Results show that in all these cases the dielectric data *in-vivo* and *in-loco* does not differ significantly, even if the impact of the skin on the dielectric

measurements is evident from the measurements with and without the skin done on the *Mouse2* and *Mouse3*; however, all the possible conclusions that could be derived from these preliminary measurements require deeper investigation, in particular because the skin must be avoided in all cases. In addition, further analysis including fat tissues (possibly derived by different animals) will be taken into account in the future experimental campaign.

Conclusions

In this chapter, three different experimental campaigns are presented.

In the first section, the results of the two extensive experimental campaigns performed in 2014 and 2016 at the European Institute of Oncology in Milan on human breast *ex-vivo* tissues in the frequency range [0.5-50] GHz are presented. The whole database involved 342 samples (247 healthy and 95 neoplastic ones) derived from around 100 women of ages from 14 to 85 years. The results of this analysis confirm that the significant dielectric difference between healthy and neoplastic tissues is high also in the mm-wave regime, in particular when tissues with high adipose content (≥80%, *Low density* tissues) are considered. In addition, it is demonstrated that this kind of tissue corresponds almost to the 40% of the whole database involving healthy samples and this result could be possibly related to the high concentration of women in the age strip around 50 years old where the use of breast cancer screening, diagnosis, and treatment techniques would be particularly beneficial.

In the second section, the experimental campaign performed at the University of Malta, in collaboration with the *Mater Dei* Hospital in Malta and the Department of Anatomy of the University of Malta, on animal and human derived homogeneous and heterogeneous tissues is presented. In particular, a first attempt to standardize the measurement protocol is proposed and the sample hydration level as possible classifier for the dielectric measurement data is deeply investigated, both for homogeneous and for heterogeneous tissues. The results of this analysis show the potentiality of the sample water content as a classifier for the *inter-* and *intra-*organ variability within the class of homogeneous tissues; while, the same conclusions cannot be derived for heterogeneous organs, where other classifiers (like the sample density) should be found. In addition, also a preliminary comparison between dielectric properties of organs derived from animals and from a human being is done in order to assess and possibly quantify the dielectric difference between the two categories, showing that no statistical difference exists (like in literature).

In the third section, the results of the preparatory experimental campaign on *in-vivo* mice up to 50 GHz are presented. The final aim of this research path is the comparison between dielectric properties of *in-vivo* and *ex-vivo* tissues, to validate the whole experimental campaign on human breast *ex-vivo* tissues, since it was partially demonstrated in the previous section that the dielectric behaviour of animal and human derived tissues does not differ significantly. Measurements *in-vivo* and *in-loco* up to 20 minutes from the death of the animal are done, with and/or without the skin, to evaluate the impact of the interruption of the blood flux on the measured dielectric properties. The results, even if cannot be used as definitive because of the skin presence (in some cases), seem to be promising as no significant variation is appreciable between *in-vivo* and *in-loco* measurements up to 20 minutes. However, in the future experimental campaign, planned for incoming months and involving also fat tissues (probably of porcine origin), the skin will be carefully avoided.

CHAPTER II

TISSUE-MIMICKING BREAST PHANTOMS

Introduction

The realization of realistic tissue-mimicking phantoms is of particular interest to many researchers working in the field of biomedical applications of electromagnetism, since realistic phantoms would give the possibility to validate the performance of all the proposed prototypes in well-controlled and reproducible conditions, as well as to study the algorithms for signal processing and image reconstruction in diagnostic systems. The realization of phantoms is interesting several research groups around the world and the most varied solutions have been proposed, in particular for breast phantoms, either investigating relatively simple oil-in-gelatine mixtures or more complex chemical compositions (possibly for 3-D printing technology). In this Thesis, the interest is for breast phantoms.

A realistic tissue-mimicking phantom has to satisfy several requirements. Firstly, it has to mimic the dielectric properties of real tissues in a target frequency range. Secondly, its electromagnetic properties have to be stable over time to ensure the repeatability of the measurements. Thirdly, its production and its preservation should not require expensive and/or toxic means. In addition, it should ideally reproduce the internal heterogeneity of the human tissues, in particular the breast.

Nowadays, different kinds of tissue-mimicking breast phantoms have been proposed, both using standard molds and basing on the 3-D printing technology. In particular, the most common phantoms rely on oil-in-gelatine, Triton X-100 and polyurethane rubbers mixtures.

In Lazebnik *et al.* (2005), Porter *et al.* (2010), Mashal *et al.* (2011), Alsheheri *et al.* (2011), Bakar *et al.* (2011), Hahn and Noghanian (2012), and Henin *et al.* (2015), o*il-in-gelatine mixtures* for breast phantoms were proposed. In this case, the dielectric properties of the tissues were modified by changing the percentage of oil in the mixture.

In particular, Lazebnik *et al.* (2005), deriving their recipes from Madsen *et al* (1982), proposed oil-in-gelatine mixtures for breast phantoms containing variable percentages of kerosene and safflower seed oil. In these recipes, aqueous gelatine solution and oil solutions (kerosene and safflower seed oil) were mixed at high temperatures, adding a surfactant and formaldehyde. The dielectric properties of all kinds of human breast tissues were mimed by changing the percentages of oil within the mixtures, and the comparison between the two (human tissues and produced phantoms) was done in the frequency range [0.5-20] GHz. The time stability of the dielectric properties of these mixtures over 8 months was demonstrated.

In Porter *et al.* (2010), a recipe for tissue-mimicking breast phantoms based on a combination of chemicals such as gelatine, safflower seed oil, n-propanol, p-toluic acid, formaldehyde and common detergent was proposed. Phantoms mimicking the dielectric properties, up to 6 GHz, of all kinds of human breast tissues (fat,

glands, skin and cancer) were created by changing the percentages of these components in the mixtures and the time stability of their dielectric properties over some months were demonstrated (lesser than 6 months).

Mashal *et al.* (2011), proposed oil-in-gelatine mixtures for the realization of four kinds of heterogeneous breast phantoms. Dielectric properties of fat and fibro-glandular tissues were mimed with mixtures composed by different percentages of water, gelatine, oil (mixture of kerosene and safflower oil) and preservatives. Each phantom was built in multiple stages by using standard molds. The dielectric measurements of these phantoms were done in the frequency range from 1 to 6 GHz and the time stability of the produced mixtures was assessed over 6 weeks, by protecting the phantom from the air exposition. In addition, they validated the stability of the dielectric properties of these phantoms when submerged in oil (mixture of kerosene and safflower oil); therefore, making suitable this kind of phantoms for prototypes involving the immersion of both antennas and phantoms in oil as coupling medium. The exact distribution of the mixtures within the phantom was assessed by means of Computer Tomography scanning. They did not propose the inclusion of cancer-mimicking mixture in this kind of phantom.

In the category of the oil-in-gelatine mixtures, Alsheheri *et al.* (2011), proposed phantoms made by petroleum jelly, soy oil, wheat flour and water to mimic the dielectric properties of all categories of healthy tissues; while, to mimic dielectric properties of tumor tissues they proposed easy mixtures made by water and flour. They measured the dielectric properties of these mixtures in the frequency range [2-12] GHz.

Bakar *et al.* (2011) characterized in the frequency range [3-11] GHz a mixture of propylene glycol, water, gelatine, grape seed oil, commercial dishwashing liquid, formalin, and glyoxal or glutardehyde in order to mimic low-density tissues; on the other hand, to mimic high-density tissues they developed a different composition consisting of agar, vegetable oil, dishwashing liquid and corn-flour.

Hahn and Noghanian (2012) proposed homogeneous mixtures to mimic the dielectric properties of healthy tissues made by distilled water, propylene glycol, gelatine, a surfactant agent and formalin. These components were used to create skin, fibro-glandular, connective and fat tissue, by simply varying the concentrations of the materials. No recipes for malignant tissues were proposed. Dielectric properties of the produced mixtures were measured in the frequency range [1-5] GHz, and heterogeneous phantoms have been created with a stratified model by using proper semi-spherical PVC pipe as molds.

Henin *et al.* (2015) proposed and characterized in the frequency range [1-4] GHz a mixture of gelatine, water, grapeseed oil, propylene glycol and dishwashing liquid for the emulation of breast soft tissues, trying also to characterize the mechanical properties of that phantoms.

Different kinds of recipes were proposed in Romeo *et al.* (2011), Joachimowicz *et al.* (2014), Burfeindt *et al.* (2012), Joachimowicz *et al.* (2016). In this case, mixtures based on *Triton X-100* (a non-ionic surfactant) were used and the dielectric properties of the produced phantoms were varied by changing the proportions of the row materials. This kind of phantom is more stable in both time and temperature with respect to the oil-in-gelatine mixtures at the cost of more expensive components.

Romeo *et al.* (2011) proposed mixtures composed by Triton X-100 and distilled water. The dielectric properties of different kinds of human tissues (following the classification proposed by Lazebnik *et al* (2007)) were mimed by varying the percentages of the two components within the mixture, and mixtures with 20, 25, 30, 35 and 40% of distilled water were produced. The produced phantoms were characterized in the frequency range [0.5-12] GHz and in a wide temperature range from 18 to 30°C.

In Joachimowicz *et al.* (2014) and Joachimowicz *et al.* (2016), mixtures made by distilled water and Triton X-100 were proposed and characterized up to 6 GHz; however, this time the dielectric properties of the produced

phantoms were measured in the temperature range from 25 to 37°C, showing the potentiality of using these phantoms for the test of the prototypes at body temperature. In addition, the time stability over one year of this kind of mixtures was demonstrated; therefore, showing that these phantoms are easy to manage and stable over time. Mixtures with percentage of Triton X-100 of 20, 30, 40 and 100% to mimic dielectric properties of T, G1, G2 and G3 (as in Romeo *et al.* (2011)) have been proposed, adding the salt for mixtures at 40%. This kind of phantom, since in liquid state, is particularly suitable for filling of proper 3-D printed plastic shells for more accurate and heterogeneous phantoms (e.g., Burfeindt *et al.* (2012)), in which the realistic model of the breast is derived from MRI scans. In this case, the air bubble presence is limited and the liquid nature of the produced mixtures simplify the liquid replacement.

In Burfeindt *et al.* (2012), an MRI-derived 3-D-printed breast phantom was proposed. In this phantom, the adipose tissue was mimed by the 3-D-printed ABS plastic parts, while the locations corresponding to the fibro-glandular tissue were left empty to allow the injection of the proper liquid. The mixture used to mimic the dielectric properties of fibro-glandular tissues was a solution of Triton X-100 surfactant and deionized water. The dielectric properties of all the materials involved were measured in the frequency range [0.5-3.5] GHz.

Another class of phantoms is based on the use of *polyurethane*, where the dielectric properties of the produced mixtures are controlled by varying the percentages of graphite powder and carbon black within the rubber mixture (Garrett *et al.* (2015), Oliveira *et al.* (2018)). This kind of materials allows the development of modular phantoms with the inner in solid state and with a free crack for the target inclusion. The usability of the polyurethane to mimic the dielectric properties of breast tissues in the frequency range [1-10] GHz was demonstrated also by Santorelli *et al.* (2015) and Moll *et al.* (2017).

In Garrett *et al.* (2015), the authors proposed a recipe for tissue-mimicking breast phantoms based on carbon/rubber mixtures. By changing the percentage of carbon in the mixture, they mimed the dielectric properties of the skin layer, the fat, the glandular structures and the tumors. These materials were chosen for the realization of breast phantoms because they showed dielectric properties similar to the ones of human breast tissues, their good stability over time, and good mechanical properties, making flexible the produced phantoms. These mixtures were put into a 3-D printer and then assembled into a single breast phantom. In addition, they tested the quality of these phantoms by comparing the results of an imaging test done on a real woman with the results of the test on the phantom. They proposed recipes based on carbon black, graphite and rubber, and they measured the dielectric properties of these mixtures in the frequency range [1-10] GHz. For the phantom fabrication, all the shells were printed by using a 3-D printer (but not with models derived by the breast MRI) and the mixtures mimicking the dielectric properties of different kinds of tissues were poured slowly within them. The dielectric properties of all tissues were changed by varying the concentrations of carbon in the mixture, except for the mixtures mimicking the dielectric properties of fat tissues. In this case, indeed, in order to allow the reconfiguration of the phantom, canola oil and glycerin were used. Also in this case, the problem of air bubbles was highlighted, and it was solved by fulfilling them with other carbon/rubber mixture.

In Oliveira *et al.* (2018), recipes based on polyurethane rubber with graphite and carbon-black powder have been proposed to fabricate a new set of tumor phantoms with different dimensions and spiculations. In particular, spherical phantoms were produced to mimic benign tumors and phantoms with increasing spiculations were used to mimic malignant tumors, since it was demonstrated in Oliveira *et al.* (2015) and Oliveira *et al.* (2016), that the spiculations of a tumor have a very strong impact on the shape of the backscattered signal. For this reason, they proposed 22 tumor models, including different levels of spiculations (corresponding to different degrees of malignancy) with different dimensions. In particular, the dielectric properties of the produced mixtures were modified by changing the concentration of powder mass. Higher

values for the dielectric properties were achieved by significantly increasing the amount of powder within the mixture. However, in this kind of phantoms, the higher is the powder the harder becomes the mixture, compromising the mixing capability itself. Therefore, to solve this problem a slightly different recipe including acetone was proposed for the mimicking of high dielectric properties. The dielectric properties of the produced phantoms were measured in the frequency range [1-8.5] GHz by means of the open-ended coaxial probe at room temperature, and the dielectric properties of the mixtures were compared to the ones of the human breast tissues proposed by Lazebnik *et al* (2007a) and Lazebnik *et al* (2007b). The produced phantoms mimic the dielectric properties of skin, fat, glandular tissue and tumor. For the phantom assembly, different molds were 3-D printed using the PLA (PolyLactic Acid) filament. Then, different shells were filled with the proper mixture. Glandular tissues were modeled as conical structures radiating from the nipple. The mixture mimicking the dielectric properties of human fat tissue was used to fill all the spaces between the glandular structures and the skin layer, therefore making the glue between them. During this process, a cylindrical hole was left empty to allow the introduction of a cylinder including the tumor (surrounded by fat-like mixture).

The preservation of phantoms is also a fundamental aspect to ensure the reproducibility of measurements over time. Strategies involving formaldehyde or formalin solutions have been largely proposed in the literature for oil-in-gel mixtures, and the dielectric properties of the preserved phantoms were measured up to 20 GHz (Lazebnik *et al.* (2005), Madsen *et al.* (2006)) after 8 weeks from the mixture preparation. Another strategy for mixture preservation for gelatine-based phantoms was the use of vinegar, and in this case the dielectric measurements were done in the range [1-6] GHz (Said and Seman (2017)).

However, despite the large variety of proposed recipes, almost all the proposed solutions show some limitations and for this reason the problem of realistic breast phantoms is still of particular interest for the research community. In particular, some of the proposed tissue-mimicking phantoms rely on the use of toxic components both for the production (kerosene derived materials) and for the preservation (formalin solutions) of the phantom, requiring specific laboratory equipment to be handled; in some cases, the fabrication process requires the utilization of not necessarily cheap fabrication processes and complex chemical compositions (for example, for 3-D printed phantoms) and/or very expensive materials (e.g., Triton X-100); in addition, all the proposed tissue-mimicking mixtures have been dielectrically characterized in the microwave regime, not exceeding 20 GHz.

For all these reasons, in this Chapter, the design of low-cost, easy to manage, non-toxic and stable-over-time mixtures for tissue-mimicking breast phantoms, is presented (Di Meo *et al.* (2018c), Di Meo *et al.* (2019a), Di Meo S *et al.* (2019b), Di Meo *et al.* (2018d)). In particular, two class of recipes are proposed: one gelatine-based to mimic the average dielectric properties of all kinds of human breast tissues (healthy and malignant), and one based on the use of waste-oil hardener to mimic the dielectric properties of very low density human breast *ex-vivo* tissues.

For what concerns the gelatine-based phantoms, starting from the basic ingredients of Ultrasound phantom recipes (Madsen *et al.* (1982), (2005), (2006)), new cheap and easy-to-manage phantoms are considered and are dielectrically characterized, in the frequency range [0.5-50] GHz. The proposed recipes make use of deionized water, sunflower oil, gelatine and common dishwashing liquid, and the dielectric properties of all kinds of human breast tissues, both the three categories of normal and the malignant ones, are mimed by changing the percentage of oil volume within the mixture. In addition, the potentiality of the common sunflower oil as a good preservation medium is demonstrated. Therefore, a general methodology to produce and preserve phantoms for the test of imaging prototypes is proposed.

For what concerns the phantoms based on the use of waste-oil hardener, different and easier recipes are proposed involving also a different surfactant (lechitin or Polysorbate 80) instead of the dishwashing liquid in order to mimic the dielectric properties of very fat breast tissues.

The dielectric properties of all the produced phantoms are compared to the ones of the human breast *ex-vivo* samples presented in Chapter I (Martellosio *et al.* (2015, 2017) and Di Meo *et al.* (2017b, 2018a)), while no comparison has been made with the phantoms produced by the other research groups, as there are substantial differences between them (e.g., different recipes, different frequency ranges). The high powerful of the produced tissue-mimicking mixtures is the possibility of tuning their electromagnetic behaviour by adjusting the concentration of the mixture components to accurately mimic healthy and cancerous tissues, composed by different adipose content.
At the end of this chapter, a preliminary hemispherical heterogeneous phantom made by healthy tissue with a tumor-like inclusion is shown.

Experimental setup

The experimental setup includes both instrumentation for mixture preparation (figure 2.1(a)) and for dielectric characterization (figure 2.1(b)). It is composed by:
• two magnetic hot-plate stirrers (BICASA, IKA-COMBIMAG RCT);
• several glass beakers, graduated cylinders and an electronic pipettor;
• an open-ended coaxial probe (Keysight 85070E Dielectric Probe Kit), able to perform measurements in 0.5-50 GHz range;
• a Vector Network Analyzer (VNA, Keysight E8361C), used to drive the coaxial probe, as well as to retrieve, monitor, and store the dielectric permittivity of the Material Under Test (MUT);
• a high performance flexible coaxial cable (provided with the Keysight 85070E Dielectric Probe Kit), to connect the VNA to the coaxial probe;
• a mechanical positioner to keep the probe fixed during measurements;
• a mechanical mover to put the MUT in contact with the probe, which is kept fixed;
• a digital balance to control the small pressure applied on the MUT while placing the probe over it, which was necessary to avoid any air presence between the tip of the probe and the sample;
• a personal computer to store the data acquired by the VNA and to process them using Matlab (The MathWorks) or Microsoft Excel.
The measurement setup, preliminary discussed in Chapter I for the part related to the dielectric characterization, is the same as in the aforementioned experimental campaigns described in Martellosio *et al.* (2015, 2017) and Di Meo *et al.* (2017b, 2018a).

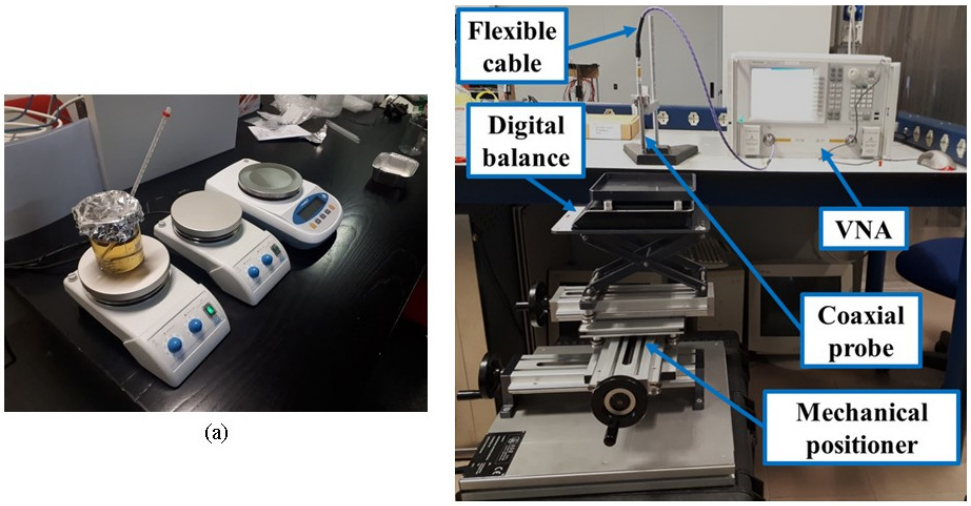

(a) (b)

Figure 2.1. (a) Magnetic hot-plate stirrer during mixture preparation and (b) experimental measurement setup for dielectric characterization.

Mixtures preparation

Two classes of phantoms were prepared: one mimicking the average values both of the three classes of healthy breast tissues (classified in Chapter I) and of malignant ones, and one mimicking the dielectric properties of particularly fat tissues, very difficult to achieve with the first class of recipes. This particular kind of tissues is representative of the 40% of samples measured during the experimental campaigns presented in Martellosio *et al.* (2015, 2017) and Di Meo *et al.* (2017b, 2018a) (as demonstrated in Di Meo *et al.* (2018b) and reported in Chapter I); therefore, represents an interesting clinical case. However, since it requires a high oil percentage and since gelatine dissolves in water, when the water volume percentage decreases (in the case of very fat tissues) the possibility to mix these components is potentially jeopardized; in addition, in such conditions also the dishwashing liquid exhibits problems in terms of uniformity of the emulsion (e.g., too many air bubbles are generated). For these reasons, two different components were used, that are a waste-oil hardener (Kokubo & Co. Ltd.) instead of gelatine and lechitin or Polysorbate 80 instead of dishwashing liquid.
The Kokubo & Co. Ltd. is a stearic acid (belonging to the family of saturated fatty acids) used as an excipient in many pharmaceutical preparations (so, also in this case, non-toxic and cheap). The waste-oil hardener dissolves in oil, and thus the addition of water was functional only to increase the dielectric properties of the produced mixtures. On the other hand, to solve the problem of deleterious air bubbles related to the use of dishwashing liquid (particularly evident when mixtures composed by a high percentage of sunflower oil are considered), two alternatives were used, i.e. lecithin and Polysorbate 80. Also these two materials are cheap, non-toxic, and easy-to-manage, as lecithin is a fatty substance present in animal and plant tissues, and Polysorbate 80 is an emulsifier used in some pharmaceutical and food preparations.
The reagents were measured using high-precision scale, graduated cylinders, or electronic pipettor.
Phantom materials were prepared according to the protocol described below.

For gelatine-based phantoms, gelatine (#G9382, Sigma Aldrich) was dissolved in deionized water (Millipore) by slowly heating the mixture up to 85 °C and continuously stirring the solution on a magnetic hot-plate stirrer. The glass beaker containing the solution was tightly covered with an aluminum foil to prevent water evaporation. Heating was switched off when the solution was clear and then temperature was allowed to decrease to about 65 °C. Sunflower oil (Esselunga, typical Italian Supermarket chain) was heated to about 65 °C and it was added to the water-gelatine mixture with dishwashing liquid (Dexal) to form an emulsion, appearing as a uniform, dense, pale liquid. Stirring continued until temperature fell below 50 °C, then the mixture was allowed to polymerize for about 3.5 h at room temperature (~25 °C).

The procedure based on a waste-oil hardener (Kokubo & Co. Ltd, Japan) and deionized water to produce low permittivity and relatively low loss phantoms emulating fat tissues is a bit different and can be summarized as follows.

The composition of the fabricated gelatine-based mixtures is reported in Table 2.1, together with the ingredients used to produce a 5% volume concentration (v/v) water-in-oil phantom. For the latter class of phantoms, further details will be done in the following of the chapter.

Sunflower oil and deionized water were added into a beaker and rapidly stirred at room temperature until an emulsion was formed. Then, the surfactant (Polysorbate 80 or lecithin) was added while the emulsion was still being stirred. Once the surfactant was well diluted in the mixture, the waste-oil hardener was added. The beaker was then heated and continuously stirred (to ensure homogeneity) on a hot plate using an aluminium foil cap. When the temperature reached approximately 75 °C, the waste-oil hardener became soluble in oil and its grains, previously floating in the mixture, disappeared. The mixture was removed from the hot plate, while continuously being stirred until its temperature reached 55 °C. It was then poured in the mould, where it solidified at around 40 °C–45 °C.

All solidified phantoms appeared as white-to-yellow materials (Figure 2.2) with colour and consistency dependent on the amount of solidifying agent and oil/water ratio. In all cases, the added volume of dishwashing liquid/different surfactant (reported in Table 2.1) was not considered when calculating the final percentages. The addition of the solidifying agent (gelatine or waste-oil hardener) changed the final volume by less than 5% in the worst case and, for this reason, the final mixture volume and its ingredient concentrations were not further corrected, considering the volume change negligible.

TABLE 2.1. COMPOSITION OF PHANTOM MIXTURES (Di Meo *et al.* (2019a)).

Mixture	Mimicked tissue	Deionized water (ml)	Gelatine (g)	Sunflower oil (ml)	Dishwashing liquid (ml)
G5	-	68	3.4	0	3.8
G10	-	68	6.8	0	3.8
G20	-	68	13.6	0	3.8
G16O20	Malignant	68	13.6	17	3.8
G8O20	Malignant	68	6.8	17	3.8
G6.6O33.3	High-density	68	6.8	34	3.8
G5O50	Medium-density	68	6.8	68	3.8
G3.3O66.6	Low-density	68	6.8	136	3.8
Mixture	Mimicked tissue	Deionized water (ml)	Waste-oil hardener (g)	Sunflower oil (ml)	Polysorbate 80 (ml)
K5.7O95	Low-density	2.6	3	50	4

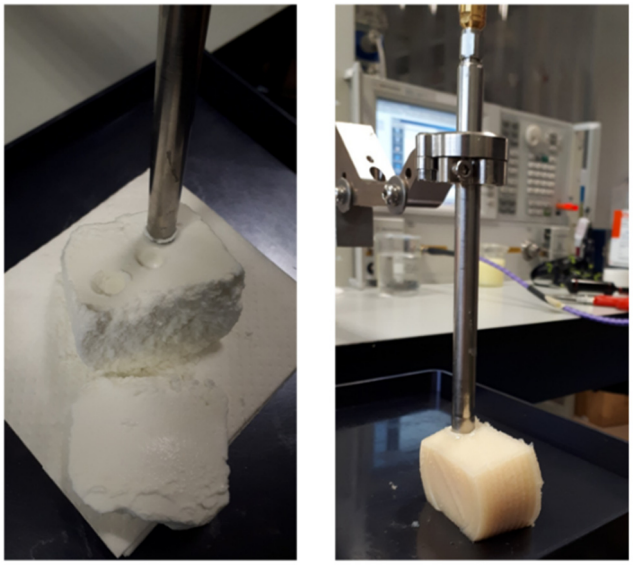

Figure 2.2. Photo of the (a) gelatine-based and (b) waste-oil-hardener-based mixture during dielectric characterization (Di Meo *et al.* (2019a)).

Gelatine-based phantoms

Oil percentage impact on permittivity

Depending on the adipose content, and according to the classification proposed by Martellosio *et al.* (2015, 2017) and Di Meo *et al.* (2017b, 2018a) (explained in the first section of Chapter I), human breast tissues can be divided in four categories: *Low*-/*Medium*-/*High*-density healthy tissues and Malignant tissues, as summarized in Table 2.2, where also the standard deviations of real and imaginary part at 4 and 30 GHz are shown.

TABLE 2.2. CATEGORIES OF HUMAN BREAST TISSUES (Di Meo *et al.* (2019a)).

Tissue category	Adipose content	Re(ε)[a] at 30 GHz	Im(ε)[a] at 30 GHz	Re(ε)[a] at 4 GHz	Im(ε)[a] at 4 GHz
Low density	≥ 80%	6.27 ± 4.46	3.27 ± 5.33	11.70 ± 12.67	2.82 ± 4.01
Medium density	20% - 80%	11.48 ± 5.48	9.57 ± 6.97	27.00 ± 16.53	7.70 ± 5.40
High density	≤ 20%	16.04 ± 5.04	15.54 ± 6.74	40.71 ± 15.39	12.20 ± 5.06
Malignant	-	18.80 ± 2.83	19.28 ± 4.23	48.55 ± 8.88	14.75 ± 2.89

[a] Mean ± standard deviation

In Figure 2.3 the comparison between the dielectric permittivity of the gelatine-based mixtures (G8O20, G6.6O33.3, G5O50, G3.3O66.6), produced according to the protocol explained above, and the average values of dielectric permittivity of the four categories of human breast tissues is shown. To assess the homogeneity of the produced mixture, the solidified phantom mixture was cut in two halves and three measurements at increasing depths (with a step of about 1 cm between them) were acquired with the coaxial probe on the inner side of one of these two parts (Figure 2.4). The curves of the produced mixtures were obtained as the average of these three measurements.

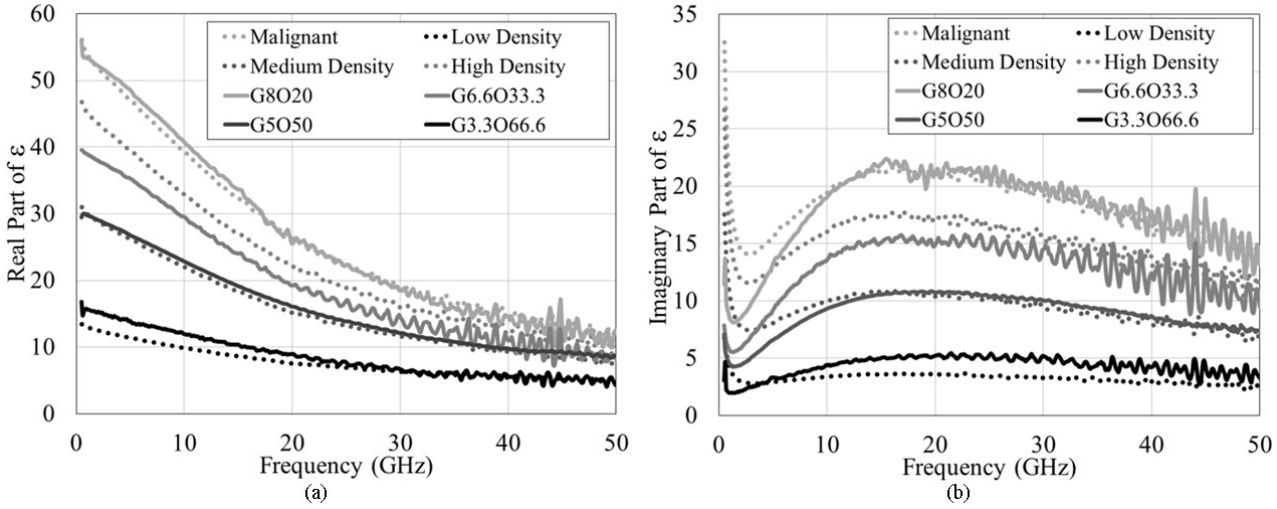

Figure 2.3. Comparison between the average dielectric properties of human breast *ex-vivo* tissues (Di Meo *et al* (2018b)), and of the produced mixtures for (a) real and (b) imaginary part of ε (Di Meo *et al.* (2019a)).

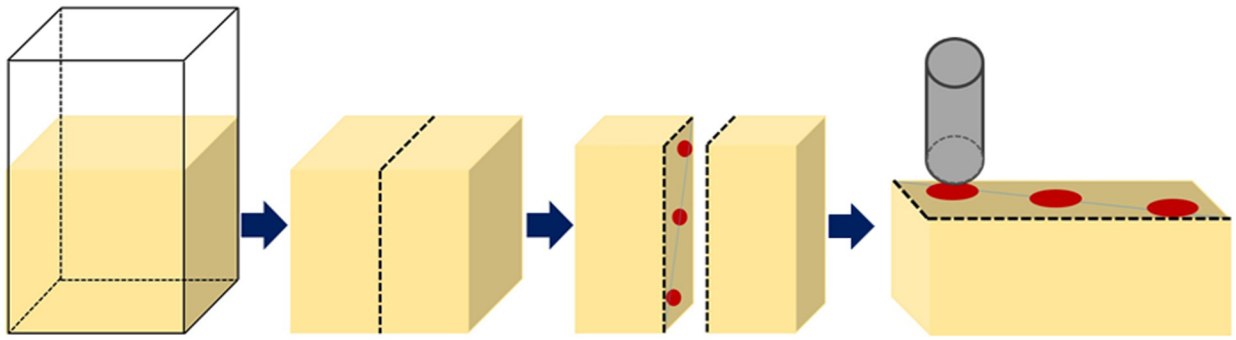

Figure 2.4. Schema of the measurement procedure: the solidified mixture is cut in two halves and three measurement sites (red areas), at increasing depths, are identified on the inner side of one of these two parts; the coaxial probe (grey cylinder) is then put in contact with the sample in each one of these points, and three measurements are acquired and averaged (Di Meo *et al.* (2019a)).

Differences among the three measurements were small in all the considered cases: the percent median absolute deviation (PMAD, i.e. the median of the absolute differences with the median, divided by median value) of the real and imaginary part of ε was lower than 3% and 2%, respectively, thanks to the homogeneity of the produced mixture. Given a mixture composition, the measured average values of ε at 30 GHz were also highly reproducible among independent tests in different days, in which the same mixture was fabricated.
In such case, PMAD was typically lower than 3% and 5% for real and imaginary parts of ε, respectively (upper limits among the ε values at the frequencies of 4 and 30 GHz).

The plots in Figure 2.3 show a very good agreement between measurements on *ex vivo* and gelatine-based phantom samples. In particular, in all the four conditions, the average ε both at 4 GHz and at 30 GHz of the fabricated mixtures falls within the *inter*-subject variability range of human breast tissue measurements (reported in Table 2) (Di Meo *et al.* 2018a). From Figure 2.4, other two aspects could also be observed, at low and at high frequencies. In particular, at low frequency the imaginary part increases, and this effect can be attributed to the non-zero ionic conductivity of the dishwashing liquid (4.86 S m−1, measurement performed using a HI 8733 conductivity meter (Hanna instruments)). Using different surfactant agents, the conductivity can be ideally tuned to the desired value. For example, the conductivity of the produced mixture can be increased by using dishwashing liquid with higher static conductivities or, alternatively, can be minimized by using a different surfactant agent (for example, the Polysorbate 80).

On the other hand, at high frequency, the ripple of the curves increases, both for human breast tissues and for the produced mixtures. This effect, while not impairing the overall trend of the measurement, is due to inaccuracies during the calibration of the coaxial probe, a common effect at such high frequencies (Martellosio *et al.* (2017)). The calibration of the coaxial probe is performed using three standards: deionized water at a controlled temperature (room temperature ~20°C), air, and short-circuit. The measurements in air is straightforward, and the appropriateness of the measurement in water can be controlled accurately using a transparent glass for the water, in such a way that the presence of air bubbles on the probe tip can be avoided. On the other hand, for the short-circuit, a customized metal block provided with the Keysight 85070E Dielectric Probe Kit is used. Especially at high frequencies, it can be difficult to guarantee the robustness of the contact between the probe tip and the metal block, and small imprecisions can hold. For this reason, the ripple is present both on phantom and *ex-vivo* tissue measurement (in this last case, the ripple is not visible on the curves shown in Figure 2.4 thanks to averaging on more than 100 samples).

Bruggeman formula

An estimate of the effective dielectric permittivity of the mixture, given the percentages of oil and water, was derived by means of the ***Bruggeman formula*** (Bruggeman (1935)), and it was used to compare the obtained results with theoretical expectations. The formula is:

$$p\frac{\varepsilon SFO - \varepsilon eff}{\varepsilon SFO + 2\varepsilon eff} + (1-p)\frac{\varepsilon H2O - \varepsilon eff}{\varepsilon H2O + 2\varepsilon eff} = 0$$

where ε_{H2O} is the permittivity of water, ε_{SFO} is the permittivity of sunflower oil (SFO), ε_{eff} is the permittivity of the mixture and p represents the volumetric concentration of sunflower oil in the mixture.
The comparison between the permittivity values of the produced mixtures (with different oil volume percentages) both at 4 GHz and at 30 GHz and those derived by the Bruggeman formula is shown in Figure 2.5 a) and b), and Figure 2.6 a) and b), at 4 and at 30 GHz, for real and imaginary part, respectively. For all the produced mixtures, the variation coefficients both for real and imaginary part of the dielectric permittivity were less than 2%. In all cases, a good agreement between them is shown, both confirming the theoretical expectations and paving the way to the rational design of breast phantoms with target dielectric properties.

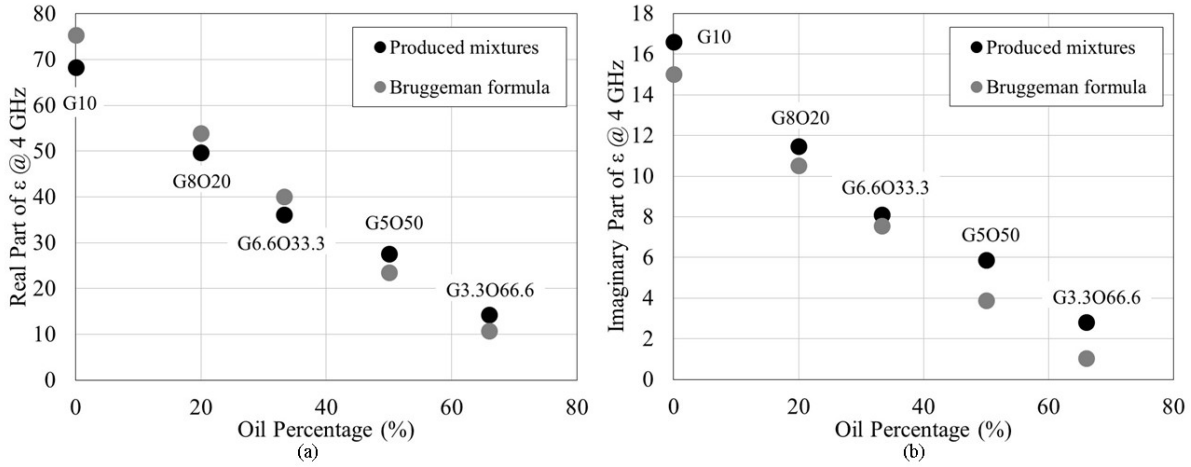

Figure 2.5. Comparison between the values of dielectric permittivity at 4 GHz of the produced mixtures (G10, G8O20, G6.6O33.3, G5O50, G3.3O66.6) and the expected theoretical values obtained with the Bruggeman formula, for (a) real and (b) imaginary part of ε (Di Meo *et al.* (2019a)).

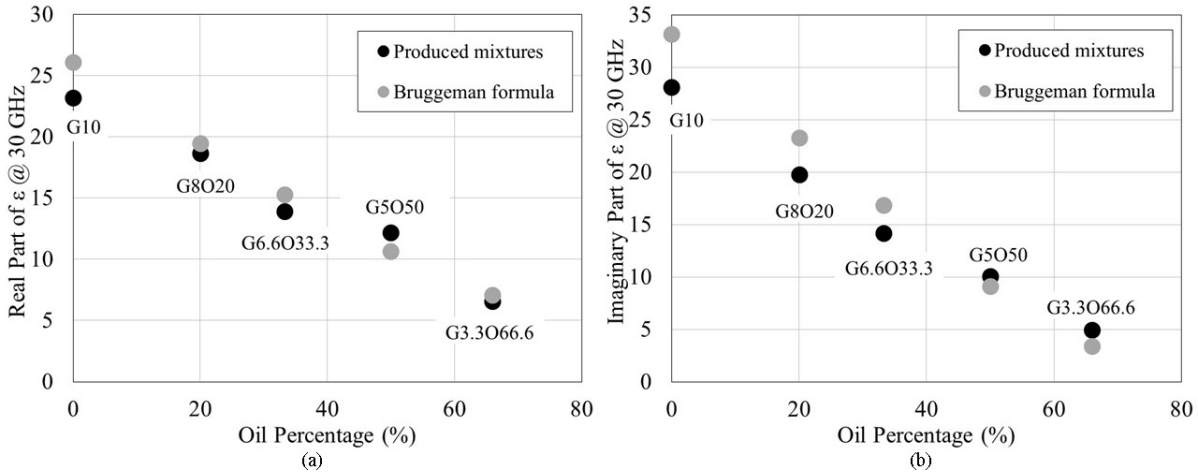

Figure 2.6. Comparison between the values of dielectric permittivity at 30 GHz of the produced mixtures (G10, G8O20, G6.6O33.3, G5O50, G3.3O66.6) and the expected theoretical values obtained with the Bruggeman formula, for (a) real and (b) imaginary part of ε (Di Meo *et al.* (2019a)).

Gelatine percentage impact on the permittivity of tumor-like mixtures

Since the clinical condition of a tissue has a direct impact on its stiffness (usually tumor tissues are stiffer than healthy ones (Sarvazyan *et al* 1995)), in order to create a realistic phantom from a mechanical point of view, it may be necessary to change the amount of solidifying agent. Thus, in this study, the relation between the amount of gelatine and the dielectric properties of the resulting phantom mixtures is firstly analyzed; then, the Young's modulus of the produced mixtures corresponding to malignant tissues is measured.

Mixtures consisting of pure water with different gelatine percentages (see Table 2.1) were firstly prepared, in order to evaluate more clearly the impact of gelatine on ε, and the values of dielectric properties at 4 and 30 GHz are shown in Figure 2.7 a)-b) and Figure 2.8 a)-b), for real and imaginary part, respectively. Figures 2.7 and 2.8 show that in general, by increasing the gelatine percentage, the dielectric properties of the produced mixtures decrease or remain almost constant. The same behavior can be observed also when fabricating phantom mixtures (i.e. with sunflower oil, water, gelatine and dishwashing liquid). The permittivity of pure water with different gelatine percentages is compared to that of two mixtures mimicking malignant tissues (G8O20 and G16O20), which also shows a similar trend of ε when the gelatine concentration doubles, in Figure 2.7 and Figure 2.8, both at 4 and 30 GHz.

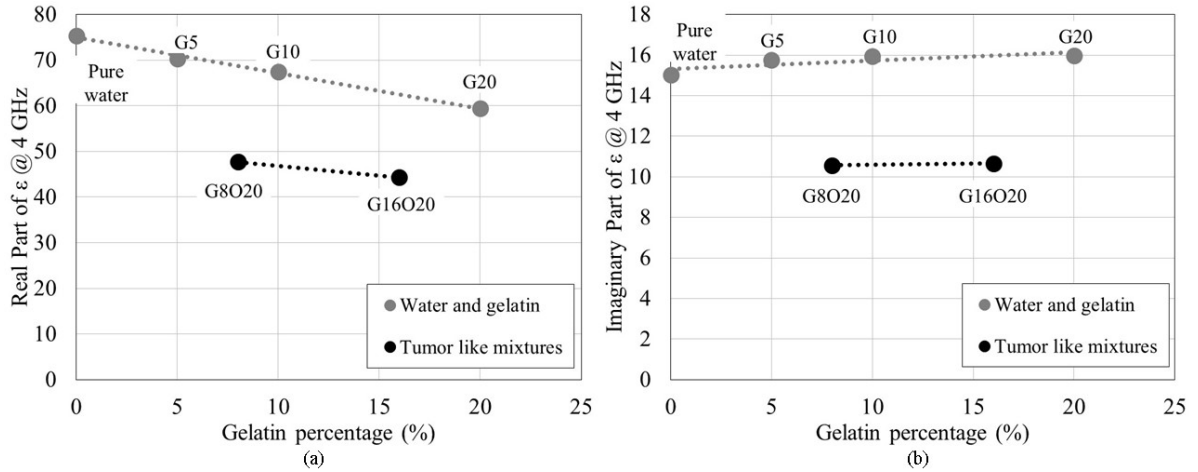

Figure 2.7. Comparison between the electromagnetic properties of pure water with different concentrations of gelatine and of G8O20 and G16O20 at 4 GHz, for (a) real and (b) imaginary part of ε. Dotted lines are representative of the trend lines of the data illustrated with the same color (Di Meo *et al.* (2019a)).

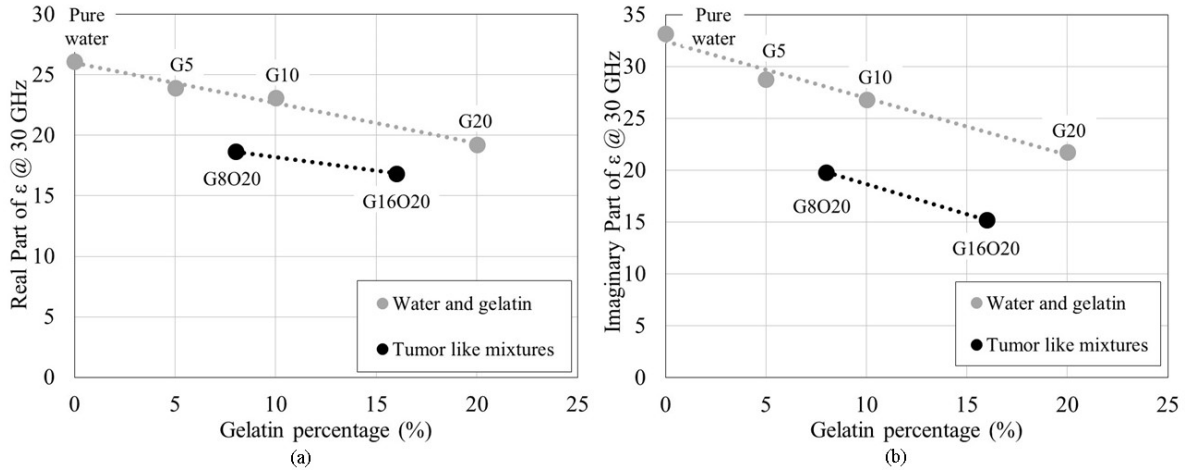

Figure 2.8. Comparison between the electromagnetic properties of pure water with different concentrations of gelatine and of G8O20 and G16O20 at 30 GHz, for (a) real and (b) imaginary part of ε. Dotted lines are representative of the trend lines of the data illustrated with the same color (Di Meo *et al.* (2019a)).

In general, however, variations of ε are relatively low. For instance, Figure 2.9 compares the permittivity of these two mixtures (G8O20 and G16O20) to that of human malignant tissues (mean value ± standard deviation), showing that the dielectric properties of the phantoms are in both cases very similar to the target ones.

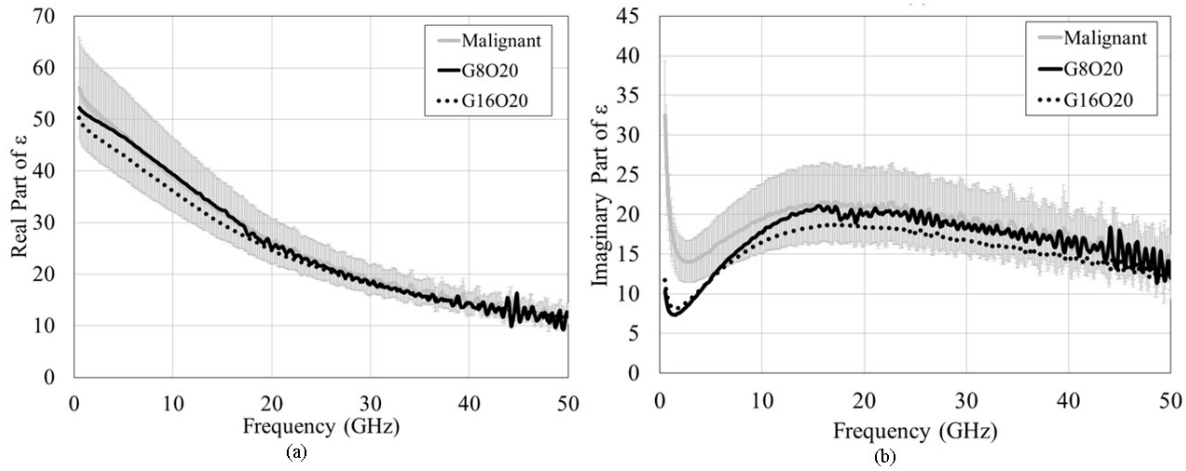

Figure 2.9. Comparison between G8O20, G16O20 and the average values of dielectric permittivity of human malignant tissues (mean ± standard deviation), for (a) real and (b) imaginary part of ε (Di Meo *et al.* (2019a)).

Gelatine percentage impact on the mechanical properties of tumor-like mixtures

Since the previous results demonstrate that the variation in dielectric properties are not significant when higher percentages of gelatine are used in the mixture, other two samples with different volume percentages of gelatine mimicking malignant tissues were prepared and both dielectric and mechanical properties were measured. The possibility to provide at the same time mechanical properties similar to those of real tissues would be, indeed, beneficial to deliver phantoms as realistic as possible. This kind of phantom, realistic from both electromagnetic and mechanical point of view, could be useful also in the perspective of testing a different imaging system, based for example not only on radar but also on the microwave elastography approach (currently done at Ultrasound).

In particular, the two mixtures were composed by 34 ml of deionized water, 8.5 ml of sunflower seed oil, 1.9 ml of dishwashing liquid, and 6.4 g (15% of gelatine volume, Sample #1) or 9.6 g (22.5% of gelatine volume, Sample #2) of gelatine. The procedure for phantom preparation, as well as the experimental setup for the

measurement of the phantom dielectric properties, was the same as above. The comparison between the dielectric properties of the two mixtures and the dielectric properties of human neoplastic tissues is shown in Figure 2.10 a) and b) for real and imaginary part, respectively.

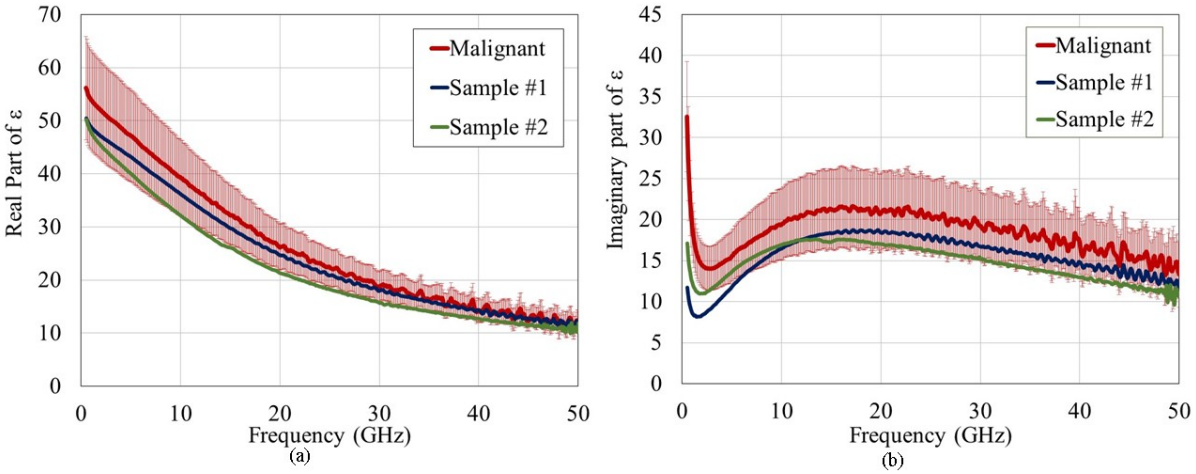

Figure 2.10. Comparison between the (a) real and (b) imaginary part of ε of the produced mixtures and of human breast malignant tissues (mean value ± one standard deviation) (Di Meo *et al.* (2018d)).

These graphs show a good agreement between the dielectric properties of the two mixtures and the ones of the human breast *ex-vivo* malignant tissues; therefore, increasing the gelatine percentage in the mixture, dielectric properties do not vary significantly and in any case remain within the strip of one standard deviation.

After the dielectric characterization of the produced mixtures, they were prepared for mechanical tests. As an example, Figure 2.11 a) shows a picture of three samples obtained from Sample #1, and Figure 2.11 b) is a picture taken during the mechanical test.
This test of the mechanical properties of the produced phantoms was done in collaboration with the Department of Civil Engineering and Architecture of the University of Pavia. All measurements were performed using MTS Insight 10 electromechanical testing machine (MTS Systems Corporation), that was connected and controlled by a computer. The system was set to have a sampling frequency of 10 Hz, a test speed of 2 mm/min, and a pre-load of 0.4 N.

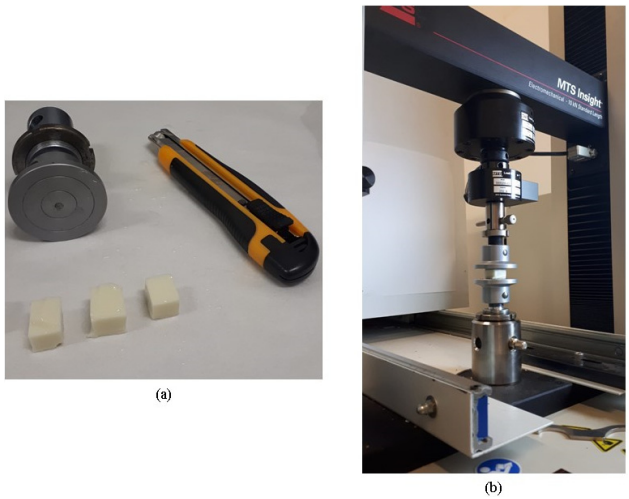

Figure 2.11. Sample #1 (a) before and (b) during mechanical measurements (Di Meo *et al.* (2018d)).

In Figure 2.12, the stress-strain curves for both samples are shown. From these curves it is possible to estimate the Young's modulus of each sample, as it is representative of the material stiffness. As an example, for a 20% strain level, the estimated Young's modulus (i.e., the slope of the strain-stress curve in that region) is about 38 kPa for Sample #1 and 42.3 kPa for Sample #2. These values were found by assuming a linear behavior of the material in this strain range.

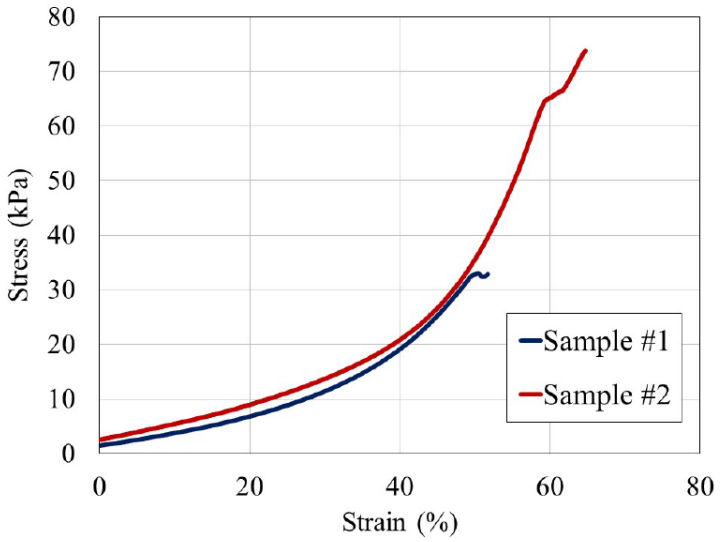

Figure 2.12. Stress-Strain curves for the two produced mixtures (Di Meo *et al.* (2018d)).

The obtained results are in agreement with those presented in Henin *et al* (2015), showing that the gelatine increases the mixture stiffness. This preliminary feasibility study of the phantom stiffness increasing with the gelatine volume, despite requires a much more extensive experimental campaign involving more gelatine percentages, showed that the volume gelatine percentage could be potentially increased to raise the tumor-like phantom stiffness; therefore, paving the road to the possibility of using this type of phantom also for other applications (for example, microwave elastography).

Preservation protocol for the gelatine-based phantom

One of the most important aspects for a durable tissue-mimicking mixture is the stability of its electromagnetic properties, in order to ensure a reliable test of the imaging system prototype over time. In this section, the test of two simple, easy-to-manage and inexpensive materials (i.e. deionized water and sunflower oil) as preservation media for the developed mixtures is presented, along with the comparison between the dielectric properties of the samples preserved in these ways and the ones of the phantom sample left in air.

The outcomes of this study demonstrated the superior capability of oil for preserving a malignant tissue-mimicking phantom (G16O20) over 10 days. Six measurements were taken over 10 days, 96/144/168/192/216/240 hours after the sample preparation (*Reference*), and they are referred to as *Day4/6/7/8/9/10*, respectively. Figure 2.13 shows the three samples of G16O20 immersed in sunflower oil, deionized water and in air. In the same way, in (Di Meo *et al.* 2018c), the effectiveness of oil as preservation solution, for example, for a medium-density tissue-mimicking phantom (G5O50) compared to deionized water and no-medium conditions was demonstrated over 8 days. In this Thesis, due to the similarity of the results, only the preservation of the G16O20 mixture over 10 days is reported.

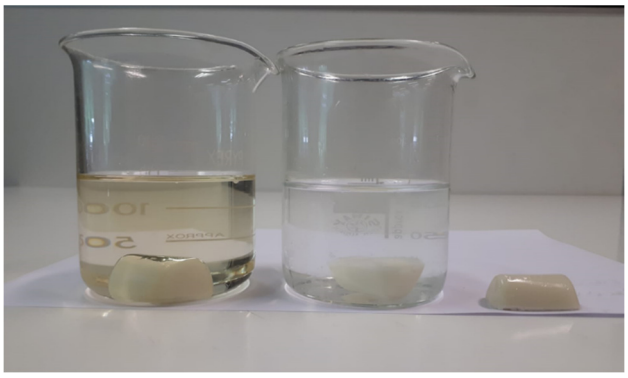

Figure 2.13. Photo of the three samples of G16O20 mixture preserved (from left to right) in sunflower oil, deionized water and air (Di Meo *et al.* (2019a)).

In Figure 2.14 a)-b) and Figure 2.15 a)-b), the comparison between the permittivity values at 4 GHz and at 30 GHz for G16O20 mixture over 10 days preserved in deionized water, sunflower oil and left without preservation medium is shown for a) real and b) imaginary part.

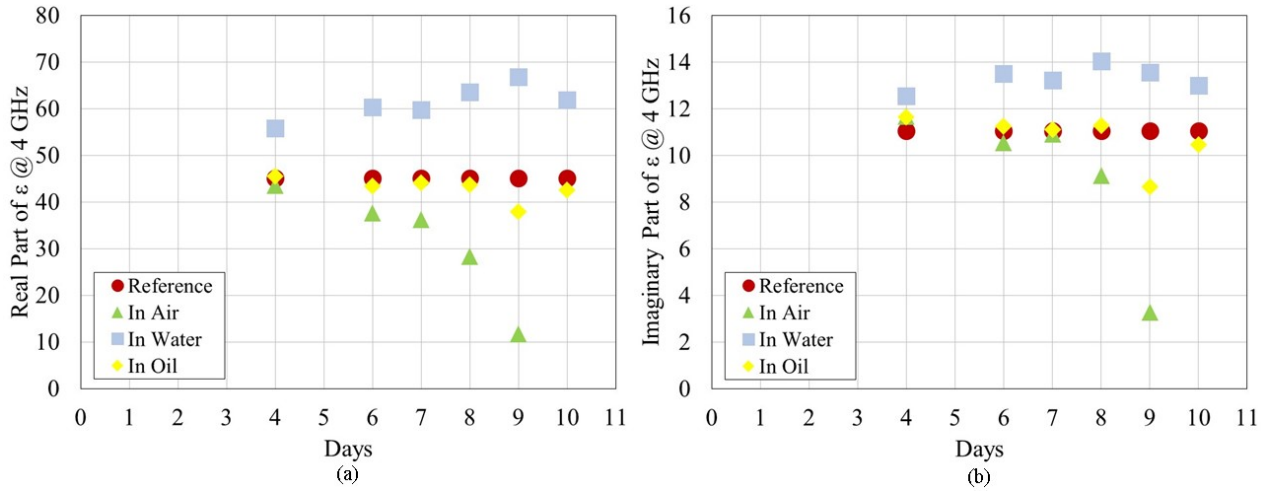

Figure 2.14. Comparison between the dielectric permittivity values for G16O20 preserved in deionized water, sunflower oil and air at 4 GHz, for (a) real and (b) imaginary part of ε (Di Meo *et al.* (2019a)).

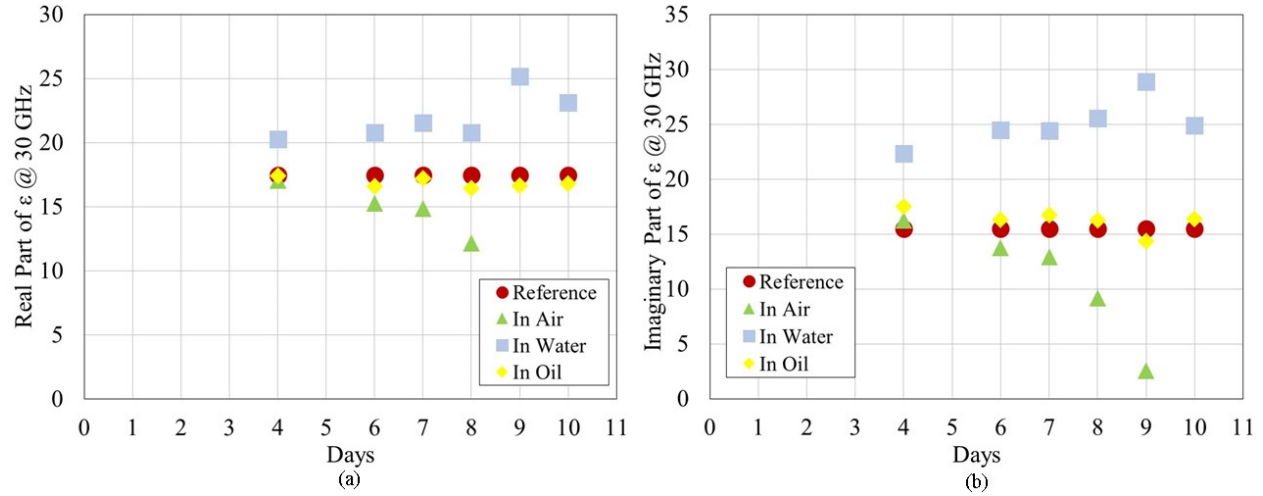

Figure 2.15. Comparison between the dielectric permittivity values for G16O20 preserved in deionized water, sunflower oil and air at 30 GHz, for (a) real and (b) imaginary part of ε (Di Meo *et al.* (2019a)).

These results show that the sunflower oil allows to maintain the dielectric properties of the mixture submerged in it almost unaltered over 10 days, a reasonable time considering the very low costs of the involved materials. When water is used as a preservation medium, instead, it is soaked by the solidified mixture, thus increasing its water content and consequently the permittivity of the mixture. On the contrary, when the phantom is left in air (no preservation medium), the water content reduces with time (water evaporation), resulting into a reduced permittivity. Similar results were obtained in Di Meo *et al* (2018c) for G5O50 preservation, as well as for G3.3O66.6 (data not shown).

For completeness, in Figure 2.16 a)-b), the comparison between the permittivity of G16O20 measured on the day of its preparation (*Reference*) and on the following days, when preserved in sunflower oil, is shown for the entire frequency band, for real and imaginary part, respectively.

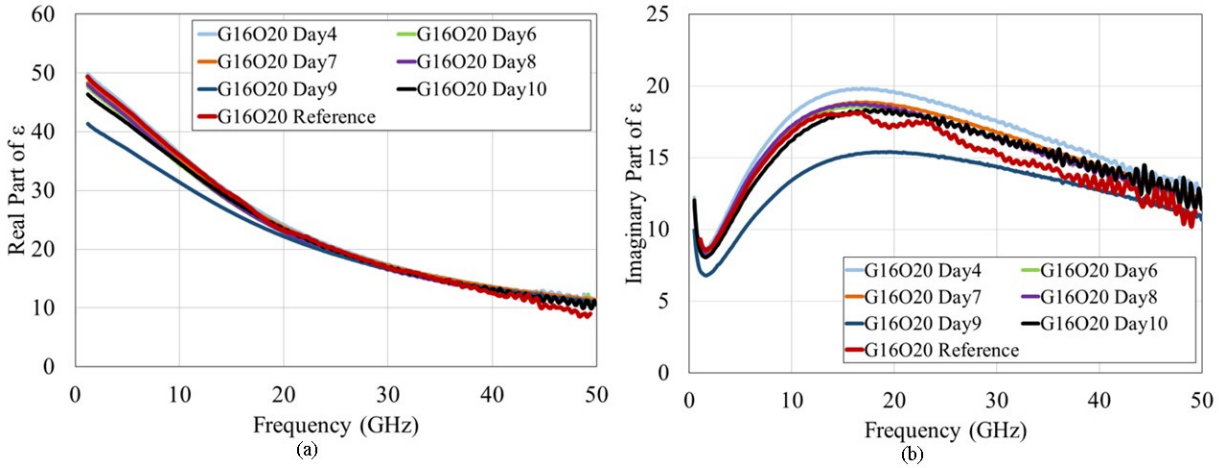

Figure 2.16. Comparison between the dielectric properties of G16O20 preserved in sunflower oil over 10 days, for (a) real and (b) imaginary part of ε (Di Meo *et al.* (2019a)).

Waste-oil hardener based phantoms

Mixtures with waste-oil hardener and sunflower oil

The gelatine-based mixtures presented above relied on deionised water, sunflower seed oil, dishwashing liquid and gelatine. However, these recipes show some limitations when particularly fat tissues are considered. Gelatine, indeed, dissolves in water, so when the water volume percentage decreases (in the case of very fatty tissues) the possibility to mix these components is compromised.
For this reason, new recipes are proposed. A cheap and easy-to-manage waste-oil hardener material (Kokubo & Co. Ltd., Japan) is used together with deionized water and a new surfactant, Polysorbate 80, to mimic the dielectric behavior of highly fatty tissues. These are, indeed, representative of a significant percentage of the human healthy *ex-vivo* samples (Di Meo *et al* (2018b)), and represent also the perfect scenario for reaching an adequate penetration depth with a mm-wave imaging system.

The comparison between the permittivity of human *ex-vivo* tissues with low density (fat content ≥80%) and of the produced K5.7O95 mixture (Table 2.1), obtained as an average between three measurements in different points on the sample is shown in Figure 2.17 a)-b) for real and imaginary part, respectively. This average, thanks to the homogeneity of the produced mixture, is representative of the three measurements done on the phantom.

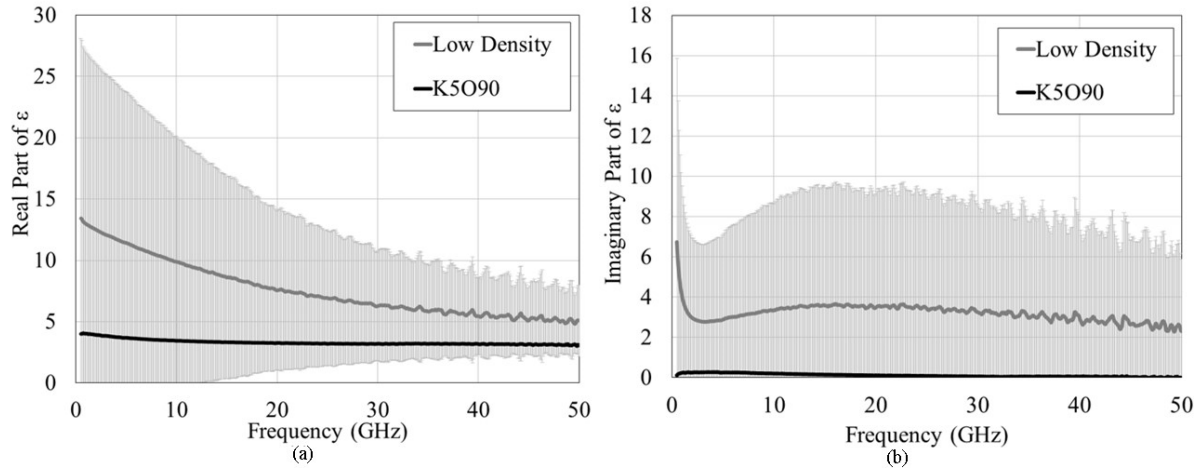

Figure 2.17. Comparison between the average dielectric properties of low-density breast *ex-vivo* tissues (mean ± standard deviation) and of the K5O90 mixture, for (a) real and (b) imaginary part of ε (Di Meo *et al.* (2019a)). The dielectric properties of the produced phantoms are well below the average of this class of healthy tissues, as they represent the outlier of this category.

To assess the possibility of controlling the dielectric properties of this new kind of recipes by adding the percentage of deionized water, mixtures with different percentages of water content were created (Table 2.3). In addition, also mixtures with a different surfactant, lecithin, were proposed.

TABLE 2.3. PHANTOM MIXTURE WITH SUNFLOWER OIL AND WASTE-OIL HARDENER (Di Meo *et al.* (2019b)).

	Ingredients				
Mixture Name	Deionized water (ml)	Waste-oil hardener (g)	Sunflower oil (ml)	Lecithin (g)	Polysorbate 80 (ml)
Mixture1	2.6	2	50	1	-
Mixture2	5.6	2	50	1	-
Mixture3	2.6	2	50	-	2
Mixture4	5.6	2	50	-	2

As for the K5O90 mixture, also the dielectric properties of these phantoms were compared to the ones of the human breast *Low density* tissues, as shown in Figure 2.18 a) and b) for real and imaginary part, respectively.

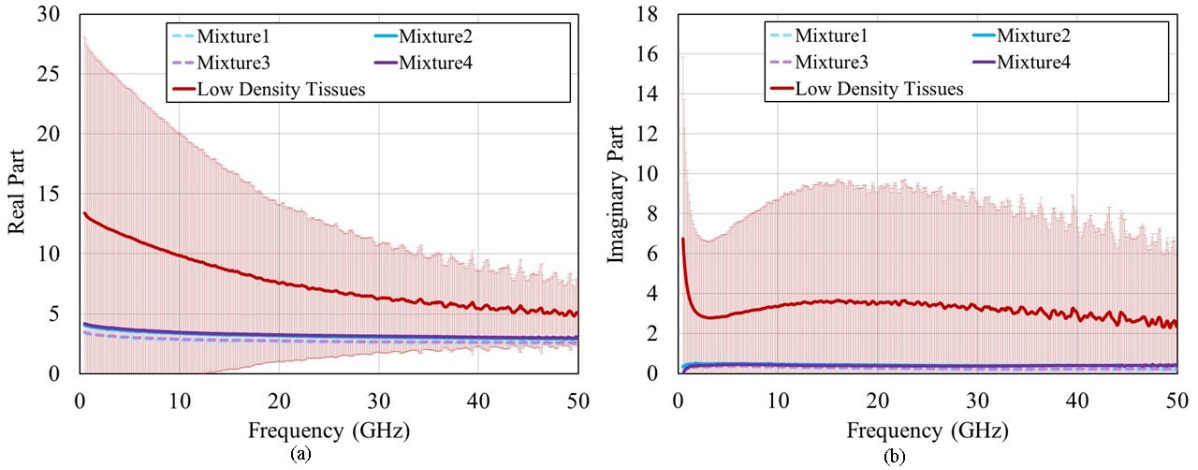

Figure 2.18. Comparison between the average dielectric properties of low-density breast *ex-vivo* tissues (mean ± standard deviation) and the dielectric properties of the produced *Mixture1/2/3/4*, for (a) real and (b) imaginary part of ε (Di Meo *et al.* (2019b)).

Results show that the dielectric properties of the produced mixtures are in line with our target, both when Polysorbate 80 and lecithin are used instead of dishwashing liquid. In particular, they show that it is possible to create relatively low-loss phantoms using the proposed waste-oil hardener instead of gelatine, and different surfactants instead of dishwashing liquid. It is clear from these graphs that the dielectric properties of the produced mixtures are similar when only the surfactant agent is changed, keeping the water and the sunflower oil amount unchanged. In addition, to highlight the increasing trend of the dielectric properties of the produced mixtures with the water content, in Figure 2.19, the values of dielectric permittivity of the four produced mixtures at 30 GHz are compared for the real and imaginary part.

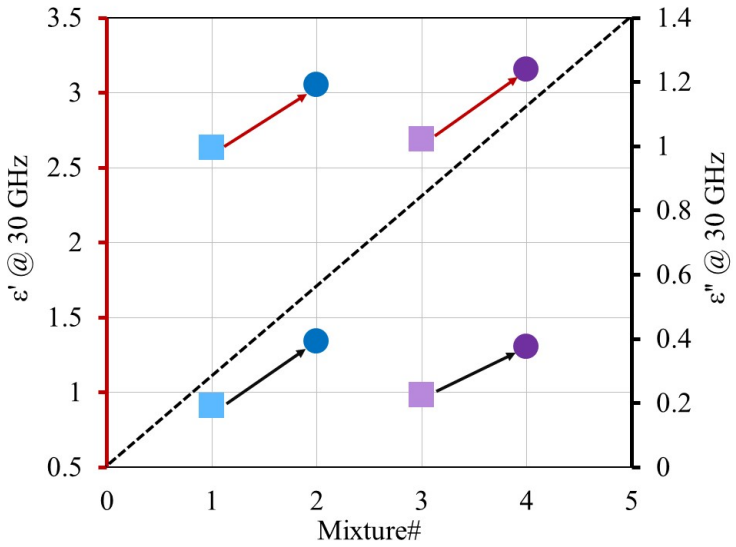

Figure 2.19. Comparison between the dielectric properties values at 30 GHz of *Mixture1/3* and *Mixture2/4* characterized by a higher water content, for real (upper side) and imaginary (lower side) part of ε. The arrows highlight the increase in values of dielectric properties with the water content (Di Meo *et al.* (2019b)).

All the presented results show that not only it is possible to create phantoms with very low values of dielectric properties, particularly favourable for an imaging system with a central working frequency of 30 GHz, but it is also possible to have a tight control of the dielectric properties of the produced mixtures by simply varying the involved water volume percentage.

Mixtures with waste-oil hardener and Polysorbate 80

During the mixture preparation described in the previous section, mixtures composed by only Polysorbate 80 showed to have promising dielectric properties, having permittivity values in line with our goal, as represented in Figure 2.20 a) and b) for the real and imaginary part, respectively. In addition, since it was found out that the waste-oil hardener dissolves in Polysorbate 80 in the same way as in sunflower oil, it was analyzed how the percentage of this component influences the dielectric properties of the produced mixtures, as done for gelatine in water. The same approach was not possible with lecithin, since the lecithin we used is a water-soluble powder component.
In Table 2.4, the ingredients of these new mixtures are presented.

TABLE 2.4. PHANTOM MIXTURE WITHOUT SUNFLOWER OIL AND WASTE-OIL HARDENER (Di Meo *et al.* (2019b)).

	Ingredients		
Mixture Name	Polysorbate 80 (ml)	Waste-oil hardener (g)	Deionized water (ml)
Polysorbate 80	25	-	-
Mixture5	25	0.8	-
Mixture6	25	2	-
Mixture7	50	2	2.6
Mixture8	50	2	5.6

For the mixtures not involving the deionized water (*Mixture5* and *Mixture6*), the procedure is very easy, indeed, the waste-oil hardener has been added to the Polysorbate 80, continuously stirred on a magnetic hot-plate and heated up to 70°C (temperature for which the waste-oil hardener dissolves), then poured in a proper mould. While, for the others (*Mixture7* and *Mixture8*), the water was added to the Polysorbate 80 at room temperature and vigorously stirred till an emulsion was formed, then the waste-oil hardener was added and the mixture heated up to 70° C (temperature for which the waste-oil hardener dissolves) and finally poured in a proper standard mould.

The comparison between the dielectric properties of the produced mixtures and the ones of low-density tissue *ex-vivo* samples, Di Meo *et al* (2018a), is shown in Figure 2.20 a) and b) for real and imaginary part, respectively. As in the previous cases, the shaded region is representative of one standard deviation for *Low density ex-vivo* tissues (Di Meo *et al* (2018a)).

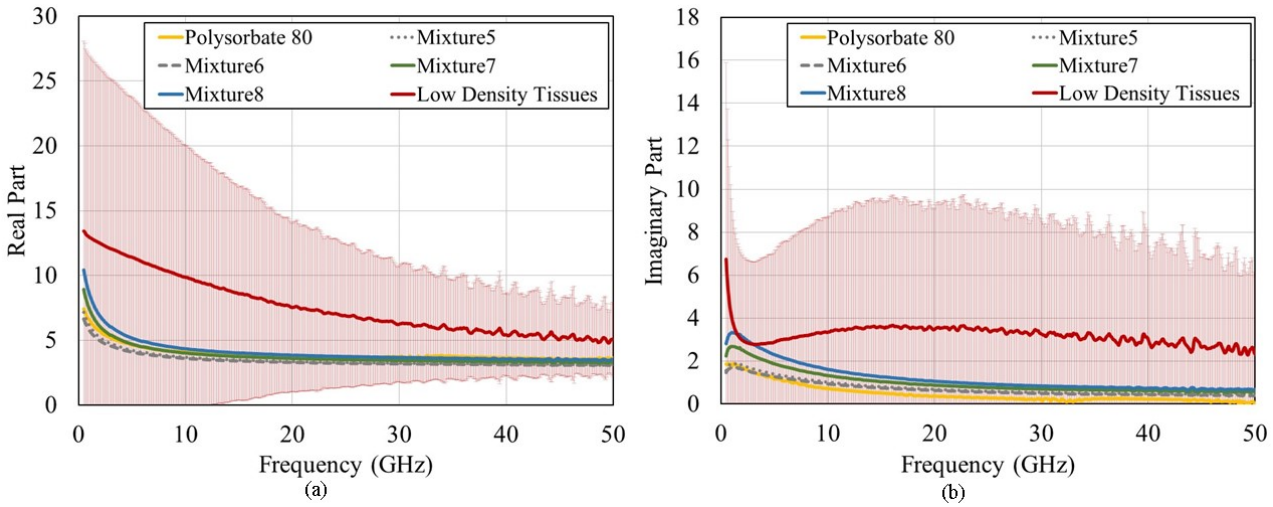

Figure 2.20. Comparison between the average dielectric properties of low-density breast *ex-vivo* tissues (mean ± standard deviation) and the dielectric properties of the produced *Mixture5/6/7/8*, for (a) real and (b) imaginary part of ε (Di Meo *et al.* (2019b)).

Mixture5 and *Mixture6* are intended to show the impact of the waste-oil hardener on the dielectric properties of the produced mixture, and in Figure 2.21 the values of their dielectric permittivity (both real and imaginary) at 30 GHz are shown. *Mixture7* and *Mixture8*, instead, have been prepared adding two different amounts of deionised water in a mixture composed only by Polysorbate 80 and waste-oil hardener, in order to check if it is possible to control the dielectric properties of the produced mixtures by adding water also in this class of recipes, and in Figure 2.22 the values of real and imaginary part of the dielectric permittivity of these mixtures with different percentages of water are plotted, as an example, at 30 GHz.

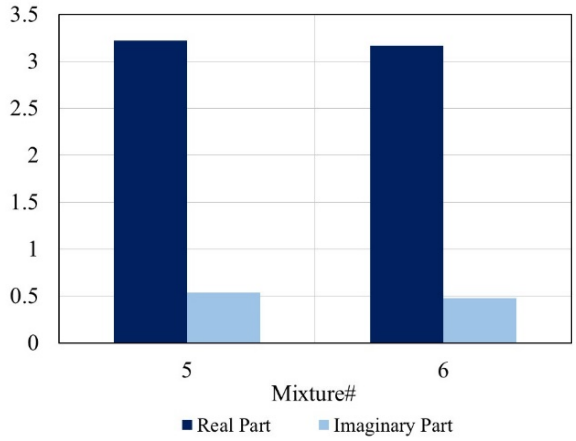

Figure 2.21. Comparison between the dielectric properties of the two mixtures (*Mixture5* and *Mixture6*) composed by a different amount of Kokubo, as summarized in Table 2.4 (Di Meo *et al.* (2019b)).

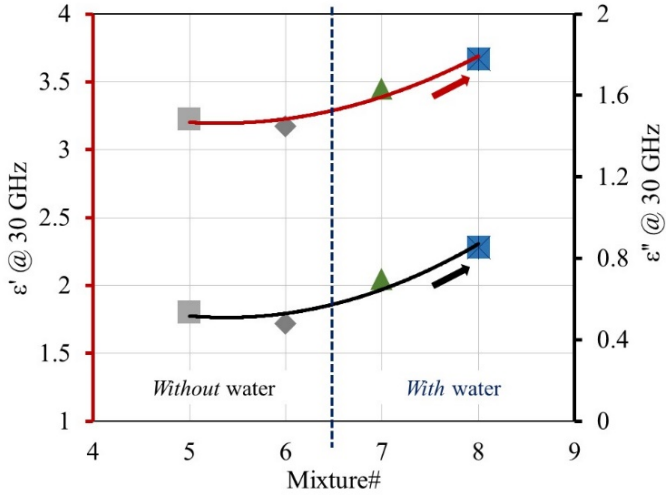

Figure 2.22. Comparison between the dielectric permittivity values at 30 GHz of *Mixture5/6* and *Mixture7/8*, which are characterized by a higher water content, for real (red scale) and imaginary (black scale) part (Di Meo *et al.* (2019b)).

From all these graphs, it is clear that for mixtures composed by Polysorbate 80 and two different amounts of waste-oil hardener no significant dielectric differences exist, as shown in Figure 2.21. The only difference is in the stiffness of the produced mixture (that was not mechanically characterized, because of the characteristics of this solidified mixture). In addition, what is evident from Figure 2.22 is that it is possible to change the dielectric properties of the produced mixture also when sunflower oil is not involved in the recipe, even if the intrinsic dielectric behaviour of the Polysorbate 80 sets a minimum in the achievable dielectric permittivity for this particular set of mixtures.

This last set of phantoms, composed only by Polysorbate 80 and waste-oil hardener, is of particular interest for the breast imaging at millimetre waves, since not only show very low values for the dielectric properties (mimicking the outlier of the *Low density* tissues category) but also is very easy to produce in large quantity; therefore, allowing the production of bigger phantoms without mixing problem.

Breast phantom

In Figure 2.23, a first example of a breast phantom, emulating a tumor mass inside a gelatine-based homogeneous tissue is presented. This phantom was intended to demonstrate both the capability of creating big phantoms (not easy to achieve, because of the difficulty of mixing high quantities of water and oil) and the

inclusion procedure of a gelatine-based target within a gelatine-based phantom. It was not used for the imaging test of the millimetre wave prototype, as the losses of this category of healthy tissues (*medium density*) do not make it possible to scan the scenario in the millimetre wave regime. The skin layer was not included. The phantom is composed by G5O50 (*medium-density* tissue) with a G16O20 (tumor tissue) target embedded in it. The produced phantom mimicking the dielectric properties of healthy tissue has a diameter of 12 cm (Figure 2.23 a)); while, the inclusion of the tumor-like phantom is clearly visible in Figure 2.23 b). The inclusion was inserted by pouring the healthy-like mixture at around 50°C on the frozen tumor-like phantom, suspended in the mold by means of a wire, which was then removed after pouring the compound of healthy-like mixture. During the manufacturing process of the phantom mimicking the dielectric properties of healthy tissues, pink food colouring was also added (a few drops were added when the mixture reached 50°C while mixing, just before pouring the compound into the mould) to create the colour contrast between the healthy-like mixture and the tumor-like one, necessary to make the inclusion visible, as well as making the phantom itself more realistic in colour.

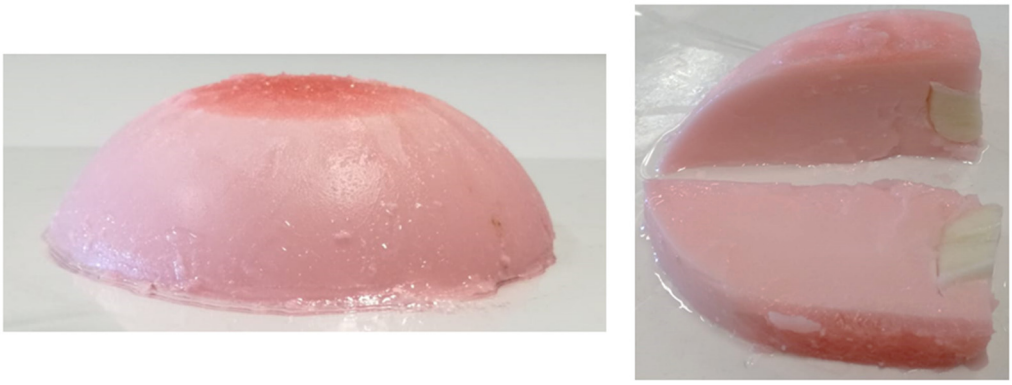

Figure 2.23. (a) Lateral view and (b) section of the heterogeneous breast phantom, composed by G5O50 and with a G16O20 inclusion (Di Meo *et al.* (2019a)).

Conclusions

In this chapter, new recipes based on cheap, easy-to-manage and not-toxic components for the production of tissue-mimicking breast phantoms are proposed. In particular, two classes of recipes are analysed. The first group involving deionized water, gelatine, sunflower oil and common dishwashing liquid, and it is demonstrated that the dielectric properties of the produced mixtures can be tuned by changing the volume percentage of oil within the mixture, and, in this way, the dielectric properties of all kinds of human breast tissues, healthy and malignant, can be mimed. The second group, on the other hand, involves different surfactants (in particular the Polysorbate 80) and a waste-oil hardener, with or without the sunflower oil. In this case, the dielectric properties of the achieved mixtures can be changed by adding a relatively small percentage of deionized water within the mixture; this second class of recipes is intended to emulate the dielectric properties of very fat human breast *ex-vivo* tissues (named "*Low density* tissues").
The dielectric properties of all the produced mixtures are measured with the open-ended coaxial probe in the frequency range [0.5-50] GHz and are compared with the ones of human breast *ex-vivo* tissues, derived from the two experimental campaigns performed at the European Institute of Oncology in Milan, in 2014 and 2016 (Martellosio *et al.* (2015, 2017) and Di Meo *et al.* (2017b, 2018a)). The impact of the amount of the gelatine as solidifying agent on the dielectric properties of the produced mixtures is also analyzed, showing that it can be increased to better mimic the mechanical properties of tissues in a more realistic way (in particular, for mimicking neoplastic tissues), without significantly affecting their dielectric properties. However, a more

accurate characterization of the elastic properties of the produced phantom should be foreseen as a perspective of this work.

In addition, a preservation strategy based on the use of sunflower oil is proposed for the gelatine-based phantoms. The dielectric properties of the produced phantom preserved in oil and deionized water are measured over 10 days and the results are compared to the ones of the phantom left in air. This approach showed the good capability of the sunflower oil of preserving the dielectric properties of the produced gelatine-based mixtures over time. On the other hand, the sample left in air undergoes the water evaporation; while, the phantom sample preserved in water absorbs water with the consequent increase of its dielectric properties.

In conclusion, a first heterogeneous phantom composed by healthy-like gelatine-based tissue with an inclusion of a tumor-like gelatine-based inclusion is shown.

CHAPTER III

TEST OF THE MM-WAVE PROTOTYPE ON BREAST PHANTOMS

Introduction

Several prototypes of microwave imaging systems for breast cancer detection have been proposed worldwide since many years (e.g., Meaney *et al.* (2000), Grzegorczyk *et al.* (2012), Nilavalan *et al.* (2005), Klemm *et al.* (2009), Klemm *et al.* (2010), Henriksson *et al.* (2011)). The most common approaches for microwave imaging are tomography and/or radar based, depending on the kind of signal that is acquired, that could be transmitted and/or reflected. The aims of the two approaches are different, even if both of them rely on the dielectric contrast between healthy and malignant tissues. In particular, in the microwave tomography, the aim is the reconstruction of the dielectric profile of an object starting from the measurement of the microwave energy transmitted through the object itself. Very promising results have been achieved using this approach, in particular by the Dartmouth University (Meaney *et al.* (2000), Grzegorczyk *et al.* (2012)); however, this technique is based on the solution of an inverse scattering problem by means of a non-linear and usually ill-posed problem. Therefore, this approach is vulnerable to several uncertainty degrees and usually the algorithms for image reconstruction are computationally very expensive.

On the other hand, the radar-based approach makes use of the backscattered signals to detect the possible presence and eventually the position of a dielectric anomaly, using the same principle of the Ground Penetrating Radar. The objective of the radar approach is to determine if a stronger scatterer is present or not within the illuminated geometry, determining eventually its position within the investigated scenario. However, since in this technique the spatial focusing of the signal is fundamental, the collection of as much signals as possible is required. Different prototypes based on this approach have been recently proposed, and some of these systems have reached a high maturity level, being tested in a clinical environment on up to 400 women (Grzegorczyk *et al.* (2012)).

On top of this fundamental distinction, a microwave imaging system can rely on different kinds of antenna arrays. In particular, the antenna arrays could be of three kinds: *synthetic* (transmitting and/or receiving antennas move around the whole breast for the complete scanning); *hardware* (all the antennas are physically present within the array), but with the array allowed to rotate in order to collect a double scanning of the breast (sometimes necessary for the calibration); *stationary*, where no moving parts are present. All of them have some pros and cons. In particular, *stationary arrays* if on one hand provide a mechanically easy equipment, on the other hand make difficult the system calibration. *Hardware arrays* have the advantage of not having moving parts, that could possibly provide the collision between antennas and between antennas and the patient

breast, but at the same time the system calibration could be difficult because of the rotation of an array with a very high number of antennas. Lastly, *synthetic arrays* are easy both from a hardware point of view and for the system calibration; however, because of the presence of moving parts, the noise floor could be high. In addition, an accurate design of the antenna movement is necessary, in order to avoid the collisions both between antennas and between antennas and the patient breast. The kind of array has also an impact on the acquisition time, a fundamental point that has to be taken into account in the system design in order to manage the unwanted patient movements.

Basing on different signal acquisitions (therefore, relying on tomographic or radar approach), possibly different woman positions (details given in the introduction of this thesis) and different array configurations, several microwave imaging systems for breast cancer detection have been proposed and, to open this chapter, an overview of the most advanced systems is given.

The most developed tomographic system was proposed at the Dartmouth College by Meaney *et al* since 2000 (Meaney *et al.* (2000)), and currently tested on 400 patients with and without diseases (Grzegorczyk *et al.* (2012)). On the other hand, within the category of *radar imaging approaches*, the two most developed systems are the ones proposed by the research group at the Bristol University (Nilavalan *et al.* (2005), Klemm *et al.* (2009), Klemm *et al.* (2010), Henriksson *et al.* (2011)) and the one proposed by the University of Calgary (Fear *et al.* (2013)), even if other radar-based systems were presented by the McGill University in Canada (Porter *et al.* (2016a)), in 2016, and tested on 13 women; by the Southern University of Science and Technology (Yang *et al.* (2017)), China, in 2017, and tested on 11 Asian women; by the Hiroshima University (Song *et al.* (2017)), Japan, in 2017, and tested on 5 women; and by the Shizuoka University (Kuwahara *et al.* (2017)), Japan, but without clinical tests on patients.

In (Meaney *et al.* (2000)), a **tomographic imaging system** for breast cancer detection is introduced. In particular, an array of 16 monopole transceiving antennas working in the frequency range from 300 MHz to 1 GHz is proposed. The system involves the prone position of the woman during the test with the breast submerged in a tank of coupling medium. The test of the prototype is done on phantoms and then on five post-menopausal patients, with a total acquisition time from 10 to 15 minutes for each breast. The array is vertically moved in seven positions from the chest wall to the nipple, and for each scanning, a 2-D image is produced. In this case, the system calibration is done by subtracting the measurements with the breast to the measurements without the breast in the tank (therefore, with the tank filled only of coupling medium). A 0.9% of saline solution is used as coupling medium. In this way, they demonstrated that the dielectric properties of *in-vivo* tissues are higher than the ones measured on *ex-vivo* tissues, and they highlighted the need of using a proper coupling medium with dielectric properties as similar as possible to the ones of the breast in order to avoid the strong reflection at the interface.

In (Grzegorczyk *et al.* (2012)), a tomographic imaging system improved, both in terms of hardware (allowing to detect signals compatible with sub-centimetric resolutions in 3-D images) and in terms of acquisition times (lower than 2 minutes), with respect to the one proposed in 2010 by the same research group is presented. The test of the prototype, this time, is done on over 400 women at the Dartmouth Hitchcock Medical Center, and the results about the suitability of this approach both for tumor detection and for the monitoring of the therapy on two patients is reported in this paper. As for the prototype proposed in 2010 (Meaney *et al.* (2000)), the system is composed by 16 monopole antennas; each antenna transmits in turn and the remaining 15 antennas receive the signals. Antennas near the transmitting antenna actually collect the reflected signal, while antennas on the opposite side of the transmitting antenna collect the transmitted waves. Measurements in 11 frequency points up to 3 GHz are done, and a coupling medium made by water and glycerine is used. Good results in terms of the local dielectric properties of the illuminated tissues are demonstrated; however, the strict

requirement of a sophisticated hardware to detect signals as low as -140 dB is highlighted, since the useful signals are attenuated by the presence of the coupling medium.

For what concerns the **radar based approach**, the system belonging to the University of Bristol, named MARIA (Multistatic Array Processing for Radiowave Image Acquisition), was introduced in 2005 and it has been recently tested on more than 90 patients with and without the disease (Nilavalan *et al.* (2005), Klemm *et al.* (2009), Klemm *et al.* (2010), Henriksson *et al.* (2011)). In particular, in Nilavalan *et al.* (2005), for the first time an array of patch antennas with 16 physical elements connected through a switch matrix with 16 channels to a VNA was proposed. The central working frequency of this system is 7 GHz, with a bandwidth of 3 GHz, and the total duration of the scanning was 2.5 minutes. In this system, each antenna transmits a wideband impulse and all others collect the reflected signal. The calibration of the signals is achieved by the array rotation, even if the problem of the skin reflection removal was highlighted, as the array rotation fails for subcutaneous targets.

In (Klemm *et al.* (2009)), a modified version of the microwave imaging system for the diagnosis of breast cancer was proposed, this time based on an array of 16 UWB aperture-coupled stacked-patch antennas in a hemispherical configuration. In this systems, the multi-static radar architecture was still used, with the 16 antennas connected to a VNA through a switch matrix, selecting in turn the couple of antennas for the collection of the S21. The total scan time was 3 minute, and both the array and the imaged object were submerged in a coupling medium with dielectric properties similar to the ones of fat tissues during the scanning. Also in this case, the signal calibration was done by rotating the array and some tests of the prototype on simplified phantoms were done, demonstrating the potentiality of the system.

Starting from these preliminary tests of the prototype, the same research group proposed versions always improved of this system, involving both higher and higher numbers of antennas, by 60 radiators, and shorter and shorter acquisition times. In particular, in 2010, a system based on 32 antennas was proposed and tested both on more complex phantoms and on real patients, showing some limitation when dense breasts were scanned (Klemm *et al.* (2010)). While, in Henriksson *et al.* (2011), an array architecture involving 60 antennas, in semi-spherical configuration, with a total acquisition time of 10 seconds, working the frequency band [4-8] GHz, was proposed. To fit breast of different dimensions to the tank containing the antennas, a low loss ceramic shell of variable dimensions was placed and the paraffin as coupling medium was used to avoid the presence of air bubbles. Also in this case, the signal calibration was achieved by rotating the array and good detection capability were demonstrated by testing the system on 95 patients.

A different radar-based imaging system, named TSAR (Tissue Sensing Adaptive Radar) system, is proposed by the University of Calgary. In 2013, the research group of Calgary proposed the microwave imaging system for breast cancer detection based on the use of the mono-static radar approach in which the same antenna transmits and receives (Fear *et al.* (2013)). In this approach, the woman is in a prone position with the breast submerged in a tank containing coupling medium and sensors. The sensor is composed by an antenna and a laser and is attached to a mechanical arm, in order to move the sensors in vertical direction. In addition, the whole tank is allowed to rotate. The UWB antenna performs a scanning around the breast by transmitting and receiving UWB monostatic signals in the band from 50 MHz to 15 GHz. The laser makes possible the demarcation of the volume of interest; therefore, the exact position of the breast is identified, allowing for the precise identification of the breast contours and improving the skin reflection removal algorithms. The antenna is connected to a VNA through a coaxial cable. Canola oil is used as coupling medium and a BAVA-D antenna is adopted. In order to reduce the noise floor, an IF bandwidth of 1 kHz is used and the measurement over three sweeps in frequency is done. Measurements are done in the frequency domain, even if the signal processing is performed in the time domain. The system calibration is done by subtracting measurements with and without

the breast (empty tank). The skin reflection removal is done by using a proximity method, by subtracting the average of the signals aligned along a given line from the actual received signal from an antenna. After this calibration procedure, all the waveforms backscattered and collected are temporally shifted and then summed in order to create a synthetic focal point. By changing the temporal shift of all the waveforms, the position of the focus is scanned within the whole breast. If a dielectric lesion, as a malignant tissue, exists in a particular focal point, then all the waveforms would add coherently; otherwise, they cancel each other. This prototype is tested on 8 alive patients with and without anomalies; however, despite the good detection capability, the two main limitations of this approach are a limited system dynamic range, in the order of -80 dB, and the long test duration.

At the McGill University, Canada, Porter *et al* presented in 2016 two kinds of multi-static radar architectures for breast cancer detection. On one side, in (Porter *et al.* (2016a)), they introduced a bulky and fix table equipment in which the woman is in prone position with the breast pending in a tank, and they tested the prototype on 13 healthy patients (ages from 21 to 76 years) to identify some variability factors affecting the monthly measurements, from the biological variability to the measurements variability. This system is composed by 16 sensors placed in a hemispherical shell in which the breast is inserted for the imaging test, with the aim of using this system both for the breast cancer detection and for the monitoring of the efficiency of the chemotherapy treatments. The frequency band used in this prototype is [2-4] GHz. The 16 resistively loaded travelling-wave antennas are connected to a VNA through a switch matrix, and in turn one antenna transmits while all others receive. All measurements are done in the time domain, and the common Ultrasound gel is used as coupling liquid. In this system, the volume of coupling medium depends on the dimension of each breast (therefore, it changes among patients); however, Porter *et al* demonstrated that this variety in the amount of coupling medium, together with the patient movement, are two of the main causes of measurement uncertainty. In addition, to reduce the measurement noise, averages on 32 measurements are done.

A different equipment for breast imaging was presented by the same group in (Porter *et al.* (2016b)), where a wearable bra is proposed. In this case, the imaging prototype is based on 16 flexible antennas placed in a bra exploiting the multi-static radar architecture. However, in this configuration, no coupling medium is used and the breast surface is immediately located. The frequency band used in this prototype is the same of the table equipment and goes from 2 to 4 GHz. The coupling medium in this configuration is not needed, and by comparing these results with the ones derived from the measurements using the table equipment they demonstrate the improvement in the achieved results (due to the exact localization of the breast surface, the correct positioning of the breast and the absence of coupling medium). In this case, to reduce the noise floor, an average on 16 measurements is done, and the complete scanning of the breast has a duration of 6 minutes.

A synthetic multi-static radar architecture based on two horn antennas in the frequency band [4-8.5] GHz is presented by the Southern University of Science and Technology, in China (Yang *et al.* (2017)). The proposed system is tested on 11 healthy women with ages from 22 to 47 years. The patient is in a prone position with the breast pending in a tank and the antennas are rotated around it. The scanning is done slice-by-slice in the frequency domain, and an improved version of the DAS algorithm is used to create the image. The two antennas are placed in a plastic tank filled by corn oil, used as coupling medium. This prototype is tested on 11 women, both healthy and sick, demonstrating good results.

In (Song *et al.* (2017)), a portable pulsed radar system for the breast tumor detection is proposed and tested on breast excised by a mastectomy surgery. The system is based on a 65-nm CMOS technology, covering the frequency band [3.1-10.6] GHz with a central working frequency of 6 GHz. The woman is intended to be in a supine position during the test with the array placed over the flattened breast, and promising results are achieved both on silicone breast phantoms and on excised breast tissues after total mastectomy surgery.

In (Kuwahara *et al.* (2017)) a hybrid imaging method based on both radar UWB and tomographic approach is presented. In particular, a sort of microwave mammography is introduced. In this system, the coupling medium is not used; however, the presence of air bubbles is avoided by using a sucker within the system. A conformal array fixing the breast by the aspiration of the air is present between the breast and the antenna array. In this way, not only the air bubbles but also the patient movements are avoided. Since both in tomographic and radar technique a high number of scanning is necessary, the multiple polarization method is used. In the solution of the inverse scattering problem (necessary in the tomographic approach), information derived from the radar signals about the power distribution within the breast is used. The system proposed by the research group of the Shizuoka University is composed by a sensor, an aspirator, a switching system, a network analyser, a PC to control all the instruments and a workstation to process the data. The sensor is composed by a varying number of stacked patch antennas powered by a slot. The number of antennas depends on the breast dimension and all the antennas are embedded in a cup with the same dielectric properties of the breast adipose tissue and goes from 6 to 30 elements. The total scanning time is 5, 30 and 200 seconds, for a sensor with 6, 18 and 30 elements, respectively. The array rotation for the artefact removal is used. The system bandwidth is [1-3] GHz, and both the exact geometry of the breast and the distribution of the backscattered power from the geometry are derived from the radar approach and are used in the tomographic processing of the data, instead of a uniform initial distribution.

However, all the proposed microwave-imaging systems share similar operational frequencies, not exceeding a few gigahertz and, therefore, lacking in resolution in particularly fat breasts. A coarse resolution is a critical problem in a radiologic environment, since a low resolution is directly translated into a difficult morphological reference for the physician (Nikolova (2011), Klemm *et at.* (2012)). For this reason, in this Chapter, the design of the mm-wave imaging system for early stage breast cancer detection in particularly fat breasts is presented. In particular, basing on the dielectric properties of the woman breast *ex-vivo* tissues shown in Chapter I, the feasibility study of the system with a central working frequency of 30 GHz and a bandwidth of almost 20 GHz is firstly presented. Then, using the recipes explained in Chapter II, different kinds of phantoms are prepared and the synthetic mm-wave imaging prototype is tested after the discussion about the resolution and the Point Spread Function of the system.

Feasibility study of the system

The proposed imaging system for early-stage breast cancer detection is based on a multi-static radar architecture by means of the so called *Synthetic Aperture Focusing* approach, involving M antennas able to either transmit or receive a mm-wave signal. In particular, each time one antenna is used to transmit the signal and all the remaining M-1 antennas are used to receive the backscattered signal till all the antennas in the array have been used to transmit the signal, so M times.

The feasibility study of the system was done by means of the link-budget evaluation and it is summarized as follows (Di Meo *et al.* (2017)). In this approach, the number of transmitter-receiver combinations, as well as the times in which the backscattered signal -assuming a uniform backscattering in all directions from the target- is collected and coherently summed, is M(M-1); therefore, the received power is improved of a factor equal to $M(M-1)^2$. At the same time, the receiver noise (supposed to be incoherent) is integrated M(M-1) times. Therefore, the final Signal-to-Noise ratio (S/N), when all the received signals are equal each other (the ideal case could be reached only in a lossless environment or when all the paths are equal each other), is improved of a factor F=M(M-1), significantly enhancing the dynamic range of the system. However, in a not ideal or not lossless case what happens is that, while the noise is integrated M(M-1) times, the received power is function

of the actual collected signals, undergoing to significant attenuations at mm-waves since propagation losses (even among adjacent radiators) are very high.

Thereby, the addition of one radiator in the array not always corresponds to an improvement in the achievable Signal-to-Noise ratio and an optimum number of antennas within the array maximizing the S/N improvement exists. In particular, the S/N improvement tends to increase up to a certain threshold, beyond which the addition of one radiator does not translate in an improvement in the overall S/N ratio anymore. As an example, in Figure 3.1, this idea referred to a 5cm-depth target in a particularly fat breast (e'=3 and e''=0.3, Martellosio *et al.* (2015)) is plotted.

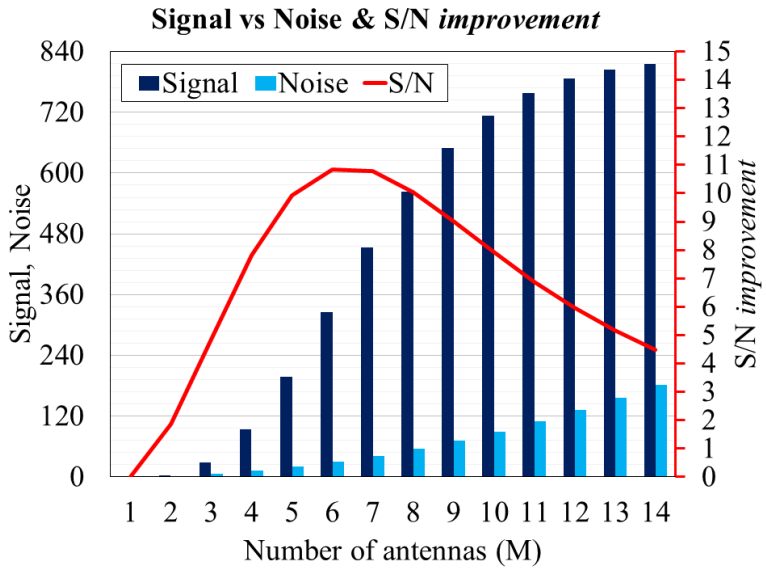

Figure 3.1. Example of S/N improvement for target 5cm within a very Low density tissue.

For this reason, it is ideally possible to divide the array in two parts, one in which the addition of one antenna provides an improvement in the overall S/N ratio and one in which the addition of one radiator corresponds only to a hardware complication without offering an effective improvement in the overall Signal-to-Noise ratio (sketch in Figure 3.2).

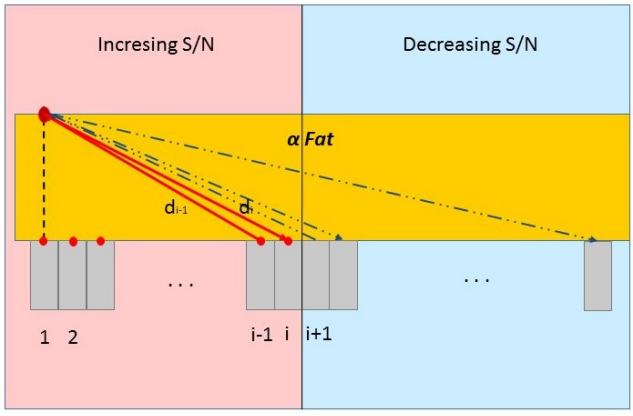

Figure 3.2. Schema of the working principle.

Basing on these considerations, a good starting point in the design of a mm-wave imaging system is the determination of a proper number of radiators in the array, as well as their reciprocal locations, in order to maximize the improving factor for a given penetration depth. For this reason, a feasibility study of the mm-wave imaging system was done in terms of link budget evaluation both for linear and conformal configuration

of the array, as these possibly correspond to the two positions of the woman during the diagnostic test. A sketch of both the architectures is shown in Figure 3.3 for a) linear and b) circular array.

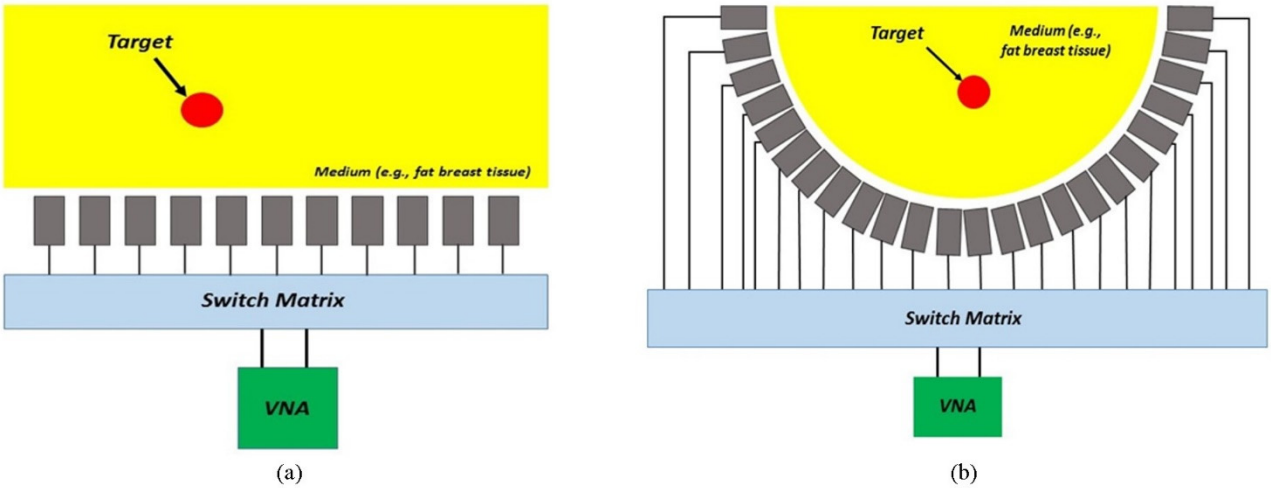

Figure 3.3. Sketch of the multi-static radar architecture for a) linear and b) circular configuration. Drawing not to scale.

In this theoretical study, safety, electronics and anatomical limitations were considered. In particular, the transmitted power was derived from a previous study on the human exposure to radiation in the mm-wave regime (Espin Lopez *et al.* (2016)), and it was set to Ptx= 20 dBm (100 mW), providing a maximum temperature increase of 1°C. At the receiver side, a Noise Figure of 10 dB (conservative margin, since receiver with lower NF are currently available (Wang *et al.* (2010), Vecchi *et al.* (2011), Hadipour *et al.* (2015)) and an imaging time compatible with human breast imaging on alive patients of 30 minutes (provided by medical doctors of the European Institute of Oncology in Milan) were considered. From these two parameters, imaging time and number of radiators, also the integration time (hence, the integration bandwidth) for each receiver was derived. Assuming that the system operates at room temperature, a receiver noise of around -150 dBm was also considered. In addition, extra losses taking into account the skin reflections and the target reflectivity equal to 20 dB (basing on the dielectric properties of the tissues) were included, as well as a final S/N greater than 30 dB, being this a realistic target at the output of the correlator, and resolutions in the order of some millimetres (around 8 mm) for penetration depths greater than 5 cm were demonstrated (Di Meo *et al.* (2017a)) in particularly fat breasts (ε'=3 and ε''=0.3, Martellosio *et al.* (2015)).

The outcomes of the numerical feasibility study for both the configurations were also verified by means of the full-wave simulations of several geometries. In particular, HFSS software was used. The radiators used in the simulated models were open-ended WR28 waveguides, with a fundamental-mode bandwidth from 26.5 GHz to 40 GHz. In all models, spheres with a diameter of 2 mm assumed to be made of tumorous tissue (e'=19.02 and e''=19.97, Martellosio *et al.* (2015)) were used to model the targets and the skin was not included. The calibration of the data was done by calculating two sets of scattering parameters, with and without the tumor, and then subtracting the scattering parameters without the target to the ones with it. As way of example, only two scenarios are reported in this thesis, linear (array composed by 28 antennas) and circular (array composed by 32 antennas), both involving two targets at two displacements and depths in a *Low density* healthy tissue with dielectric properties equal to ε'=3 and ε''=0.3.

The final set of calibrated data was used as input for the image reconstruction technique (given by the Bioengineering Laboratory of the University of Pavia), that is an improved version of the Delay-And-Sum algorithm (standard approach used for image processing, described in the following of this chapter), the Filtered-Delay-Multiply-And-Sum (F-DMAS) (Lim *et al.* (2008), Matrone *et al.* (2015)), and the results are shown in Figure 3.4 for the linear case and in Figure 3.5 for the conformal case (Di Meo *et al.* (2017c)).

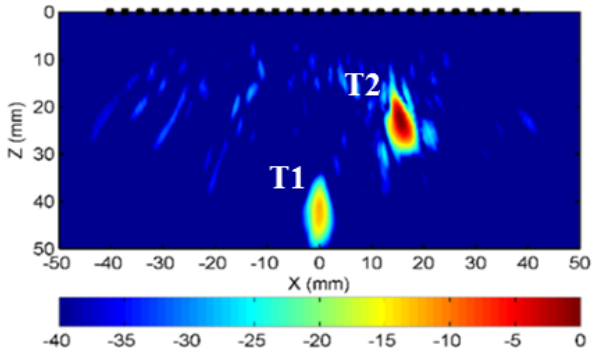

Figure 3.4. Reconstructed image for linear configuration with two targets using F-DMAS beam-forming (color scale in dB).

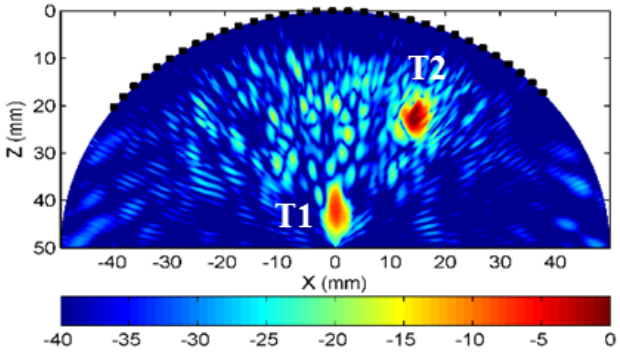

Figure 3.5. Reconstructed image for circular configuration with two targets using F-DMAS beam-forming (color scale in dB).

System description & experimental setup

The experimental setup for the mm-wave imaging measurements is composed by:

- Two mono-modal truncated double-ridge waveguides (PNR180) with cut-off frequency of the fundamental mode, TE10, of 15 GHz, and bandwidth [18-40] GHz;
- A two-port Vector Network Analyzer (VNA, Keysight E8361C), used to generate the signal and then receive the backscattered ones, collecting the scattering parameters for each configuration in the frequency band of interest;
- Two flexible coaxial cables to route the signal from the VNA to the two radiators, and vice versa;
- Four microstep actuators, supporting the two antennas, to generate the synthetic array;
- A personal computer to drive the actuators and the signal acquisition;

The whole imaging system is shown in Figure 3.6, while a sketch of the four actuators is shown in Figure 3.7 (credits of Moscato *et al.* (2013)).

The maximum achievable dimension for the aperture is 20,32 cm, corresponding to the length of each actuator. The distance between adjacent radiators was the same used in the feasibility study summarized above, and it was equal to 5 mm (half wavelength in air at 30 GHz to reduce the side-lobes). Because of the flange transition hindrance, the spacing between physically adjacent antennas could not be lower than 25 mm; while, all the subsequent spacings were achieved with the linear actuators and were equal to 5 mm. The array was composed by 24 antennas in 28 positions for a final dimension of the array of 13.5 cm.

Only two actuators were moved for these preliminary tests of the mm-wave prototype. The complete system is intended to include a full planar array of radiators allowing the 3-D image formation; however, the simplified version of the system allowing the creation of 2-D images was proposed as proof-of-concept and allowed to evaluate all the critical aspects related to radar imaging on realistic breast phantoms in the millimetre-wave regime. After this, the extension to a complete full planar array would be straightforward, as it would require only larger computational and mechanical resources.

The antennas were directed toward the floor and several anechoic panels were used to isolate the measurement environment by all the rest. A personal computer connected to both the VNA and the linear actuators was used to coordinate both the antenna shifts and the signal acquisition by means of a proper MatLAB routine. In addition, it was used in all subsequent signal processing phases, from the organization of the complete matrix, to the matrix calibration, to the image creation.

The Stepped Frequency Continuous Wave (SFCW) radar was used for the data acquisition. In the SFCW approach, each antenna-target-antenna combination is considered as a linear transfer function, with its behaviour defined by means of its measured scattering matrix. The amplitude and the phase of this transfer function between two antennas provide a complete information of the target, and this information is used as input in the image reconstruction process, after the calibration. The complete scattering matrix corresponding to the whole system is obtained by shifting in turn each antenna along the line and by measuring the S21 coefficient for each combination; then, the complete matrix is assembled.

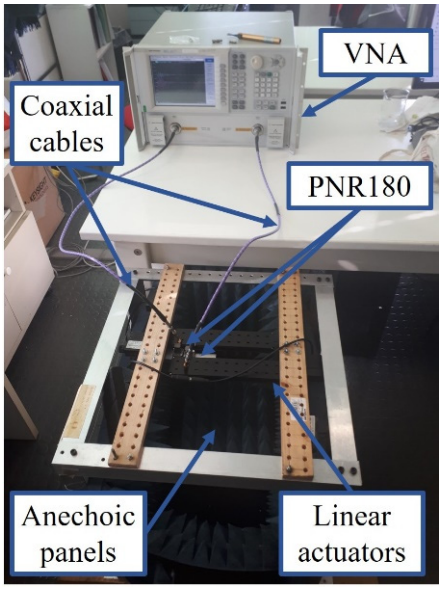

Figure 3.6. Experimental setup for imaging at mm-waves.

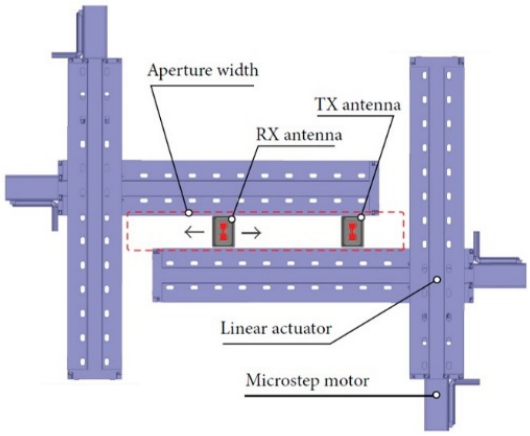

Figure 3.7. Sketch of the four actuators.

System calibration

Before using the signals for image reconstruction, the received signals have to be properly calibrated. In this configuration, indeed, due to the proximity between radiators, the mutual coupling is very large, therefore masking the contribution of all other useful signals reflected by the illuminated geometry (that are very weak).

This unwanted signal is usually referred to as the “Crosstalk” and it is easily removed by means of the subtraction between the measurement with and without the target. In this way, both the antenna coupling and the environment multiple reflections are suppressed.

In addition, also the phase of the received signal has to be properly adjusted, as this is influenced by several factors (like the propagation in the waveguides, the transitions, and the spurious backscattering). In particular, it is essential to fix the phase reference for imaging directly on the plane (or on the line, in the case of a linear array) of the phase centres of the transmitting and receiving antennas, since the imaging procedure makes use both of amplitude and phase information to reconstruct the image. To do this, a known calibration target is used, that is a metallic plate. This is a good standard, since its backscattering matrix is analytically known and the corresponding phase delay is directly related to its distance from the antennas.

Therefore, the complete calibration procedure is as follows. A first measurement with the metallic plate at a given distance in front of the array is done and the corresponding scattering matrix is calibrated by the crosstalk contribution (i.e., measurement with the plate minus measurement without the plate). The delay matrix corresponding to an ideal metallic plate at the same distance is analytically computed, where the elements of this matrix are complex numbers given by $e^{-j2\pi f\tau}$, where f is the frequency and τ is the time delay (Balanis (2005)). After this, the calibration of the whole imaging systems, made by cables, transitions and antennas, is achieved by means of the ratio between these two matrixes. Then, the measurement of the target (calibrated by the crosstalk) is multiplied by this correction matrix and the final result is used in the image reconstruction procedure.

This approach is valid in general and no further steps are required for target detection in air (Ahmed *et al.* (2011)). However, for target detection within realistic breast phantoms, an additional step is required. In this case, indeed, the calibration procedure has to take into account also the artefacts due to the strong reflection at the interface air-phantom. This contribution both for the proximity of the phantom to the antenna array and for the propagation of the signal in air (therefore, a relatively significant dielectric contrast with the phantom), is very high and masks the late-time signal contribution, that usually contains information about tumor presence. The use of a proper coupling medium could reduce this contribution; however, due to the difficult maintenance of the system submerged in oil and the problems related to the sterilization between consequent uses on different patients (in a potential clinical environment), as well as the not easy use of the calibration procedure described above in presence of the coupling liquid, in this work, no coupling medium is used. To solve this problem, the time-gating approach is adopted; therefore, the image is reconstructed starting from the end in time and space of the interface.

Phantom preparation

The phantoms on which the prototype of the imaging system was tested were intentionally produced from the recipes proposed in Chapter II, modified appropriately to mimic the dielectric properties of different types of human tissues within the category of *Low density* tissues. In particular, within the range of one standard deviation, two phantoms with dielectric properties below the mean of *Low density* tissues and one above the mean were produced. The numbering of phantoms corresponds to the increasing values of dielectric properties, as well as to the logical and temporal progression with which the tests were performed. To mimic the tumor target both a cylinder of deionized water and gelatine or a cylinder of deionized water and agar (both with diameter of 8 mm) was used to demonstrate the inclusion procedure, then, to mimic a more realistic target, a currant was used as spherical target with diameter of around 8 mm.

For all the phantoms, the procedure for phantom preparation was described in Chapter II.

After the mixtures solidification, their dielectric properties were measured in the broad frequency range [0.5-50] GHz by means of the equipment described in Chapter I and Chapter II. In Figure 5.8 a)-b) the comparison between the dielectric properties of the three phantoms and the ones of human breast *ex-vivo Low density* tissues for real and imaginary part is shown. The shaded region is representative of one standard deviation.

The inclusion of the cylinder of water and gelatine/agar in all the three categories of phantoms was obtained by pouring the entire mixture into the mould and, after its complete solidification, recreating a cylindrical opening of the same size as the inclusion in the phantom, into which was poured the mixture of water and gelatine/agar at 45 ° C. Then, the complete phantom was left into the fridge to solidify.

For the inclusion of currant, the mixture was poured up to a certain level in one mould, and then it was left in the fridge up to its partial solidification. At that point, the currant was included in the centre of the lower phantom and the other part (that was continuously stirred at controlled temperature of around 60°C) was poured on the lower phantom and the currant up to a certain level, corresponding to the target depth.

In all these cases, the pouring process provided some air bubbles, a quite common problem in this phase (Garrett *et al* (2015), Mashal *et al.* (2011)).

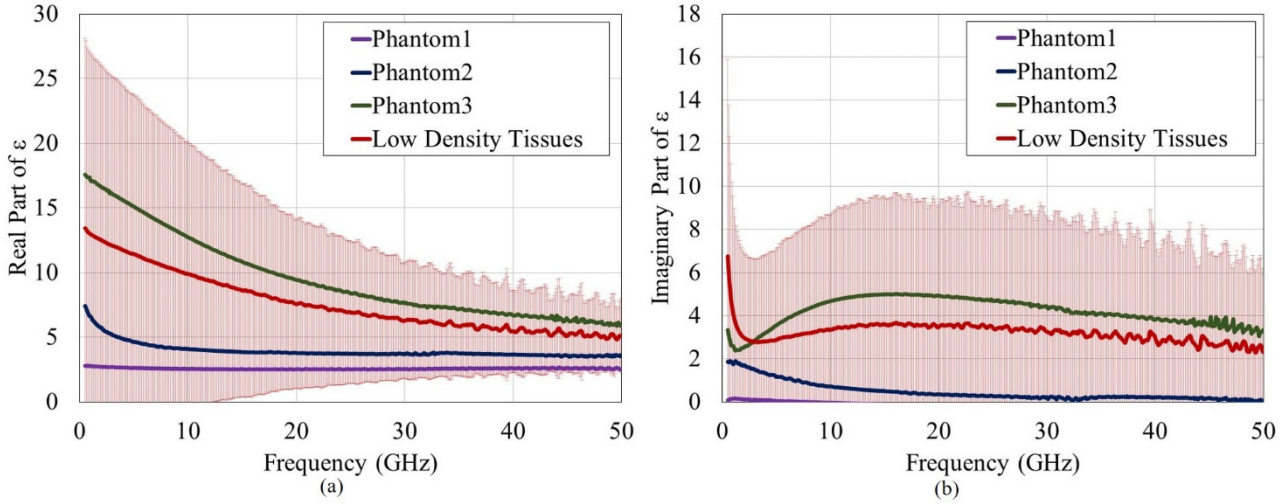

Figure 3.8. Comparison between dielectric properties of the Polysorbate 80- and SunFlower Oil (SFO)- based phantom and the human breast *ex-vivo Low density* tissues for a) real and b) imaginary part.

In Figure 3.9 a) and b), a photo a) of the phantom during the inclusion process of the cylinder made by water and gelatine/agar, and b) a photo of the final phantom is shown. Figure 3.10 shows a photo of the phantom during the procedure of inclusion of the currant.

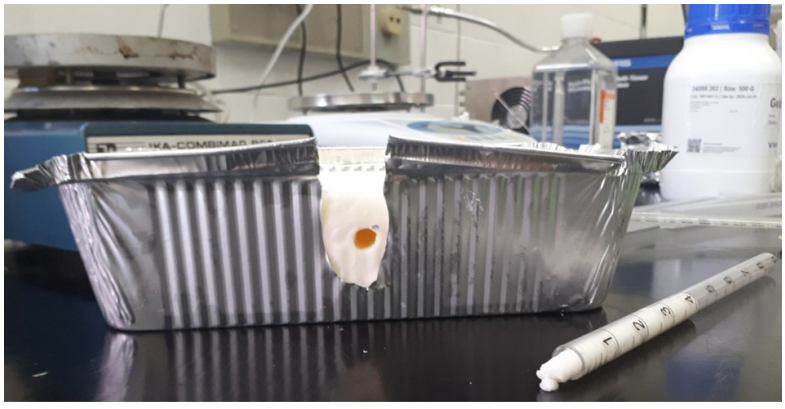

(a)

(b)

Figure 3.9. Photo a) of the phantom during the inclusion process of the cylinder made by water and gelatine, and b) a photo of the final phantom.

Figure 3.10. Photo of the phantom during the procedure of inclusion of the currant.

Delay-And-Sum (DAS) algorithm

Despite the current availability of more sophisticated imaging algorithms, all the images presented in the following of this chapter have been obtained on purpose using the basis of all the imaging algorithms in question, the Delay-And-Sum (DAS) algorithm, so as not to hide any hardware limitations with the software improvements. The DAS algorithm is the easiest beamforming procedure for image reconstruction. In the DAS algorithm, for each point of the imaged area, the antenna-point-antenna time delay is computed by the geometrical computation of the distances from the transmitting antenna to the point and from the point to the receiving antenna. In particular, the time delay is evaluated by doing the ratio between the length of the signal propagation path and the average speed of the signal within the propagation medium (of which, the dielectric properties are known *a-priori*). Basing on these time delays, the signals for each focal point are aligned and the signals corresponding to each point are coherently summed between them. What is expected is that if in that point a target is present, all contributions coming from that point sum coherently providing a very strong signal; otherwise, if a target is not present, all contributions sum incoherently each other, producing a less intense signal.

The Bioengineering Laboratory of the University of Pavia provided the DAS algorithm.

In Figure 3.11, the schema showing the DAS procedure for each focal point is presented.

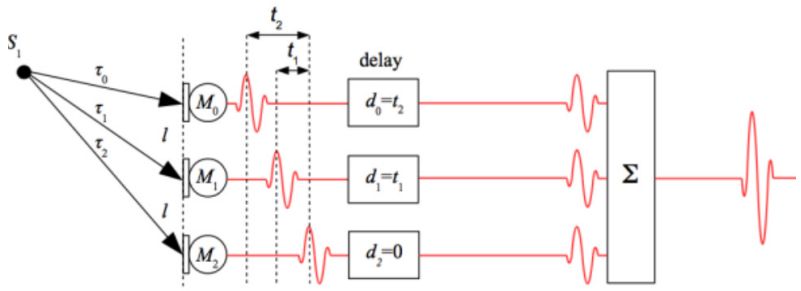

Figure 3.11. Schema of the DAS procedure for each focal point (credits of Król *et al.* (2015)).

Point Spread Function (PSF)

The Point Spread Function is a parameter describing the response of an imaging system to a point source or to a point object, or equivalently the PSF can be seen as the impulse response of a system. From a practical point of view, the PSF could be thought as the extended blob in the image representing a single point object, depending on the blurring of the point object, the PSF gives a direct measure for the quality of an imaging system.

In general, PSF describes the resolving ability of an imaging system. From a practical point of view, if we have a point emitting source its corresponding image will appear to have a finite size and this enlargement is due to the process of spatial filtering. Since PSF gives us a measure of how a point source is mapped into an image, the close correlation between the concept of PSF and resolution is appreciable. Let's imagine, for example, that we have two point sources in the scenario of interest and suppose we put these two sources closer and closer together. Since each point source in space is identified on the basis of its characteristic PSF, the PSFs corresponding to each point source as the two sources approach each other will begin to overlap in the image plane until they reach a point where they are indistinguishable. For this reason, the two PSFs can only be distinguished from each other if the maximums of the PSFs of the two sources have a greater separation than the characteristic width of an individual PSF. In addition, resolution is defined as the smallest distance between two small, but detectable targets that can be distinguished in an image. Therefore, for these considerations, the narrower the PSF, the better the resolution will be.

Two full-wave simulations (using software Ansys HFSS) were done to determine the simulated PSF of the proposed mm-wave imaging system with central working frequency of around 30 GHz and bandwidth [26.5-40] GHz. Both the simulated full-wave models included 28 rectangular waveguides in a linear configuration in air, with a distance between phase centres of adjacent radiators of half wavelength at 30 GHz in air, 5 mm. The targets were: a) a metallic sphere with diameter of 2-mm, and b) a sphere with dielectric properties of human malignant tissue with diameter of 2-mm. In particular, the simulation a) was done to evaluate the PSF of a perfect scatterer (punctiform-like, in accordance with the guidelines published by Amineh *et al.* (2015) for the evaluation of the PSF for a radar system), while case b) was done to evaluate the PSF of a not-perfect, but punctiform-like, scatterer. In these simulations the final dimension of the array was 13.5 cm. In both cases, the target distance was 4 cm from the center of the array. The time duration for each single simulation was around six hours. In addition, the computation effort for each simulation was significant, since around 600 GHz of disk space was necessary. A screenshot of the simulated model for both cases is reported in Figure 3.12, and the achieved resolutions will be summarized in Table 3.1, after the description of the formulas for the evaluation of the resolution.

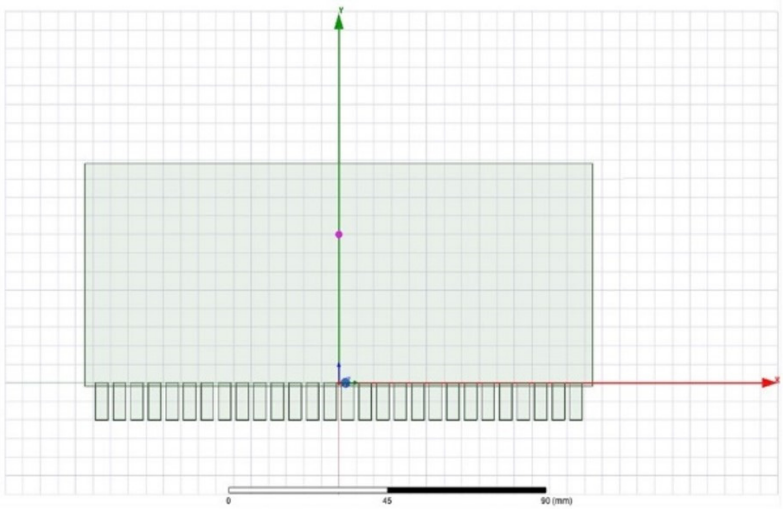

Figure 3.12. Screenshot of the simulated models.

Resolution

The resolution of a system is defined as the smaller detail that can be detected in an image, or, alternatively, as the smaller distance between two very small, but detectable, targets that could be distinguished in an image (Nikolova (2011)). The formulas for the range, δr (IEEE), and lateral, δxy, (Balanis (2005)) resolution are:

$$\delta r = \frac{v}{2B}$$

$$\delta_{xy} = \frac{\lambda}{dxy} L$$

Where v is the wave speed within the propagation medium, B is the signal bandwidth, λ is the wavelength, dxy is the array dimension, and L is the target distance from the array.

Range resolution is not depending on geometrical parameters; while, the lateral resolution is a far-field parameter depending both on the dimension of the array and on the target distance from the array. Therefore, some consideration about the lateral resolution is needed.

In the formula of lateral resolution, the size of the array is present. However, even if the physical size of the array used in our models in air is 13.5cm, it cannot be considered directly in the formula for calculating lateral resolution for several reasons. First, the system proposed for the intended application works in the near-field region, while the formula is derived in the far-field condition. Secondly, due to the proximity of the target from the array, the relative antenna-target-antenna path for antennas close to the target is significantly different (much smaller) from the antenna-target-antenna path for antennas far from the target; therefore, the backscattered signals toward distant antennas are strongly attenuated in the propagation path to and from the target, arriving in some cases so attenuated to the receiver side that they can no longer be detected. In this case, it is therefore not surprising if the achieved lateral resolution is different from the theoretical one (calculated considering the physical size of the array), because the equivalent actual size of the array that transmits and receives signals is smaller than the physical one.

Therefore, on the basis of these considerations, the calculated theoretical resolution can only give us an indication about the order of magnitude of the expected resolution.

The figures corresponding to the two simulated cases are reported in Figure 3.13, 3.14; while, the resolution achieved in the two cases is summarized in Table 3.1.

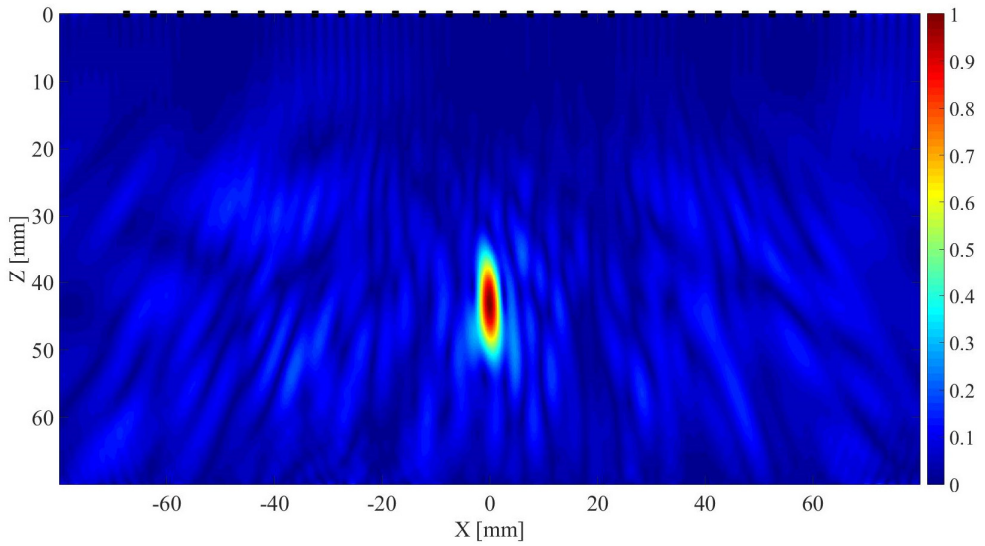

Figure 3.13. Image corresponding to the Case a) with DAS algorithm (color scale in linear).

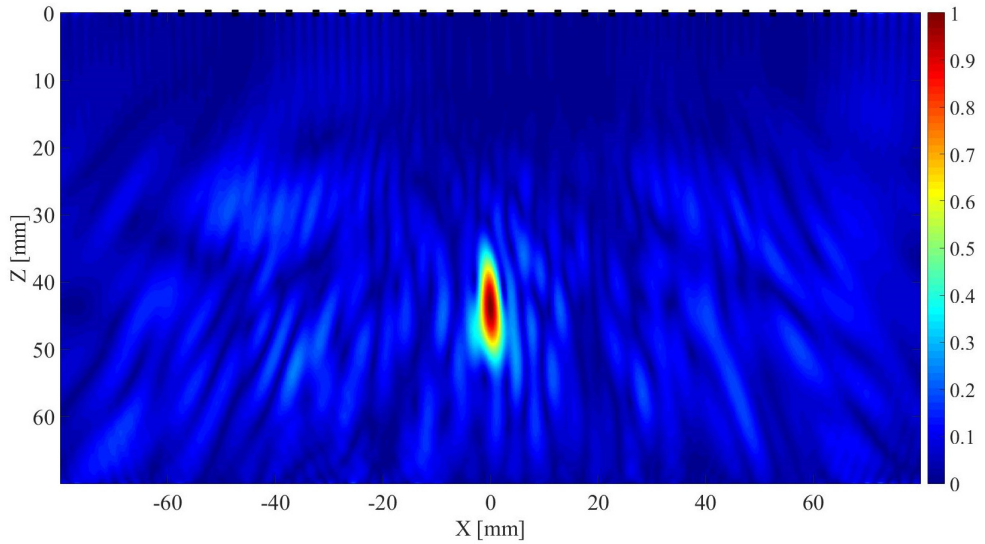

Figure 3.14. Image corresponding to the Case b) with DAS algorithm (color scale in linear).

TABLE 3.1. RESOLUTIONS OF THE SIMULATED TARGETS.

Case		Measured *range*-resolution (δ_r)	Measured *lateral*-resolution (δ_{xy}) @ 30 GHz
a	Metallic sphere in air diameter = 2mm	14 mm	3.6 mm
b	Tumor sphere in air diameter = 2mm	14 mm	3.6 mm

Theoretical δ_r =14 mm and *theoretical* δ_{xy} @ 30 GHz = 2.9 mm for a point-like emitter in air.

Test of the prototype

In this thesis, the proof-of-concept for imaging at mm-waves was done considering a linear layout based on a synthetic array with 24 antennas in 28 positions. Imaging measurements are done in the broad frequency range from 18 to 40 GHz. The spacing between the phase centres of adjacent radiators is 5 mm, corresponding to half wavelength in air at 30 GHz. The proposed prototype does not include coupling medium; therefore, in all cases, the scanning is done in air. Being these the first feasibility tests of target detection in phantom at mm-wave, the skin has not been included in these tests of the prototype. However, even if these first models were deliberately produced in simplified versions, the strong contribution of signal reflection to the skin interface was taken into account in the feasibility study of the system (the results of which are summarized above); therefore, there is room for inclusion and certainly tests on more complex phantom that include the presence of the skin will have to be done in the future. Different tests were done in order to demonstrate the target detection capability of the proposed radar system, and some results are presented in this chapter summarizing the escalation of these tests on phantoms with increasing values for attenuation. A sketch of the experimental setup for the case of measurements with phantom is shown in Figure 3.15.

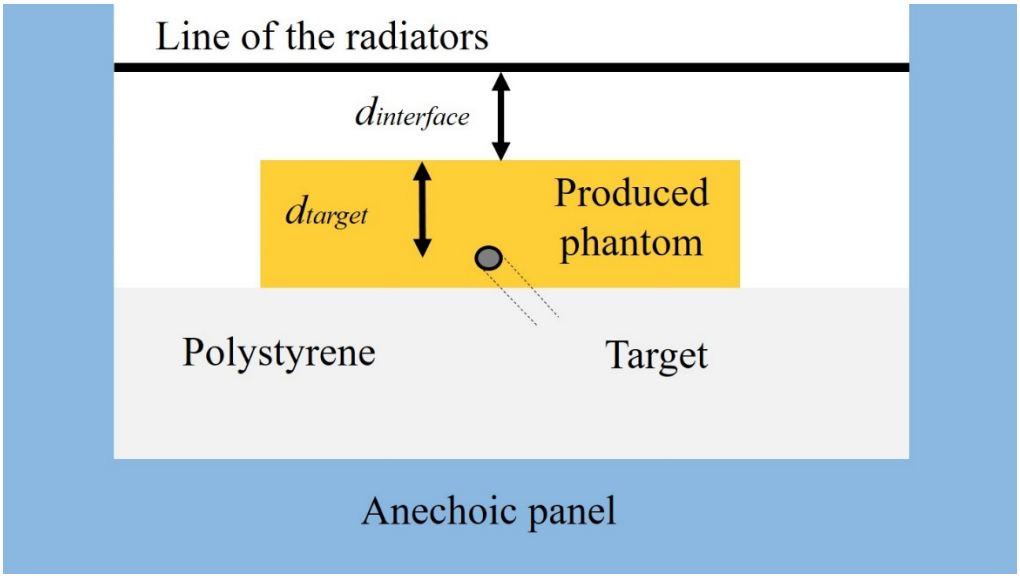

Figure 3.15. Sketch of the experimental setup for the case of measurements with phantom.

The mm-wave imaging prototype was firstly tested on a perfect microwave target, a metallic sphere, in air, with diameter of 4 mm, placed 7 cm far from the centre of the array, and with a lateral displacement of around 3 cm. In Figure 3.16, the image corresponding to this test is shown, demonstrating the reliable identification of the target position in air.

The prototype was then tested on a not-ideal target, a cylinder made by deionized water and gelatine, with diameter around 8 mm at a distance of 7 cm from the centre of the array and with a lateral displacement of around 5 mm from the center of the array, and in Figure 3.17 the corresponding radar image is shown. Also in this case, the result confirms the reliable identification of the target position by the proposed imaging system.

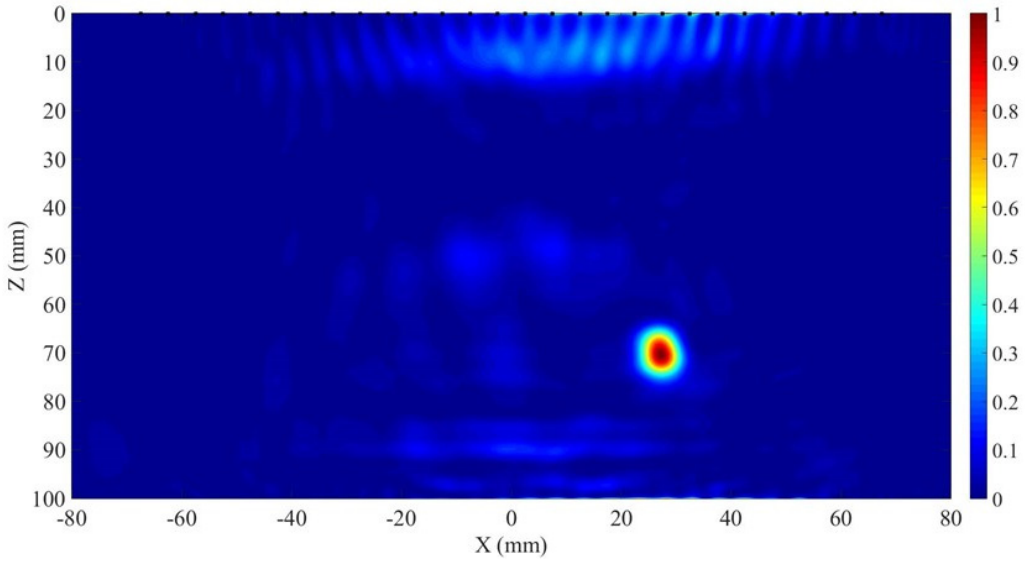

Figure 3.16. Reconstructed mm-wave image for a spherical target (diameter=4 mm) in air using a synthetic linear array with 24 antennas, far 7 cm from the center of the array and with a lateral displacement of 3 cm. Image achieved by using the DAS algorithm, and color scale in linear.

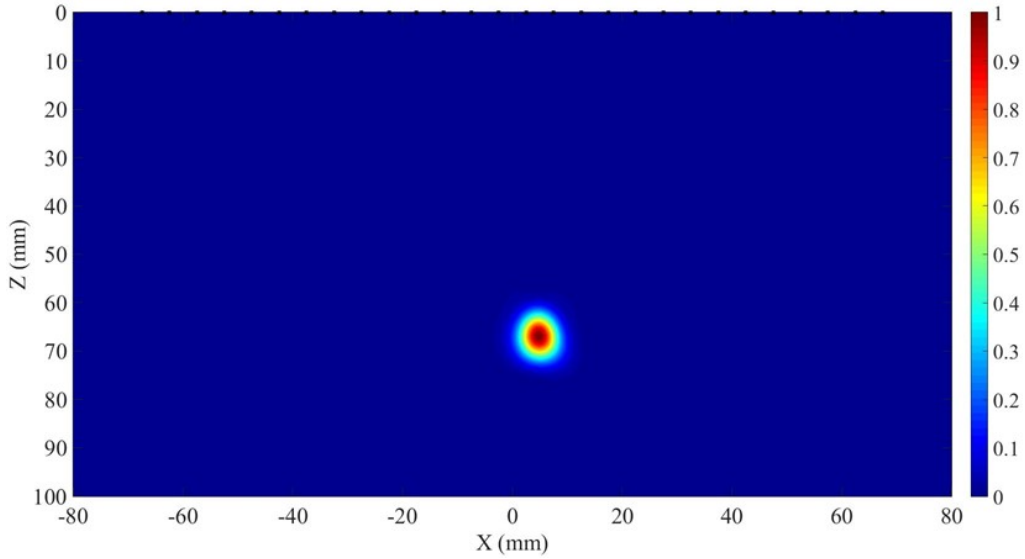

Figure 3.17. Reconstructed mm-wave image for a cylindrical tube (diameter=8 mm) made by water and gelatine in air using a synthetic linear array with 24 antennas, far 7 cm from the center of the array and with a lateral displacement of 5 mm. Image achieved by using the DAS algorithm, and color scale in linear.

A different test involving the wave propagation in a medium practically lossless at 30 GHz, instead of in air, was done considering *Phantom1* distant 3 cm from the line of the antennas, with a cylindrical tube made by deionized water and gelatine (diameter 8 mm) as target placed 1.5 cm under the surface of the phantom, off-axis of around 10 mm with respect to the centre of the array. The imaging result for this case is shown in Figure 3.18, where not only the target detection capability of the system is demonstrated, but also that the inclusion procedure (described above) works. In this case, since the wave speed is different from light speed because the medium is not air anymore, the real position of the target within the phantom is derived from the equivalence:

$$(d_{air} - d_{interface}) : c = d_{target} : v$$

where d_{air} is the equivalent distance in air (the one visible in all Figures), $d_{interface}$ is the distance of the phantom from the array, c is the light speed in vacuum, d_{target} is the target depth within the phantom and v is the wave speed within the propagation medium ($v = \frac{c}{\sqrt{\varepsilon r}}$).

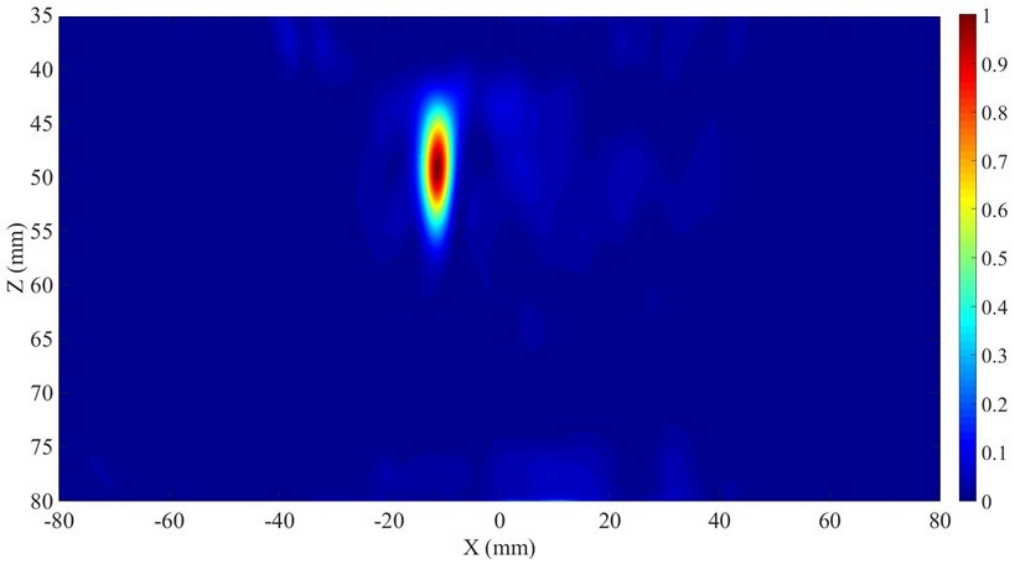

Figure 3.18. Reconstructed mm-wave image for a cylindrical tube (diameter=8 mm) made by water and gelatine in *Phantom1* using a synthetic linear array with 24 antennas. Target depth within the phantom: **1.5 cm**. The image starts from 35 mm because from this point the interface is no longer visible. Image achieved by using the DAS algorithm, and color scale in linear.

By changing the medium, assumed to have a non-null value for losses, an additional test was done considering *Phantom2* distant 5 cm from the line of the antennas, with a cylindrical tube made by deionized water and gelatine (diameter 8 mm) as target placed again 1.5 cm under the surface of the phantom, in-axis with respect to the centre of the array in order to optimize the S/N improvement (as described in the feasibility study of the system). The imaging result for this case is shown in Figure 3.19, where the target detection capability of the system is demonstrated.

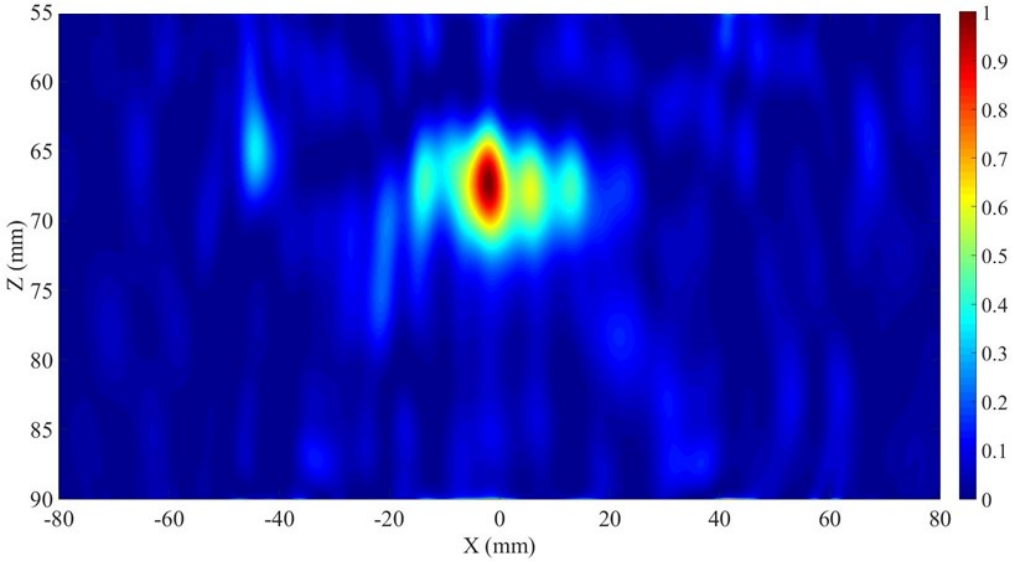

Figure 3.19. Reconstructed mm-wave image for a cylindrical tube (diameter=8 mm) made by water and gelatine in *Phantom2* using a synthetic linear array with 24 antennas. Target depth within the phantom: **1.5 cm**. The image starts from 55 mm because from this point the interface is no longer visible. Image achieved by using the DAS algorithm, and color scale in linear.

As mentioned in the description of the phantom preparation procedure, the pouring process provides unavoidable air bubbles within the phantom. To show this aspect, as an example, the image corresponding to the measurement of the only *Phantom2* (with no inclusions) is shown in Figure 3.20, where it is possible to appreciate the spurious scattering due to the air bubbles presence and its effect on the produced image.

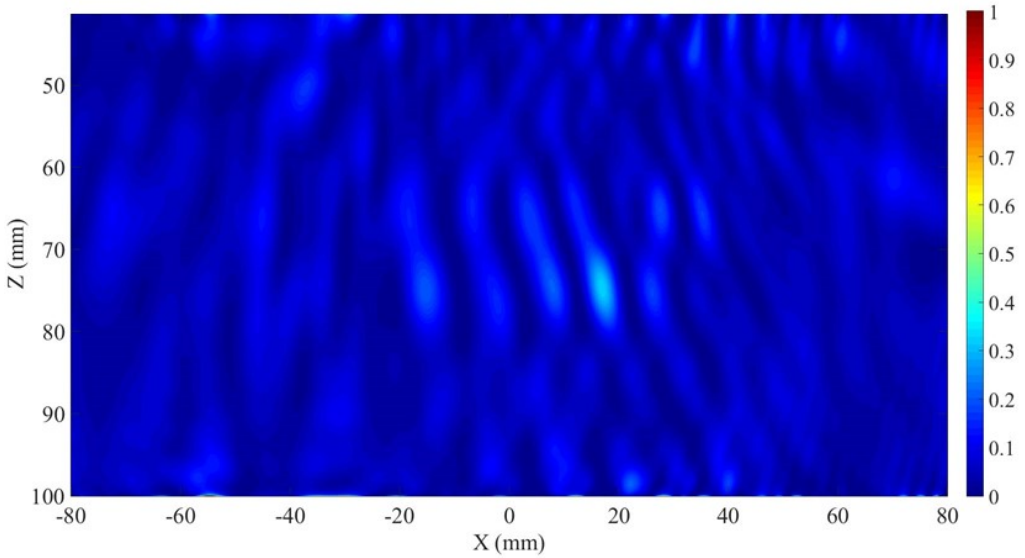

Figure 3.20. Reconstructed mm-wave image for the measurement of the *Phantom2* without inclusions using a synthetic linear array with 24 antennas. The image starts from 40 mm because from this point the interface is no longer visible. Image achieved by using the DAS algorithm, and color scale in linear.

The test of the mm-wave prototype on *Phantom2*, distant 4 cm from the array, but with a more realistic target (in shape), a currant of diameter around 8 mm, is now shown. This inclusion gives the possibility of having in the same time a target with high water content and a spherical shape (very difficult to achieve with our home-made phantom); therefore, more realistic than a cylinder made by deionized water and gelatine. The target depth was 2 cm under the surface of the phantom, in-axes with respect to the centre of the array. Also in this case, the target detection capability of the mm-wave imaging system is demonstrated (Figure 3.21).

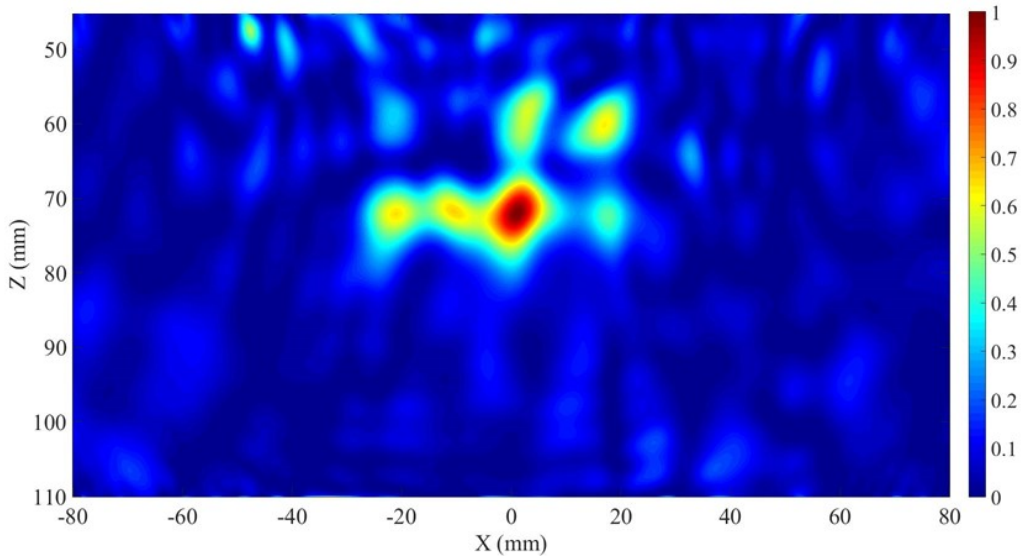

Figure 3.21. Reconstructed mm-wave image for a currant (diameter=8 mm) in *Phantom2* using a synthetic linear array with 24 antennas. Target depth within the phantom: **2 cm**. The image starts from 53 mm because from this point the interface is no longer visible. Image achieved by using the DAS algorithm, and color scale in linear.

The last test reported in this thesis was done on a phantom with high values for losses (*Phantom3* in Figure 3.8). In this case, the inclusion was done by a cylinder (diameter of 8 mm) of deionized water and agar as solidifying agent at a depth of 1.4 cm under the surface of the phantom, and almost in line with respect to the center of the array. The phantom was placed 3.5 cm from the line of the antennas, and also in this case the measurement was done in air.

Figure 3.22 shows the achieved image and the good detection capability up to 1.4 cm under the surface of a lossy phantom is demonstrated.

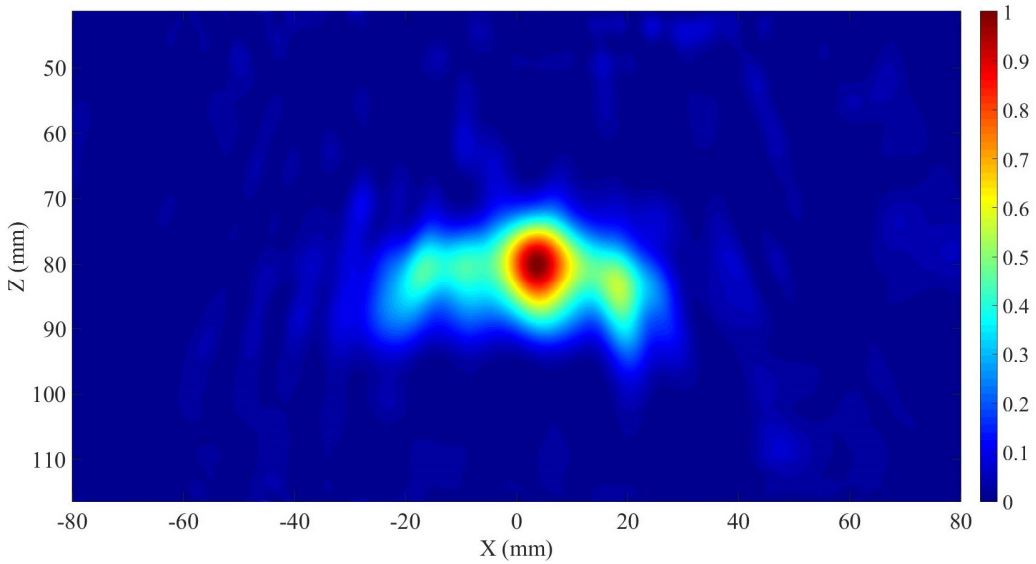

Figure 3.22. Reconstructed mm-wave image for a cylinder made by deionized water and agar (diameter=8 mm) in *Phantom3* using a synthetic linear array with 24 antennas. Target depth within the phantom: **1.4 cm**. The image starts from the point in which the interface is no longer visible. Image achieved by using the DAS algorithm, and color scale in linear.

Since the latter phantom does not represent a particularly fatty tissue, an Ultrasound scan was also possible and the corresponding image is shown in the Figure 3.23. From this image, not only is it possible to see the position of the target, but it is also proof of the fact that this type of phantom is suitable for scanning in a bi-modal approach, millimetre waves and ultrasounds based. This, therefore, represents the first significant step in the direction of having a combined imaging system, from which a significantly improved morphological reference of the malignant lesion within the scenario is expected.

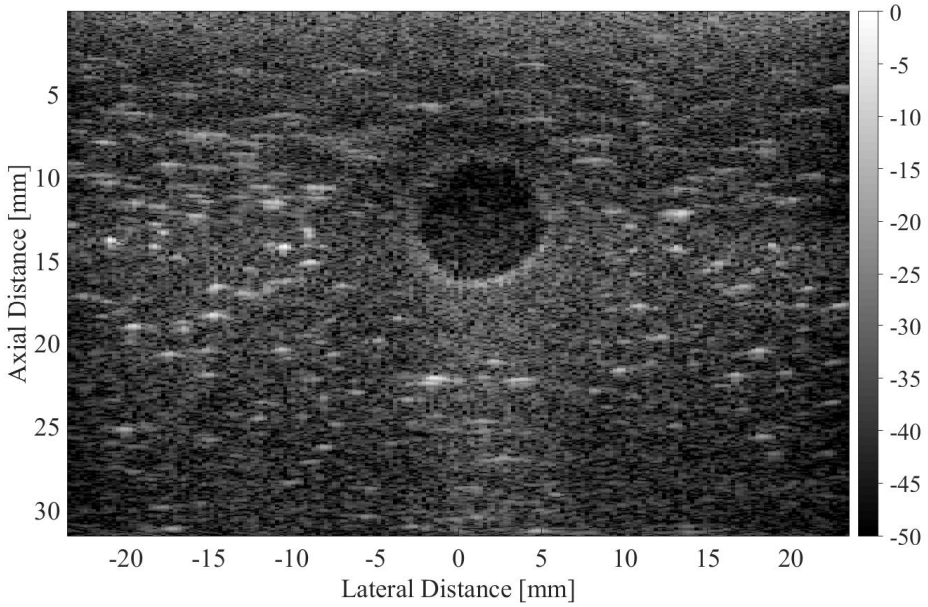

Figure 3.23. Reconstructed Ultrasound image for a cylinder made by deionized water and agar (diameter=8 mm) in *Phantom3*. Same phantom with inclusion used for Figure 3.22. Target depth within the phantom: **1.4 cm**. Color scale in dB.

Other tests on different phantoms, considering as inclusion both the metallic sphere with diameter of 4 mm and cylinder of deionized water and gelatine with diameter of 8 mm, also involving a lower or higher number of antennas were done. However, the corresponding images were not included in this thesis as do not contain additional information with respect to the results shown.

Conclusions

In this chapter, some tests of the mm-wave imaging prototype on realistic breast phantoms are presented. The proposed system is based on the multi-static radar architecture and the signal acquisition is done by means of the *Synthetic Aperture Focusing* approach. After the feasibility study of the system with central working frequency of 30 GHz, both for linear and circular layout, and the discussion about the Point Spread Function of this kind of system, the synthetic linear prototype is tested. The signal acquisition for the imaging test is driven by the VNA and the synthetic linear array is based on two double-ridge truncated waveguides, supported by four micro-step linear actuators, and connected to the VNA through two coaxial cables. For the linear scanning of the object, only two actuators are used and the distance between phase centre of adjacent radiators is half wavelength at 30 GHz in air, 5 mm. Measurements are done in the frequency range from 18 to 40 GHz. Different targets are imaged, both in air and in three kinds of phantoms with increasing values for dielectric losses (mimicking dielectric properties of *Low density* human breast *ex-vivo* tissues).

In all cases, after the calibration of the system, made by using air and a metallic plate as standard, the data are used as input of the Delay-And-Sum (DAS) algorithm for image reconstruction.

Further tests on more complex phantoms will be done in the future both in linear and conformal configuration and both in a 1-D and in 2-D layout.

CONCLUSIONS

In this thesis, the detailed study of a new millimetre wave imaging system with a central working frequency of 30 GHz for breast cancer detection was presented. The three main phases of the project were described in detail, from the dielectric characterization of biological tissues in the wide frequency range from 500 MHz to 50 GHz, to the production of realistic phantoms mimicking the dielectric properties of human breast *ex-vivo* tissues, to the test of the linear prototype of the millimetre wave imaging system on phantoms mimicking dielectric properties of fat human breast tissues.

In the *first chapter*, the three main dielectric characterization campaigns followed and carried out by the author of this thesis have been described, that are:

- The two experimental campaigns performed at the European Institute of Oncology in Milan on 342 *ex-vivo* samples of the human breast, derived from 98 women aged from 14 to 85 years, in 2014 and 2016, in the frequency range [0.5-50] GHz. The objective of these experimental campaigns was to assess whether a significant dielectric difference exists between healthy and diseased breast tissues even up to 50 GHz; before these experimental campaigns, indeed, only data measured up to no more than 20 GHz were available, while for higher frequencies the dielectric properties were only extrapolated through mathematical models from measurements at lower frequencies. The experimental data produced by the two experimental campaigns performed at the European Institute of Oncology have shown not only that the dielectric difference between different types of healthy tissues and neoplastic ones is significant up to the regime of millimeter waves, but also that about 40% of the healthy samples measured show very low dielectric permittivity values (both in terms of ε' and in terms of ε") and, therefore, with particularly significant dielectric contrast compared to neoplastic tissues (which, vice versa, have high dielectric permittivity values even at high frequencies) as well as with relatively low values for propagation losses. In addition, the correlation between the *ex-vivo* samples measured and the age of the women who produced them showed that the samples responsible for the aforementioned statistics were derived in greater numbers from women in the age group around 50 years, therefore the target for the current screening programs based on mammography, showing for these reasons the promising use of the system proposed in this thesis as a complementary technique and/or potentially substitutive to mammography, for screening applications even before diagnosis.
- The experimental campaign on *ex-vivo* samples derived both from homogeneous (liver and kidney cortex) and from heterogeneous (lungs) organs of animals and humans, in the frequency range [0.5-50] GHz performed in collaboration with the University of Malta and the *Mater Dei* Hospital of Malta. The aim of this work was to investigate the origin of the significant dielectric differences between the results produced by the different research groups also in relation to the same organ, as well as the quantification of any possible dielectric difference between organs derived from humans and those derived from animals. In particular, after the proposal of an attempt to standardize the measurement protocol aimed to the preservation of the sample hydration level, the sample water content was investigated as a possible classifier (among other derived quantities) for *intra-* and *inter*-organ/animal variability, both for homogeneous tissues and for heterogeneous ones. Three independent measurements were made for each sample and the percentage variation coefficient (i.e., the percentage ratio between the standard deviation and the mean) between these three measurements was related to the water content of the sample itself. The results showed that, for homogeneous tissues, a higher water content of the sample is responsible for a lower variability between measurements made on the sample

itself for all types of animals and for samples derived from the human being; therefore, in future experimental campaigns, an assessment of the variability of dielectric measurements on the same sample could give an indication of the water content of the sample itself. For heterogeneous tissues, however, the analysis of the correlation of the sample hydration level and the variability of its dielectric properties showed that, due to the high standard deviation values, other classifiers (such as sample density) are needed for the dielectric measurement data. It will be interesting, in the future, to re-apply this methodology on homogeneous samples with a higher percentage of adipose tissue (therefore, lower percentage of water), as well as, as regards heterogeneous tissues, to an in-depth analysis of the cross correlation between the level of hydration of the sample, its density and the variability in its dielectric properties. On the other hand, the analysis of the comparison between the dielectric properties of samples derived from animals and those derived from humans has shown that there are no particularly significant dielectric differences between these two categories and it would be desirable, in the future, to validate these preliminary results on a database involving more human subjects.

- the *in-vivo* experimental campaign on the small colony of mice at the IFOM institute in Milan, in preparation for the largest campaign of measurements that will be made in the coming months, in the frequency range [0.5-50] GHz, in collaboration with the European Institute of Oncology in Milan. In this case, the measurements were made on *in-vivo*, *in-loco* up to 20 minutes after the mouse's death and in some cases *ex-vivo* tumours, with and (when possible) without skin. The final objective of this measurement campaign is the comparison between the dielectric properties measured on *ex-vivo* samples and those measured on *in-vivo* samples to evaluate and quantify the possible impact of blood flow, as well as body temperature, on the dielectric properties measured. This work will be useful to validate the extensive database derived by the two experimental campaigns on human breast *ex-vivo* samples, also based on the results of the previous section about the non-significant variability of dielectric properties of animal and human organs. In particular, it will be interesting to carry out the comparison also considering fatty samples (maybe even derived from different animals) and avoiding in all cases the presence of the skin.

In the *second chapter* of this thesis, several recipes were proposed for the preparation of realistic breast phantoms capable of mimicking the dielectric properties of *ex-vivo* breast tissues up to 50 GHz, as these are fundamental to test the proposed mm-wave imaging prototype. In particular, two macro-categories of phantom have been proposed: one based on the use of gelatine as a solidifying agent and on dishwashing liquid as a surfactant to mimic the average dielectric properties of the three categories of healthy breast tissues (*Low*-, *Medium*- and *High- density* tissues, basing on the percentage adipose content) and neoplastic ones, and one on the use of waste-oil hardener as a solidifying agent and Polysorbate 80 as a surfactant to mimic the dielectric properties of particularly fatty healthy tissues (target of the imaging system with millimetric waves, thanks to the favourable low values of dielectric losses). In both cases, low-cost, safe, easy-to-handle and retrievable materials were used. Mixtures in the first category were produced using oil, deionized water, gelatine and dishwashing liquid, and the average dielectric properties of all the four categories of breast tissues (three healthy and malignant) were mimicked by changing the percentages of oil in the mixtures. For this category of phantom, also a preliminary study of the mechanical properties of phantom mimicking the dielectric properties of neoplastic tissues has been done in collaboration with the Department of Civil Engineering and Architecture of the University of Pavia, since they are anatomically more rigid than the surrounding healthy tissues, and the good results obtained (in line with Young's Module values in the literature), although they need a validation on a larger number of samples, could be useful for using this kind of phantom also for other applications (for example, microwave elastography). In addition, the good capability of sunflower oil to preserve the dielectric properties of phantom up to 10 days after its preparation has been demonstrated. The

mixtures belonging to the second category, on the other hand, were born from the need to mimic the dielectric properties of particularly fatty human breast tissues (corresponding to 40% of the healthy samples measured in the two experimental campaigns of 2014 and 2016), which, requiring a lower percentage of water volume, compromise the ability of gelatine to solidify the whole phantom. Therefore, mixtures based on the use of waste-oil hardener instead of gelatine have been proposed and, to limit the presence of air bubbles in phantoms of this type, two different surfactants have been used, Polysorbate 80 and lecithin. In both cases, these are safe and low-cost materials. The new recipes, therefore, were based on low volume percentages of deionised water, sunflower oil, waste-oil hardener and Polysorbate 80 or lecithin. In addition, since waste-oil hardener dissolves in oil as much as in Polysorbate 80, simpler phantoms based on the use of only these two components have been produced and characterized in the frequency range [0.5-50] GHz. The dielectric properties of all the produced phantoms were compared with those of the human breast *ex-vivo* tissues measured in 2014 and 2016 at the European Institute of Oncology in Milan. In this chapter, a first example of hemispheric phantom mimicking the dielectric properties of healthy tissues with an inclusion mimicking the dielectric properties of neoplastic tissues was also shown. This phantom, although not perfect, represented the first case of heterogeneous phantom and marked the first step in the direction of creating increasingly realistic phantoms with appropriate inclusions to test the prototype of a millimeter wave imaging system. Phantoms with improved inclusions, as well as with different types of healthy tissue, are desirable for the future.

In the *third* and final *chapter* of the thesis, the test of the linear prototype of the millimeter wave system for the detection of different types of targets was shown. In particular, after a summary of the feasibility study of the millimeter wave imaging system for the diagnosis of breast cancer both for linear and circular configuration, as well as some discussion about the Point Spread Function of a system of this kind, in this chapter, the results of radar imaging were shown on two targets in air, metal sphere and cylinder of water and gelatine, and on three targets (cylinder of water and gelatine, cylinder of water and agar, and currant) included in three different phantoms with increasing values for dielectric losses, deep up to 2 cm below the surface of the phantom. The proposed prototype is based on the multi-static radar architecture and the signal processing is done following the *Synthetic Aperture Focusing* approach. The experimental setup for this type of test included two double-ridge truncated waveguides, mounted on four interconnected linear translators, and connected via two coaxial cables to the VNA. The synthetic array was composed by 24 antennas in 28 positions, with spacing between phase centers of adjacent radiators equal to half wavelength in air at 30 GHz, 5mm. The system did not involve the use of a coupling medium. The mono-modal working bandwidth of the two antennas ranges from 18 to 40 GHz, with a TE10 mode cut-off frequency of 15 GHz. The proposed prototype worked with only the transmitted signals and for each pair of antennas the amplitude and phase of the S21 were measured. The matrix corresponding to the entire array was then formed and calibrated before being used as input in the image reconstruction algorithms. In particular, the complete calibration of the system involved the use of two standards, the air and the metal plate, while the algorithm used for data processing and image creation was the Delay-And-Sum and was provided by the Bioengineering Laboratory of the University of Pavia. The results showed that the system is able to correctly identify the position of the target in both scenarios, in air and in phantom. This chapter represented the proof-of-concept of the feasibility of the imaging system with central working frequency of 30 GHz for the detection of breast cancer. Now, with the awareness that millimetre wave imaging in *Low density* tissues is possible, many margins for improvement can be explored. The transition from linear to planar acquisition, with the consequent passage from two-dimensional to three-dimensional images and, therefore, a significant increase in the morphological reference of the malignant lesion in the illuminated scenario; the passage from linear/planar configurations to conformal configurations, which in theory would allow to reach greater depths with better resolutions; the utilization of better image processing algorithms; the testing of the prototype on increasingly realistic phantoms, possibly

including skin, as well as the development of procedures to eliminate the strong contribution of the air/skin interface, are only some of the future steps that would be desirable.

In conclusion, therefore, the road to be taken before seeing the insertion of a system of this type in clinical practice (also involving combined modalities) is still very long; however, in this thesis, the feasibility of this system for applications of screening and possibly diagnosis for breast cancer in women whose breasts lend themselves to scanning with mammography is demonstrated in many respects, strongly encouraging further analysis in this direction.

REFERENCES

Agilent 85070E Dielectric Probe Kit 200 MHz to 50 GHz. Available: http://literature.cdn.keysight.com/litweb/pdf/5989-0222EN.pdf

Ahmed S S, Genghammer A, Schiessl A, and Schmidt L P, 2013 Fully electronic E-band personnel imager of 2 m² aperture based on a multistatic architecture *IEEE Trans. Microw. Theory Techn.* **61** 651-657.

Ahmed S S, Schiessl A, and Schmidt L P, 2011 A Novel Fully Electronic Active Real-Time Imager Based on a Planar Multistatic Sparse Array *IEEE Trans. Microw. Theory Techn.* **59** 3567-3576.

Alanen E, Lahtinen T, Nuutinen J 1999 Penetration of electromagnetic fields of an open-ended coaxial probe between 1 Mhz and 1 Ghz in dielectric skin measurements *Phys. Med. Boil.* **44** N169–N176.

Alekseev S I, Szabo I, and Ziskin M C 2008 Millimeter wave reflectivity used for measurement of skin hydration with different moisturizers *Skin Res Technol* **14** 390-396.

Alekseev S I, Ziskin M C 2007 Human skin permittivity determined by millimetre wave reflection measurements *Bioelectromagnetics* **28** 331-339.

Alsheheri S, *et al.*, 2011 A UWB Imaging System to Detect Early Breast Cancer in Heterogeneous Breast Phantom *International Conference on Electrical, Control and Computer Engineering*, Pahang, Malaysia.

Amineh RK, McCombe JJ, Khalatpour A, Nikolova NK 2015 Microwave Holography Using Point-Spread Functions Measured With Calibration Objects *IEEE Transactions on Instrumentation and Measurements*, **64**, pp. 403 - 417.

Antes J and Kallfass I 2013 Performance estimation for broadband multigigabit millimeter- and sub-millimeter-wave wireless communication links *IEEE Trans. Microw. Theory Techn.* **63** 3288-3299.

Bahramiabarghouei H, *et al.*, 2015 Flexible 16 antenna array for microwave breast cancer detection *IEEE Trans. Biomed. Eng.* **62** 2516–525.

Balanis C. A., *Antenna Theory: Analysis and Design*, Wiley-Interscience, New Jersey, 2005.

Balanis C. A., *Advanced Engineering Electromagnetics*, John Wiley and Sons, New York, 1989.

Bakar A A, Abbosh A and Bialkowski M 2011 Fabrication and characterization of a heterogeneous breast phantom for testing an ultrawideband microwave imaging system *Proc. Asia-Pacific Microwave Conf. 2011 (Melbourne, Australia)* pp 1414-7.

Barrett A H and Myers P C 1975 Subcutaneous temperature: a method of noninvasive sensing *Science* **190** 669-671.

Barrett A H, Myers P C, and Sadowsky N L 1977 Detection of breast cancer by microwave radiometry *Radiol. Sci.* **12** 167–171.

Beard P 2011 Biomedical photoacoustic imaging *Interface Focus* **1** 602–631.

Bigu del Blanco J and Romero-Sierra C 1974 Microwave radiometric techniques: A means to explore the possibility of communication in biological systems *6th Annual Meet., Neuro-Electric Soc. Symp. Effects of Low-Frequency Magnetic and Electric Fields on Biological Communication Processes* (Snowmass-at-Aspen, CO, Feb. 1973).

Bond E J, Li X, Hagness S C, Van Veen B D 2003 Microwave Imaging via Space-Time Beamforming for Early Detection of Breast Cancer *IEEE Trans. Ant. and Prop.* **51** 1690-1705.

Bonello, J., *et al.*, 2018. An investigation of the variation of dielectric properties of ovine lung tissue with temperature *Biomedical Physics & Engineering Express* **5** 045024.

Broquetas A *et al.* 1991 Cylindrical geometry: A further step in active microwave tomography," *IEEE Trans. Microw. Theory Tech.* **39** 836-844.

Brovoll S *et al.* 2013 Time-lapse imaging of human heartbeats using UWB radar *IEEE Biomed. Circuits Syst. Conf.* pp. 142-145.

Bruggeman D A G 1935 Berechnung verschiedener physikalischer Konstanten von heterogenen Substanzen. I. Dielektrizitätskonstanten und Leitfähigkeiten der Mischkörper aus isotropen Substanzen *Ann. Phys.* **416** 636–64.

Burfeindt M J, Colgan T J, Mays R O, Shea J D, Behda N, Van Veen B D and Hagness S C 2012 MRI-derived 3-d-printed breast phantom for microwave breast imaging validation *IEEE Antennas Wireless Propag. Lett.* **11** 1610-3.

Burfeindt MJ, Shea JD, Van Veen BD and Hagness SC 2009 Beamforming-enhanced inverse scattering for microwave breast imaging *IEEE Trans. Antennas Propag.* **62** 5126–5132.

Caratelli D, Lay-Ekuakille A, Vergallo P 2013 Non-invasive reflectometry-based detection of melanoma by piezoelectric micro-needle antenna sensors *Progress Electromagn. Res.* **135** 91-103.

Carr K L 1989 Microwave radiometry: Its importance to the detection of cancer *IEEE Trans. Microwave Theory Tech.* **37** 1862–1869.

Cole K. – Cole R. 1941 Dispersion and absorption in dielectrics I. Alternating current characteristics *J. Chem. Phys.* 9 341351.

Colton D and Monk P 1995 The detection and monitoring of leukemia using electromagnetic waves: Numerical analysis *Inverse Prob.* **11** 329-341.

Converse MC, Bond EJ, Hagness SC and Van Veen BD 2004 Ultrawideband microwave space-time beamforming for hyperthermia treatment of breast cancer: a computational feasibility study *IEEE Trans. Microw. Theory Tech.* **52** 1876–89.

Di Meo S, *et al.*, 2017a On the Feasibility of Breast Cancer Imaging Systems at Millimeter-Waves Frequencies *IEEE Trans. Microw. Theory Techn.* **65** 1795-806.

Di Meo S, *et al.*, 2017b Experimental validation of the dielectric permittivity of breast cancer tissues up to 50 GHz *Proc. IEEE MTT-S Int. Microwave Workshop Series Advanced Materials and Processes (Pavia, Italy)* pp 1–3.

Di Meo S, *et al.*, 2017c High-Resolution mm-Wave Imaging Techniques and Systems for Breast Cancer Detection *IEEE MTT-S International Microwave Workshop Series-Advanced Materials and Processes (IMWS-AMP 2017) (Pavia, Italy)*.

Di Meo S, *et al.*, 2018a Dielectric properties of breast tissues: experimental results up to 50 GHz *Proc. 2018 12th European Conf. On Antennas Propagation (EuCAP 2018) (London, UK)* pp 1–5.

Di Meo S, *et al*., 2018b Correlation Between Dielectric Properties and Women Age for Breast Cancer Detection at 30 GHz *IEEE International Microwave Biomedical Conference (IMBioC)*, Philadelphia, USA.

Di Meo S, Pasotti L, Pasian M and Matrone G 2018c On the conservation of materials for breast phantoms in the frequency range 0.5–50 GHz *Proc. 48th European Microwave Conf. 2018 (Madrid, Spain)* pp 320–3.

Di Meo S, *et al.*, 2018d Preliminary Experimental Characterization of Gelatine-Based Tissue-Mimicking Materials for Realistic Breast Phantoms aimed at Microwave Applications, *1st EMF-Med World Conference on Biomedical Applications of Electromagnetic Fields*, Split, 10-13 September 2018.

Di Meo S, *et al.*, 2019a Tissue-mimicking materials for breast phantoms up to 50 GHz *Phys. Med. Biol.* https://doi.org/10.1088/1361-6560/aafeec.

Di Meo S, *et al.*, 2019b Tissue mimicking materials for breast phantoms using waste oil hardeners, *13th European Conference on Antennas and Propagation* (*EuCAP 2019*), Krakow, Poland, March 31-April 5, 2019.

Enander B and Larson G 1974 Microwave radiometric measurements of the temperature inside the body *Electron. Lett.* **10** 317.

Espin Lopez P F, *et al.*, 2016 Breast cancer imaging at mm-Waves: feasibility study on the safety exposure limits," *46th European Microwave Conference (EuMC2016)*, London, UK, October 3–7.

Farrugia L, Wismayer PS, Mangion LZ and Sammut CV 2016 Accurate in vivo dielectric properties of liver from 500 MHz to 40 GHz and their correlation to ex vivo measurements *Electromagn Biol Med* **35** 365-73.

Fear E C, *et al.*, 2013 Microwave breast imaging with a monostatic radarbased system: A study of application to patients *IEEE Trans. Microw. Theory Techn.* **61**, pp. 2119–2128.

Fear E C, Li X, Hagness S C, Stuchly M A 2002 Confocal Microwave Imaging for Breast Cancer Detection: Localization of Tumors in Three Dimensions *IEEE Trans. Biomed. Eng.* **49** 812-822.

Fleming W J 2015 Forty-year review of automotive electronics *IEEE Veh. Technol. Mag.* **10** 80-90.

Gabriel S, Lau RW and Gabriel C 1996b The dielectric properties of biological tissues: II. Measurements in the frequency range 10 Hz to 20 GHz *Phys. Med. Biol.* **41** 2251–69.

Gabriel C, Gabriel S and Corthout E 1996a The dielectric properties of biological tissues: I. Literature survey *Phys. Med. Biol.* **41** 2231–49.

Gabriel C and Peyman A 2006 Dielectric measurement: error analysis and assessment of uncertainty Phys. Med. Biol. **51** 6033-46.

Garrett J and Fear E 2015 A new breast phantom with a durable skin layer for microwave breast imaging *IEEE Trans. Antennas Propag.* **63** 1693-700.

Ghaaliq Lalkhen A, *et al* 2008 Clinical tests: sensitivity and specificity, *Continuing Education in Anaesthesia Critical Care & Pain*, Volume 8, Issue 6, December 2008, Pages 221–223.

Grzegorczyk TM, *et al.*, 2012 Fast 3-D tomographic microwave imaging for breast cancer detection *IEEE Trans. Med. Imag.* **31** 1584–92.

Hadipour K, *et al.*, 2015 A 40GHz to 67GHz bandwidth 23dB gain 5.8dB maximum NF mm-wave LNA in 28nm CMOS *2015 IEEE Radio Frequency Integrated Circuits Symposium (RFIC)*, Phoenix, Arizona, U.S.A., May 17 – 22.

Hahn C and Noghanian S 2012 Heterogeneous breast phantom development for microwave imaging using regression models *Int. J. Biomed. Imaging* **2012** 803607.

Hayashi Y, Miura N, Shinyashiki N, Yagihara S 2005 Free water content and monitoring of healing processes of skin burns studied by microwave dielectric spectroscopy in vivo *Phys. Med. Biol.* **50** 599.

Haslam N C, Gillespie A R, and Haslam C G T 1984 Aperture synthesis thermography—A new approach to passive microwave temperature measurements in the body *IEEE Trans. Microwave Theory Tech.* **32** 829–835.

Hater R J *et al.*, 2009 The correlation of in vivo and ex vivo tissue dielectric properties to validate electromagnetic breast imaging: initial clinical experience *Physiol Meas.* **30** S121-36.

Heijblom M *et al.* 2012 Imaging breast lesions using the Twente Photoacoustic Mammoscope: ongoing clinical experience *Photons Plus Ultrasound: Imaging and Sensing* (San Francisco, USA, January 22-24, 2012).

Henderson R P, Webster J G 1978 An impedance camera for specific measurements of the thorax *IEEE Trans. Biomed. Eng.* **BME-25** 250-254.

Henin B, Abbosh A M and Abdulla W A 2015 Electro-biomechanical breast phantom for hybrid breast imaging *Proc. 2015 Int. Symp. On Antennas and Propagation (ISAP) (Hobart, Tasmania, Australia)* pp 1-3.

Henriksson T, *et al.* 2011 Clinical trials of a multistatic UWB radar for breast imaging *2011 Loughborough Antennas & Propagation Conference*, Loughborough, UK, Nov. 14-15.

Hofmann M, Fischer G, Weigel R, Kissinger D 2013 Microwave-based non-invasive concentration measurements for biomedical applications *IEEE Trans. Microwave Theory Tech.* **61** 2195-2204.

IEEE Standard for Radar Definitions, IEEE Std 686™-2017 (Revision of IEEE Std 686-2008).

Jacobi J H, Larson L E, and Hast C T 1979 Water-immersed microwave antennas and their application to microwave interrogation of biological targets *IEEE Trans. Microwave Theory Tech.* **MIT-27** 70-78.

Janssen N and Smulders P 2012 Design of millimeter-wave probe for diagnosis of human skin *Proc. 42nd European Microwave Conf.* (Amsterdam, Netherlands, 29 Oct.-1 Nov.) pp. 440-443.

Jean B, Green E, McClung M 2008 A microwave frequency sensor for non-invasive blood-glucose measurement *Proc. IEEE Sensors Applications Symp.* (Atlanta, GA, USA, 12-14 Feb.), pp. 4-7.

Joachimowicz N, Conessa C, Henrikkson T and Duchene B 2014 Breast phantoms for microwave imaging *IEEE Antennas Wireless Propag. Lett.* **13** 1333-6.

Joachimowicz N, Duchene B, Conessa C and Meyer O 2016 Easy-to-produce adjustable realistic breast phantoms for microwave imaging *10th European Conference on Antennas and Propagation (EuCAP)* 1-4.

Klemm M, Craddock IJ, Leendertz JA, Preece A and Benjamin R 2009 Radar-based breast cancer detection using a hemispherical antenna array—Experimental results *IEEE Trans. Antennas Propag.* **57** 1692–1704.

Klemm M, *et al.* 2010 Clinical trials of a UWB imaging radar for breast cancer *Proceedings of the Fourth European Conference on Antennas and Propagation*, Barcelona, Spain, April 12-16.

Klemm M, Craddock I J and Preece A W 2012 Contrast-enhanced breast cancer detection using dynamic microwave imaging *2012 IEEE Antennas and Propagation Society International Symposium*, Chicago, U.S.A., July 8–14.

Kolin A 1936 Electromagnetic flowmeter: principle of method and its application to blood flow measurements *Proc. Soc. Experiment. Biol. Med.* **35** 53-56.

Króll D, Lorenc A, Świcęiński R 2015 Detecting laterality and nasality in speech with the use of a multi-channel record *IEEE International Conference on Acoustics, Speech and Signal Processing* (*ICASSP*), Brisbane, Queensland, April 19-24.

Kuwahara Y 2017 Microwave imaging for early breast cancer detection in *New Perspectives in Breast Imaging*, A. M. Malik, Ed. Rijeka, Croatia: InTech.

Lambert R K and Gremels H 1926 On the factors concerned in the production of pulmunary edema *J. Physiol.* (London) **61** 98-112.

Land D V 1987 A clinical microwave thermography system *IEEE Proc. A: Phys. Sci., Meas. Instrument., Manage. Educ. Rev.* **134** 193–200.

Larsen L E and Jacobi J H 1986 Medical Application of Microwave Imaging New York, NY, USA: IEEE Press.

Lazebnik M, Madsen E L, Frank G R and Hagness S C 2005, Tissue-mimicking phantom materials for narrowband and ultrawideband microwave applications *Phys. Med. Biol.* **50** 4245-58.

Lazebnik M, Converse MC, Booske JH and Hagness SC 2006 Ultrawideband temperature-dependent dielectric properties of animal liver tissue in the microwave frequency range *Phys. Med. Biol.* **51** 1941-55.

Lazebnik M, *et al.*, 2007a A large-scale study of the ultrawideband microwave dielectric properties of normal breast tissue obtained from reduction surgeries *Phys. Med. Biol.* **52** 2637–56.

Lazebnik M, *et al.*, 2007b A large-scale study of the ultrawideband microwave dielectric properties of normal, benign and malignant breast tissues obtained from cancer surgeries *Phys. Med. Biol.* **52** 6093–115.

Li X and Hagness S C 2001 A confocal microwave imaging algorithm for breast cancer detection *IEEE Microw. Wireless Compon. Lett.* **11** 130-132.

Li X, *et al.*, 2004 Microwave imaging via space-time beamforming: Experimental investigation of tumor detection in multilayer breast phantoms *IEEE Trans. Microw. Theory Tech.* **52** 1856-1865.

Lim H B, *et al.*, 2008 Confocal microwave imaging for breast cancer detection: Delay-multiply-and-sum image reconstruction algorithm *IEEE Trans. Biomed. Eng.* **55** 1697-1704.

Lin J C 1975 Non-invasive microwave measurement of respiration *Proc. IEEE* (Lett) **63** 1530.

Lin J C and Clarke M J 1982 Microwave imaging of cerebral edema *Proc. IEEE* **70** 523-524.

Lyte R J and Dines K A 1978 An impedance camera: a system for determining the spatial variation of electrical conductivity *Lawrence Livermore Lab.* (Livermore, CA), UCRL-52413.

Madsen E L, Hobson M A, Shi H, Varghese T and Frank G R 2005 Tissue-mimicking agar/gelatine materials for use in heterogeneous elastography phantoms *Phys. Med. Biol.* **50** 5597-618.

Madsen E L, Hobson M A, Shi H, Varghese T and Frank G R 2006 Stability of heterogeneous elastography phantoms made from oil dispersions in aqueous gels *Ultrasound Med. Biol.* **32** 261-70.

Madsen E L, Zagzebski J A and Frank G R 1982 Oil-in-gelatine dispersions for use ad ultrasonically tissue-mimicking materials *Ultrasound Med. Biol.* **8** 277-87.

Martellosio A, *et al.*, 2017 Dielectric properties characterization from 0.5 to 50 GHz of breast cancer tissues *IEEE Trans. Microw. Theory Techn.* **65** 998-1011.

Martellosio A, *et al.*, 2015 0.5–50 GHz dielectric characterization of breast cancer tissues *IET Electron. Lett.* **51** 974–5.

Mashal A, Gao F and Hagness S C 2011 Heterogeneous anthropomorphic phantoms with realistic dielectric properties for microwave breast imaging experiments *Microw. Opt. Technol. Lett.* **53** 1896-902.

Matrone G, Savoia A S, Caliano G, and Magenes G 2015 The delay multiply and sum beamforming algorithm in ultrasound B-mode medical imaging *IEEE Trans. Med. Imag.*, **34**, pp. 940–949.

Meaney P M *et al.*, 2012 Clinical microwave tomographic imaging of the calcaneous: A first-in-human case study of two subjects *IEEE Trans. Biomed. Eng.* **59** 3304-3313.

Meaney P M, *et al.*, 2000 A Clinical Prototype for Active Microwave Imaging of the Breast *IEEE Transactions on Microwave Theory and Techniques* **48**, pp. 1841-1853.

Mehta P, Chand K, Narayanswamy D, Beetner D, Zoughi R, Stoecker W 2006 Microwave reflectometry as a novel diagnostic tool for detection of skin cancers *IEEE Trans. Instrum. Meas.* **55** 1309-1316.

Moll J, *et al.*, 2017 Quality control of carbon-rubber tissue phantoms: Comparative MRI, CT, X-ray and UWB microwave measurements *11th European Conference on Antennas and Propagation (EuCAP)* 2723-7.

Moscato S, *et al.* 2013 A mm-Wave 2D ultra-wideband imaging radar for breast cancer detection *Int. J. Antennas Propag.* **2013**.

Nilavalan R, *et al.* 2005 Breast tumor detection using a flat 16 element array, *Sematic Scholar*.

Nikolova N K 2011 Microwave imaging for breast cancer *IEEE Microwave Magazine* **12** 78–94.

Nuutinen J, Ikäheimo R, Lahtinen T 2004 Validation of a new dielectric device to assess changes of tissue water in skin and subcutaneous fat *Physiol. Meas.* **25** 447-454.

Oliveira B L, *et al.*, 2015 Combined Breast Microwave Imaging and Diagnosis System *Proceedings of Progress In Electromagnetics Research Symposium* 1 274-8.

Oliveira B L, *et al.*, 2016 Development of clinically informed 3-D tumor models for microwave imaging applications *IEEE Antennas Wireless Propagation Lett.* **15** 520-3.

Oliveira B L, *et al.*, 2018 Microwave Breast Imaging: experimental tumour phantoms for the evaluation of new breast cancer diagnosis systems **4** 025036.

Persico R, 2014, Introduction to Ground Penetrating Radar: Inverse Scattering and Data Processing, *IEEE*, *IEEE Press Series on Electroma*.

Pichot C *et al.* 1985 Active microwave imaging of inhomogeneous bodies *IEEE Trans. Antennas Propag.* **33** 416-425.

Pickwell E, *et al.*, 2005 Simulating the response of terahertz radiation to basal cell carcinoma using ex vivo spectroscopy measurements *J. Biomed. Opt.* **10** 064021-064027.

Porter R A and Miller H H 1978 Microwave radiometric detection and location of breast cancer in *Proc. IEEE Electro/78*, Session 30 (Boston, MA, May 23-25).

Porter E, La Gioia A, Elahi MA, O'Halloran M 2017 Significance of heterogeneities in accurate dielectric measurements of biological tissues *XXXIInd General Assembly and Scientific Symposium of the International Union of Radio Science* (Montreal, QC, Canada, Aug. 19-26).

Pollacco DA, Farina L, Wismayer PS, Farrugia L and Sammut CV 2018 Characterization of the dielectric properties of biological tissues and their correlation to tissue hydration *IEEE Transactions on Dielectrics and Electrical Insulation* **25** 2191-2197.

Porter E, La Gioia A, Salahuddin S, Decker S, Shahzad A and Elahi MA 2018 Minimum information for dielectric measurements of biological tissues (MINDER): A framework for repeatable and reusable data *International Journal of RF and Microwave Computer-Aided Engineering* **28**.

Porter E, Fakhoury J, Oprisor R, Coates M and Popovic M 2010 Improved tissue phantoms for experimental validation of microwave breast cancer detection *4th European Conference on Antennas and Propagation (EuCAP)* 1-5.

Porter E, Coates M, Popovic M 2016a An Early Clinical Study of Time-Domain Microwave Radar for Breast Health Monitoring *IEEE Trans. Biomed. Eng.*, **63**, pp. 530-9.

Porter E, *et al.* 2016b A Wearable Microwave Antenna Array for Time-Domain Breast Tumor Screening *IEEE Trans. On Medical Imaging* **35**, pp. 1501 - 1509.

Report "Bridging mmWave Biophysics, Safety and Imaging" Prepared for Istituto Europeo di Oncologia by Università degli Studi di Pavia – Laboratorio di Microonde, October 2014.

Romeo S, *et al.*, 2011 Dielectric characterization study of liquid-based materials for mimicking breast tissues *Microw. Opt. Technol. Lett.* **53** 1276-80.

Rosen A, Stuchly MA and Vander Vorst A 2002 Applications of RF/microwaves in medicine *IEEE Trans. Microw. Theory Tech.* **50** 963–74.

Said M S M and Seman N 2017 Preservation of gelatine-based phantom material using vinegar and its life-span study for application in microwave imaging IEEE Trans. Dielectr. Electr. Insul. 24 528-34.

Santorelli A, Laforest O, Porter E and Popovic M 2015 Image classification for a time-domain microwave radar system: Experiments with stable modular breast phantoms *9th European Conference on Antennas and Propagation (EuCAP)* 1-5.

Sarvazyan A, Skovoroda A R, Emelianov S and Fowlkes J B 1995 Biophysical bases of elasticity imaging *Acoustical Imaging* vol 21, ed J P Jones (Berlin: Springer) pp 223–41.

Schaller G 1989 On the imaging of hot spots using correlation radiometers and a circular aperture *IEEE Trans. Microwave Theory Tech.* **37** 1210–1216.

Semenov S Y and Corfield D R 2008 Microwave tomography for brain imaging: Feasibility assessment for stroke detection *Int. J. Antennas Propag.* **2008** 254830-1-254830-8.

Semenov S Y, *et al.*, 1996 Microwave tomography: Two-dimensional system for biological imaging *IEEE Trans. Biomed. Eng.* **43** 869-877.

Semenov S Y 2000 Three-dimensional microwave tomography: Experimental imaging of phantoms and biological objects *IEEE Trans. Microw. Theory Tech.* **48** 1071-1074.

Semenov S Y, *et al.*, 2003 Microwave tomography for detection/imaging of myocardial infarction. I. Excised canine hearts *Ann. Biomed. Eng.* **31** 262-270.

Semenov S Y, *et al.*, 2006 Microwave tomographic imaging of the heart in intact swine *J. Electromag. Waves Appl.* **20** 873-890.

Shahzad A, *et al.*, 2017 Investigation of the effect of dehydration on tissue dielectric properties in in-vivo measurements *Biomedical Physics & Engineering Express.*, **3**.

Sill J E and Fear E C 2005 Tissue sensing adaptive radar for breast cancer detection-Experimental investigation of simple tumor models *IEEE Trans. Microw. Theory Tech.* **53** 3312-3319.

Smulders P 2013 Analysis of human skin tissue by millimeter-wave reflectometry *Skin Res. Technol.* **19** e209-e216.

Song H, *et al.* 2017 Detectability of breast tumor by a hand-held impulseradar detector: Performance evaluation and pilot clinical study *Sci. Rep.*, **7**.

Sorrentino R, Bianchi G (2010). Microwave and RF engineering. John Wiley & Sons.

Stuchly MA, Kraszewski A, Stuchly SS and Smith AM 1982 Dielectric properties of animal tissues in-vivo at radio and microwave frequencies comparison between species *Phys. Med. Biol.* **27** 927.

Stuchly S S, Goldberg M, Thansandote A, and Carraro B 1978 Monitoring of arterial wall movement by microwave Doppler radar *Symp. Electromagnetic Fields in Biological Systems* (Ottawa, Ont., Canada, June 27-30).

Sugitani T, *et al.*, 2014 Complex permittivities of breast tumor tissues obtained from cancer surgeries *Applied physics letters* **104** 253702.

Summers P E, *et al.* 2019 Towards mm-wave spectroscopy for dielectric characterization of breast surgical margins *ELSEVIER The Breast* **45** 64-69.

Susskind C 1973 Possible use of microwaves in the management of lung disease *Proc. IEEE* (Lett.) **61** 673.

Taeb A, Gigoyan S, Safavi-Naeini S 2013 Millimetre-wave waveguide reflectometers for early detection of skin cancer *IET Microwaves Antennas Propagat.* 7 1182-1186.

Tasto M and Schomberg H 1978 Object reconstruction from projections and some nonlinear extensions *NATO Advanced Study Institute on Pattern Recognition and Signal processing* (Paris, France, June 25-July 4).

Töpfer F and Oberhammer J 2015 Millimeter-wave tissue diagnosis: The most promising fields for medical applications *IEEE Microw. Mag.* **16** 97–113.

Vecchi F *et al.* 2011 A wideband receiver for multi-Gbit/s communications in 65 CMOS *IEEE Journal of Solid-State Circuits*, **46**, pp. 551–561.

Wang C H, Chiu Y T, and Lin Y S 2010 3.1 dB NF 20-29 GHz CMOS UWB LNA using a T-match input network *Electron. Lett.*, **46**, pp. 1312–1313.

Web site: www.airc.it

Web site: American Institute for Cancer Research: https://www.wcrf.org/dietandcancer/cancer-trends/breast-cancer-statistics

Williams B T, *et al.* 1971 Continuous long-term measurement of cardiac output after open-heart surgery *Ann. Surg.* **174** 357-363.

Yamaura I 1978 Measurement of heart dynamics using microwaves (Fourth Rep.)-microwave stethoscope," *Inst. Electron. Commun. Eng. Japan* **TG-EMCJ78-15** 9-14.

Yang D, Bertram JM, Converse MC, O'Rourke AP, Webster JG, Hagness SC, Will JA and Mahvi DM 2005 A floating sleeve antenna yields localized hepatic microwave ablation IEEE Trans. Biomed. Eng. **53** 533–7.

Yang F, *et al.* 2017 A large-scale clinical trial of radar-based microwave breast imaging for Asian women: Phase I in *Proc. Int. Symp. Antennas Propag.*, Jul. 9–14, pp. 781–783.